Early Solar System Processes and Parent Body Relationships Recorded by Chromium and Titanium Isotopes in Meteorites

by

Zachary A. Torrano

A Dissertation Presented in Partial Fulfillment
of the Requirements for the Degree
Doctor of Philosophy

Approved June 2020 by the
Graduate Supervisory Committee:

Meenakshi Wadhwa, Chair
Ariel Anbar
Devin Schrader
David Williams
Patrick Young

ARIZONA STATE UNIVERSITY

August 2020

ABSTRACT

Meteorites and their components can be used to unravel the history of the early Solar System. Carbonaceous chondrites are meteorites that originated from undifferentiated parent bodies that formed within a few million years of the beginning of the Solar System. These meteorites contain calcium-aluminum-rich inclusions (CAIs), which are the oldest dated solids in the Solar System at ~4.567 billion years old and thus preserve a record of the earliest stage of Solar System formation. The isotopic compositions of CAIs and bulk carbonaceous chondrites can be used to identify the sources of material inherited by the protoplanetary disk, assess the degree of mixing in the disk, and evaluate sample origins and potential genetic relationships between parent bodies. In particular, mass-independent Cr and Ti isotopic compositions have proven to be especially useful for these purposes.

In this work, I first developed new methods for the chemical separation of Cr and Ti, improving the reliability of existing methods to ensure consistent yields and accurate isotopic measurements. I then measured the Cr and Ti isotopic compositions of CAIs from CV and CK chondrites to determine the extent of isotopic heterogeneity in the CAI-forming region and assess the role of CAIs in the preservation of planetary-scale isotopic anomalies. My results show that all measured CAIs originated from a common isotopic reservoir that incorporated material from at least three distinct nucleosynthetic sources and preserved limited isotopic heterogeneity. These results also suggest that planetary-scale isotopic anomalies cannot be attributed solely to the transport of CAIs from one part of the solar nebula to another. I finally measured the Cr and Ti isotopic compositions of bulk CM, CO, and ungrouped chondrites to evaluate the relationship between CM and

CO chondrites, which have been suggested to originate from either distinct but related parent bodies or a common compositionally heterogeneous parent body. My results suggest that CM, CO, and related ungrouped chondrites originated from distinct parent bodies that formed from similar precursor materials in nearby formation regions. These results may have implications for asteroid samples returned by the OSIRIS-REx and Hayabusa2 missions.

DEDICATION

This dissertation is dedicated to my grandparents.

ACKNOWLEDGMENTS

This dissertation would not have been possible without the support of numerous individuals. I would first like to thank my supervisory committee members both past and present, including Mini Wadhwa, Ariel Anbar, Dave Williams, Devin Schrader, Patrick Young, Alyssa Rhoden, and Chris Groppi. I am particularly thankful for my advisor Mini Wadhwa, whose guidance and support has enabled my growth as a scientist during my time at ASU. I am grateful for the support of Steve Romaniello, Rebekah Hines, and Vinai Rai in the Isotope Cosmochemistry and Geochronology Laboratory, all of whom contributed to my development as a laboratory scientist. I am appreciative of the help of Laurence Garvie in the Center for Meteorite Studies, whose assistance with selecting and procuring meteorite samples was instrumental for this work. Much of this work would not have come to fruition without the generous help of many collaborators, including Greg Brennecka, Jemma Davidson, and Curtis Williams. I would also like to thank those who helped me along my scientific journey prior to ASU, including Tony Simonetti for giving me my first experience in scientific research, Clive Neal for encouraging me to become involved in planetary science, and Duck Mittlefehldt for introducing me to the world of meteorites and cosmochemistry.

I am fortunate to have had amazing colleagues in the Center for Meteorite Studies who have also become some of my closest friends, including Soumya Ray, Emilie Dunham, Alice Stephant, Prajkta Mane, Daniel Dunlap, and Cameron Mercer. I am also fortunate to have had supportive friends throughout the School of Earth and Space Exploration and beyond, including Hannah Shamloo, Matt Sanborn, Aleisha Johnson, Kara Brugman, Jake Adler, Hannah Kerner, Crystyl Fudge, Nari Miller, Scott

Dickenshied, Alex Pye, Joel Leonard, Jessica Noviello, Sierra Ferguson, Kyle Mohr, and many more.

Thank you to the staff in the Center for Meteorite Studies and the School of Earth and Space Exploration, especially Rebecca Davis, Becca Dial, Juana Garcia, and Cami Skiba. Their hard work kept things running smoothly, from my first visit to ASU as a prospective student, through numerous travel and grant reimbursements, and on to preparations for my defense. I would like to extend a special thank you to Thijs van Soest for his willingness to drive me to the hospital any time of the day or night and his generosity in sharing his delicious home cooked meals. Finally, I would like to thank my parents and canine siblings for their love and support.

TABLE OF CONTENTS

Page

LIST OF TABLES xii

LIST OF FIGURES. xiii

CHAPTER

1 INTRODUCTION 1

1.1 Background 1

1.2 Abstract for Chapter 2 6

1.3 Abstract for Chapter 3 7

1.4 Abstract for Chapter 4 8

2 TITANIUM ISOTOPE SIGNATURES OF CALCIUM-ALUMINUM-RICH INCLUSIONS FROM CV AND CK CHONDRITES: IMPLICATIONS FOR EARLY SOLAR SYSTEM RESERVOIRS AND MIXING 10

Abstract 10

2.1 Introduction 11

2.2 Samples and Methods 15

2.2.1 Sample Description 15

2.2.2 Sample Extraction 18

2.2.3 Analytical Methods 19

2.2.3.1 Clean Laboratory Reagents 19

2.2.3.2 Sample Digestion and Concentration Measurements. 19

2.2.3.2 Titanium Purification Chemistry 20

CHAPTER Page

2.2.3.2 Titanium Isotope Measurements 23

2.3 Results 25

2.3.1 Rare Earth Element Concentrations..... 25

2.3.2 Titanium Isotopic Compositions 28

2.4 Discussion 31

2.4.1 The Relationship Between REE Patterns, CAI Size, and Ti Isotopic Anomalies 31

2.4.2 Implications for the CAI-forming Region in the Solar Nebula..... 34

2.4.3 The Relationship Between ^{46}Ti and ^{50}Ti..... 35

2.4.4 Ti Isotopic Anomalies as Tracers of Mixing in the Solar Nebula. 38

2.5 Conclusions 43

3 CHROMIUM AND TITANIUM ISOTOPIC COMPOSITIONS OF CALCIUM-ALUMINUM-RICH INCLUSIONS: CLUES TO THE FORMATION OF DISTINCT ISOTOPIC RESERVOIRS IN THE EARLY SOLAR SYSTEM.. 46

3.1 Introduction 46

3.2 Samples and Methods 49

3.2.1 Sample Description 49

3.2.2 Sample Extraction 50

3.2.3 Analytical Methods 50

3.2.3.1 Sample Digestion and Concentration Measurements. 50

3.2.3.2 Cr Purification via Column Chromatography 51

CHAPTER Page

3.2.3.3 Additional Cr Purification 52

3.2.3.4 Cr Isotopic Analyses 55

3.2.3.5 Ti Purification and Isotopic Analyses 56

3.3 Results 58

3.3.1 Rare Earth Element Concentrations 58

3.2.2 Cr and Ti Isotopic Compositions 59

3.4 Discussion 61

3.4.1 Potential Isotopic Effects of Matrix Addition to CAIs 61

3.4.2 The Relationship Between REE Patterns and Anomalies 65

3.4.3 Clues to the Origin of the NC–CC Isotopic Dichotomy 66

3.4.4 Identifying the Sources Contributing to the Infalling Material 73

3.4.5 Isotopic Variability in CAIs: Inherited or Prodcued in the Disk?. 76

3.5 Conclusions 80

4 THE RELATIONSHIP BETWEEN CM AND CO CHONDRITES: INSIGHTS FROM CORRELATED CHROMIUM AND TITANIUM ISOTOPIC ANALYSES OF UNGROUPED CHONDRITES 82

4.1 Introduction 82

4.2 Samples and Methods 85

4.2.1 Sample Description 85

4.2.2 Analytical Methods 86

4.2.2.1 Sample Digestion and Concentration Measurements. 86

CHAPTER Page

4.2.2.2 Cr and Ti Purification and Isotopic Analyses 87

4.3 Results 89

4.3.1 Cr and Ti Isotopic Compositions 89

4.4 Discussion 90

4.4.1 Constraining the Range of Cr and Ti Isotopic Compositions of CM and CO Chondrites 90

4.4.2 Evaluating Potential Genetic Relationships in ε^{50}Ti vs. ε^{54}Cr Isotope Space 98

4.4.2.1 EET 83355 and EET 83226 99

4.4.2.2 MAC 87300, MAC 87301, and MAC 88107 100

4.4.2.3 Coolidge 102

4.4.2.4 GRO 95566 103

4.4.2.5 LEW 85332 104

4.4.2.6 MWA 5958 105

4.4.2.7 LAP 04757 and LAP 04773 106

4.4.3 Implications for the Relationship Between CM and CO Chondrites 108

4.4.4 Implications for the Formation Time and Location of Ungrouped Chondrite Parent Bodies 110

4.4.5 Implications for Asteroid Sample Return Missions 112

4.5 Conclusions 113

CHAPTER Page

5 SUMMARY AND FUTURE DIRECTIONS 117

5.1 Summary 117

5.2 Future Directions 120

5.2.1 Identifying the Carriers of Isotopic Anomalies in Meteorites 122

5.2.2 Determining the Relative Ages of Refractory Inclusions and Correlating These With Their Isotopic Anomalies 123

5.2.3 Utilizing Meteoritic Data in Combination with Astrophysical Modeling 124

REFERENCES 126

APPENDIX

A. A RECLASSIFICATION OF NORTHWEST AFRICA 2900 FROM CV3 TO CK3.8 CHONDRITE 144

Abstract 145

A.1 Introduction 146

A.2 Analytical Methods 149

A.2 Results 150

A.2.1 Petrography 150

A.2.2 Magnetite Morphologies and Composition 153

A.2.3 Olivine Compositions 156

A.3 Discussion 160

A.3.1 The Classification of Northwest Africa 2900 160

APPENDIX Page

A.3.2 New Criteria for Distinguishing Between CV and CK Chondrites 162

A.4 Summary..... 164

A.5 References for Appendix A..... 166

B. PREVIOUS PUBLICATIONS AND STATEMENT OF CO-AUTHORS.... 170

LIST OF TABLES

Table		Page
2.1	List of CAIs Studied in Chapter 2	16
2.2	Titanium Purification Chemistry Methods	22
2.3	REE Concentrations in CAIs Studied in Chapter 2	27
2.4	Ti Isotopic Compositions of CAIs Studied in Chapter 2	29
3.1	List of CAIs Studied in Chapter 3	50
3.2	Chromium Purification Chemistry Methods	55
3.3	REE Concentrations in CAIs Studied in Chapter 3	59
3.4	Cr and Ti Isotopic Compositions of CAIs Studied in Chapter 3	61
4.1	List of Samples Studied in Chapter 4	86
4.2	Cr and Ti Isotopic Compositions of Samples Studied in Chapter 4	90
A1	NWA 2900 Chondrule Magnetite Compositions	155
A2	NWA 2900 Chondrule and Matrix Olivine Compositions	158

LIST OF FIGURES

Figure		Page
2.1	Back-Scattered Electron (BSE) Images of CAIs Studied in Chapter 2	17
2.2	Ti Isotope Measurement External Reproducibilities	25
2.3	REE Abundances in the CAIs Studied in Chapter 2	27
2.4	ε^{50}Ti Compositions of CAIs Studied in Chapter 2	30
2.5	ε^{50}Ti Compositions of CAIs Studied in Chapter 2 and in the Literature	31
2.6	ε^{50}Ti vs. Chondrite-normalized La/Lu Ratios in CAIs	33
2.7	ε^{50}Ti vs. CAI Mass	34
2.8	ε^{50}Ti vs. ε^{46}Ti for CAIs and Bulk Meteorites	36
2.9	Schematic Diagram of Homogenization of Ti Isotopic Anomalies	42
3.1	Effects of Fe on Cr Isotopic Measurements	54
3.2	REE Abundances in the CAIs Studied in Chapter 3	59
3.3	Mixing Lines Between CAIs and Matrix in ε^{50}Ti vs. ε^{54}Cr Space	63
3.4	ε^{54}Cr vs. ppm Cr in the CAIs Studied in Chapter 3	64
3.5	ε^{50}Ti and ε^{54}Cr vs. La/Lu Ratios	65
3.6	ε^{50}Ti vs. ε^{54}Cr for Bulk NC Materials, CC Materials, and CAIs	67
3.7	ε^{50}Ti and ε^{54}Cr vs. Si- and CI-normalized Al Abundances	69
3.8	ε^{54}Cr vs. Ge and Cu Concentrations	70
3.9	ε^{46}Ti vs. ε^{50}Ti for the CAIs Studied in Chapter 3	75
3.10	ε^{53}Cr vs. ε^{54}Cr for bulk NC materials, CC materials, and CAIs	76
3.11	ε^{50}Ti and ε^{54}Cr values for CAIs Studied in Chapter 3 and the Literature	77

Figure Page

4.1 $\delta^{17}O$ vs. $\delta^{18}O$ for CO, CM, CM-an, and C2-ungrouped Chondrites 84

4.2 $\varepsilon^{50}Ti$ vs. $\varepsilon^{54}Cr$ for Bulk Carbonaceous Chondrites 94

4.3 Mixing Line Between CV and CAI Composition in $\varepsilon^{54}Cr$ vs. $\varepsilon^{50}Ti$ Space 96

4.4 $\varepsilon^{50}Ti$ vs. wt.% Ca and Al 98

4.5 $\varepsilon^{54}Cr$ vs. $\varepsilon^{50}Ti$ for LAP 04757, LAP 04773, and Ordinary Chondrites 108

A1 BSE and RGB Images of NWA 2900 151

A2 BSE Images of NWA 2900 Chondrules 152

A3 BSE Images of NWA 2900 Matrix Regions 153

A4 BSE Images of NWA 2900 Chondrule Magnetite 154

A5 NWA 2900 Magnetite Compositions Plotted with Literature Data 156

A6 Histogram of Fa Content in NWA 2900 Chondrule and Matrix Olivine 158

A7 NWA 2900 Chondrule Olivine Compositions Plotted with Literature Data 159

A8 Bulk Oxygen Isotope Compositions of CV and CK Chondrites 164

CHAPTER 1

INTRODUCTION

1.1 Background

Over the past ~4.5 billion years, the region around our Sun has evolved from a protoplanetary disk of gas and dust to the Solar System we know today. As a result of this evolution, forensic investigations must be conducted to learn about the earliest stages of our Solar System's formation. Meteorites are the ideal tools for such investigations because they preserve a record of our Solar System's early history and thereby enable us to probe its origins and evolution through time. By studying meteorites and their individual components, we can identify the material inherited by our protoplanetary disk from the molecular cloud, assess the degree of mixing in the protoplanetary disk, evaluate sample origins and potential genetic relationships between meteorite parent bodies, and learn about the process of planet formation. Meteorites come from diverse parent bodies, and their widely varying textures and compositions reflect their varied origins. Broadly, meteorites originate from two types of parent bodies: bodies that have not melted ("undifferentiated") and bodies that have undergone partial or complete melting ("differentiated"). This dissertation focuses on meteorites known as chondrites that originate from undifferentiated bodies and contain components that preserve a record of the earliest history of our Solar System.

The isotopic compositions of meteorites and their components can be used to interpret the historical record of our Solar System. This dissertation focuses on the isotopes of the elements Cr and Ti, which have proven to be particularly useful for these

purposes. The neutron-rich isotopes ^{50}Ti and ^{54}Cr are produced in supernovae and thus may be used to trace supernova material inherited by our protoplanetary disk (e.g., Clayton, 2003; Wanajo et al., 2013; Davis et al., 2018). A significant recent finding was the discovery of a planetary-scale isotopic dichotomy between "non-carbonaceous chondritic" (NC) and "carbonaceous chondritic" (CC) Solar System materials that is observed for a wide range of isotope systems, including Cr and Ti (e.g., Warren, 2011). These two distinct isotopic reservoirs are suggested to be represented by rocky parent bodies of inner (NC) and outer (CC) Solar System provenance, perhaps kept separated by the formation and growth of Jupiter (Kruijer et al., 2017). Isotopic analyses can therefore be used to establish origin in distinct nebular reservoirs for meteorite parent bodies and to evaluate potential genetic relationships between meteorites (e.g., Warren, 2011; Sanborn et al., 2019). An open question is whether this planetary-scale isotopic dichotomy was created because of processes (such as thermal processing, transport, and mixing) occurring within the protoplanetary disk or whether it reflects inherited isotopic heterogeneity from the parent molecular cloud.

Calcium-aluminum-rich inclusions (CAIs) are refractory inclusions found in chondritic meteorites that are the oldest dated Solar System materials at ~4.567 billion years old (e.g., Connelly et al., 2012, 2017). In addition to these ancient absolute ages from Pb-Pb chronometry, short-lived chronometers such as ^{26}Al-^{26}Mg have shown that most CAIs exhibit an inferred initial ^{26}Al/^{27}Al ratio of ~5×10^{-5} arguing that these objects formed during a short time interval of less than 200,000 years (Jacobsen et al., 2008; MacPherson et al., 2012; Kawasaki et al. 2019; Liu et al., 2019). Because these inclusions formed at such an early time and over a short time period, they record a snapshot of the

very beginning of our Solar System. Previous studies have shown that CAIs record mass-independent isotopic anomalies in most elements, reflecting formation in an isotopically distinct reservoir from that of later formed solids such as bulk chondrites and terrestrial planets (e.g., Dauphas and Schauble, 2016). Whereas certain elements show resolvable ε-level (parts per ten thousand deviation from a standard) variability, others do not. While previous analyses of the Cr and Ti isotopic compositions of CAIs have been conducted, the majority of the Ti data and entirety of the Cr data are for CAIs from CV chondrites (and the vast majority of those are from a single CV chondrite, Allende, which is known to have undergone aqueous alteration and thermal metamorphism on its parent body; Krot et al., 1998). Additionally, only a small handful of CAIs from two CV chondrites have been measured for both their Cr and Ti isotopic compositions. The measurement of both Cr and Ti isotopic compositions of a single sample set of CAIs from several CV and CK chondrites is therefore an important step for making a more comprehensive assessment of the isotopic heterogeneity of the CAI-forming region, identifying the nucleosynthetic processes that produced the ingredients of our protoplanetary disk, determining the degree of mixing that occurred in the early Solar System, and evaluating the role of CAIs in planetary scale Cr and Ti isotopic anomalies.

The genetic relationships between bulk carbonaceous chondrites belonging to different groups can also provide important information about our early Solar System. Various chondrite groups are thought to represent meteorites originating from distinct parent bodies (e.g., Weisberg et al., 2006). The Mighei-like CM chondrites, Ornans-like CO chondrites, and ungrouped chondrites that may be related to these groups are of particular interest because previous studies have suggested that CM and CO chondrites

may have originated from parent bodies that formed in close proximity to each other and from similar precursor materials (e.g., Kallemeyn and Wasson, 1981; Clayton and Mayeda, 1999; Frank et al., 2014; Schrader and Davidson, 2017) or potentially from a common compositionally heterogeneous parent body (Greenwood et al., 2014). Quantitative modeling has suggested that the CM and CO chondrite parent bodies formed in nearby regions but at different times (Sugiura and Fujiya, 2014; Desch et al., 2018). A gap exists between the compositions of CM and CO chondrites in three-oxygen isotope space that is populated by ungrouped chondrites and anomalous CM chondrites that show affinities to both chondrite groups. A compositional gap also exists between CM and CO chondrites in ε^{54}Cr vs. ε^{50}Ti space (e.g., Warren, 2011; Sanborn et al., 2019), but the ε^{54}Cr and ε^{50}Ti isotopic compositions of the ungrouped and anomalous chondrites that plot in the compositional gap between CM and CO chondrites in three-oxygen isotope space have not yet been determined. Additionally, only two CM and two CO chondrites had been measured for their bulk Cr and Ti isotopic compositions prior to this dissertation work. Most previously reported Cr and Ti values are from different sample aliquots, but this dissertation work included measurements of both isotope systems from single aliquots of each sample.

The measurements of the Cr and Ti isotopic compositions of additional CM and CO chondrites conducted in this work aim to provide additional constraints on the compositional fields of these chondrite groups. Measurements of the Cr and Ti isotopic compositions of the ungrouped and anomalous chondrites that plot in the compositional gap between CM and CO chondrites in three-oxygen isotope space, along with ungrouped chondrites with similar mineralogic and/or geochemical characteristics, were

conducted to further evaluate the relationship between CM and CO chondrites and ascertain potential genetic relationships between these ungrouped chondrites. A better understanding of the potential genetic relationship between CM and CO chondrites and related ungrouped chondrites has implications for the ongoing OSIRIS-REx and Hayabusa2 sample return missions to the carbonaceous asteroids Bennu and Ryugu, respectively. These asteroids, from which material will be returned and studied in Earth-based laboratories, have been suggested to be analogous to CM chondrites based on currently available remote sensing data from the spacecraft (e.g., Hamilton et al., 2019; Kitazato et al., 2019; Lauretta et al., 2019) and may therefore be similar to the parent bodies of some of the samples studied here.

The motivating questions of this dissertation can each be addressed by the combination of Cr and Ti isotopic analyses of meteorites and their components. I used the Cr and Ti isotopic compositions of CAIs to assess the isotopic heterogeneity of the CAI-forming region near the young Sun, identify the initial ingredients inherited by our Solar System from the parent molecular cloud, and evaluate models for the ensuing isotopic evolution of our Solar System. I then used the Cr and Ti isotopic compositions of bulk CM, CO, and ungrouped chondrites to evaluate the relationship between CM and CO chondrites and potential implications for materials returned from carbonaceous asteroids by ongoing sample return missions. During the course of this work, I have developed new methods for the chemical separation of Cr and Ti that improved the efficiency and reliability of existing methods to ensure consistent yields as well as precise and accurate isotopic measurements. The abstracts of each chapter of this dissertation are presented below.

1.2 Titanium Isotope Signatures of Calcium-Aluminum-rich Inclusions from CV and CK Chondrites: Implications for Early Solar System Reservoirs and Mixing

The overwhelming majority of Ti isotopic data for CAIs is limited to inclusions from the CV chondrite Allende and a few other CV, CO, CM, and ordinary chondrites. It is therefore important to ascertain whether previously reported values for CAIs are representative of the broader CAI-forming region and to make a more rigorous assessment of the extent and implications of isotopic heterogeneity in the early Solar System. In this chapter, we report the mass-independent Ti isotopic compositions of a suite of 23 CAIs of diverse petrologic and geochemical types, including 11 from Allende and 12 from 7 other CV3 and CK3 chondrites. The data for CAIs from CK chondrites are the first reported measurements of Ti isotopic compositions of CAIs from this meteorite class. The resolved variation in the mass-independent Ti isotopic compositions of these CAIs indicates that the CAI-forming region of the early Solar System preserved isotopic variability. Nevertheless, the range of Ti isotopic compositions reported here for CAIs from CV and CK chondrites falls within the range observed in previously analyzed CAIs from CV, CO, CM, and ordinary chondrites. This implies that CAIs from CV, CK, CO, CM, and ordinary chondrites originated from a common nebular source reservoir characterized by mass-independent isotopic variability in Ti (and certain other elements). We further interpret these data to indicate that the Ti isotopic anomalies in CAIs represent the isotopic signatures of supernova components in presolar grains that were incorporated into the Solar System in an initially poorly mixed reservoir that was progressively homogenized over time. We conclude that the differing degrees of isotopic variability observed for different elements in normal CAIs are the result of distinct carrier

phases and that these CAIs were likely formed towards the final stages of homogenization of the large-scale isotopic heterogeneity that initially existed in the solar nebula.

1.3 Chromium and Titanium Isotopic Compositions of Calcium-Aluminum-rich Inclusions: Clues to the Formation of Distinct Isotopic Reservoirs in the Early Solar System

Although CAIs from CV, CK, CM, CO, and ordinary chondrites have been analyzed previously for their Ti isotopic compositions, only CAIs from two CV chondrites have been analyzed for their Cr isotopic compositions, and only a handful of CAIs have been measured for both their Cr and Ti isotopic compositions. In this chapter, we report the coupled mass-independent Cr and Ti isotopic compositions of several CAIs from both CV and CK chondrites; this is the first report of the Cr isotopic composition of a CAI from a CK chondrite. With these additional data, we aim to better constrain the compositional range of CAIs in ε^{50}Ti vs. ε^{54}Cr space, thereby facilitating the isotopic characterization of the material inherited by the solar protoplanetary disk and the role of CAIs in the formation of distinct planetary-scale isotopic reservoirs in our early Solar System. The resolved variation in both ε^{50}Ti and ε^{54}Cr in these CAIs indicates that the CAI-forming region preserved isotopic variability that likely resulted from a combination of isotopic heterogeneity inherited during infall from the parent molecular cloud, heterogeneous carrier phase distribution, and thermal processing in the disk. The ε^{50}Ti and ε^{54}Cr isotopic compositions of these CAIs further demonstrate that CAIs alone cannot be responsible for the offset between the non-carbonaceous chondritic (NC) and

carbonaceous chondritic (CC) isotopic reservoirs and instead are consistent with previous models in which infalling material from the molecular cloud was initially enriched in supernova-derived neutron rich isotopes (i.e., similar to the isotopic composition recorded by CAIs) and later changed to material depleted in these isotopes. Such models can explain the distinct compositions of planetary-scale isotopic reservoirs in the early Solar System.

1.4 The Relationship Between CM and CO Chondrites: Insights from Correlated Chromium and Titanium Isotopic Analyses of Ungrouped Chondrites

The isotopic compositions of meteorites can be used to determine the source region of their parent bodies and evaluate potential genetic relationships with known meteorite groups. A close relationship between CM and CO chondrites has been suggested, and previous studies of O-isotope compositions have even suggested a common parent body origin. In this study, we evaluate the genetic relationship between CM and CO chondrites using Cr and Ti isotopes. We first provide additional constraints on the ranges of Cr and Ti isotopic compositions of CM and CO chondrites by reporting the isotopic compositions of the CO chondrite Isna, and the CM chondrites Murchison, Murray, and Aguas Zarcas. We then report the Cr and Ti isotopic compositions of several ungrouped chondrites that have been previously reported to exhibit similarities to the CM and CO chondrite groups. These ungrouped chondrites include Elephant Moraine (EET) 83226, EET 83355, Grosvenor Mountains (GRO) 95566, MacAlpine Hills (MAC) 87300, MAC 87301, MAC 88107, and Northwest Africa (NWA) 5958. We additionally report the Cr and Ti isotopic compositions of other ungrouped chondrites LaPaz Ice Field (LAP)

04757, LAP 04773, Lewis Cliff (LEW) 85332, and Coolidge to assess their potential relationships with known carbonaceous and ordinary chondrite groups. Our results extend and redefine the CM and CO chondrite group compositional fields in $\varepsilon^{54}Cr$ vs. $\varepsilon^{50}Ti$ space and suggest that many of the ungrouped chondrites studied here possess affinities to multiple carbonaceous chondrite groups. Two ungrouped chondrites studied here (LAP 04757 and LAP 04773) exhibit isotopic compositions consistent with classification as low-FeO ordinary chondrites. We conclude that the ungrouped chondrites that show affinities to multiple carbonaceous chondrite groups likely originated from distinct parent bodies that may have formed from similar precursor material and/or in nearby formation regions in the solar protoplanetary disk.

CHAPTER 2

TITANIUM ISOTOPE SIGNATURES OF CALCIUM-ALUMINUM-RICH INCLUSIONS FROM CV AND CK CHONDRITES: IMPLICATIONS FOR EARLY SOLAR SYSTEM RESERVOIRS AND MIXING

Abstract

Calcium-aluminum-rich inclusions (CAIs) are the first solids to form in the early Solar System, and they exhibit nucleosynthetic anomalies in many isotope systems. The overwhelming majority of isotopic data for CAIs is limited to inclusions from the CV chondrite Allende and a few other CV, CO, CM, and ordinary chondrites. It is therefore important to ascertain whether previously reported values for CAIs are representative of the broader CAI-forming region and to make a more rigorous assessment of the extent and implications of isotopic heterogeneity in the early Solar System. Here, we report the mass-independent Ti isotopic compositions of a suite of 23 CAIs of diverse petrologic and geochemical types, including 11 from Allende and 12 from 7 other CV3 and CK3 chondrites; the data for CAIs from CK chondrites are the first reported measurements of Ti isotopic compositions of CAIs from this meteorite class. The resolved variation in the mass-independent Ti isotopic compositions of these CAIs indicates that the CAI-forming region of the early Solar System preserved isotopic variability. Nevertheless, the range of Ti isotopic compositions reported here for CAIs from CV and CK chondrites falls within the range observed in previously analyzed CAIs from CV, CO, CM, and ordinary chondrites. This implies that CAIs from CV, CK, CO, CM, and ordinary chondrites originated from a common nebular source reservoir characterized by mass-independent

isotopic variability in Ti (and certain other elements). We further interpret these data to indicate that the Ti isotopic anomalies in CAIs represent the isotopic signatures of supernova components in presolar grains that were incorporated into the Solar System in an initially poorly mixed reservoir that was progressively homogenized over time. We conclude that the differing degrees of isotopic variability observed for different elements in normal CAIs are the result of distinct carrier phases and that these CAIs were likely formed towards the final stages of homogenization of the large-scale isotopic heterogeneity that initially existed in the solar nebula.

2.1 Introduction

Calcium-aluminum-rich inclusions (CAIs) are the oldest dated Solar System materials and are thought to be the first solids formed in the early Solar System at ~4.567 Ga (Amelin et al., 2002; Amelin et al., 2009; Bouvier et al., 2011; Connelly et al., 2012, 2017). Most CAIs have an inferred initial $^{26}Al/^{27}Al$ ratio of ~5×10^{-5} that is used to define the short time interval for CAI formation, which may have been less than 100,000 years and perhaps as low as ~20,000 years (e.g., Bizzarro et al., 2004; Jacobsen et al., 2008; MacPherson et al., 2012). As such, CAIs provide an important record of the earliest processes and conditions in our Solar System (Wood, 2004; MacPherson, 2013).

Previous investigations have shown that CAIs possess mass-independent (presumably nucleosynthetic) isotopic anomalies in most elements, reflecting their formation in an isotopically distinct reservoir when compared to subsequently formed solids such as bulk chondrites and terrestrial planets (e.g., Dauphas and Schauble, 2016 and references therein). Characterizing the isotopic anomalies in CAIs is crucial for our

understanding of the early Solar System because this can provide constraints on nucleosynthetic processes that produced the ingredients in the solar nebula. As such, constraining the composition of the region in which CAIs formed in the early Solar System can inform Solar System formation models and help to track its isotopic and chemical evolution. Furthermore, these data can be used to evaluate the extent of isotopic heterogeneity in the early solar nebula, which could provide useful information about mixing processes and dynamics of the early Solar System. The focus of this study is on the mass-independent isotopic anomalies in the abundant "normal" CAIs found in primitive chondritic meteorites (which will simply be referred to as CAIs from hereon) and not on other rarer refractory materials also found in such meteorites – such as hibonite-rich inclusions designated as PLACs (platy hibonite crystals) or PLAC-like CAIs (Zinner et al., 1986; Fahey et al., 1987; Hinton et al., 1987; Ireland, 1990; Sahijpal et al., 2000; Liu et al., 2009; Kööp et al., 2016a,b), SHIBs (spinel-hibonite inclusions; Fahey et al., 1987; Ireland, 1988, 1990; Sahijpal et al., 2000; Liu et al., 2009; Kööp et al., 2016a), and FUN CAIs (Fractionated and Unidentified Nuclear effect CAIs; e.g., Niederer et al., 1985; Papanastassiou and Brigham, 1989; Loss et al., 1994; Williams et al., 2016, 2017; Kööp et al., 2018). These rarer objects all have large and variable nucleosynthetic anomalies in multiple elements, as well as non-canonical $^{26}Al/^{27}Al$, suggesting that either they did not form in the same spatial nebular reservoir as the more abundant CAIs or they were formed at a time prior to large-scale homogenization of the nebula (e.g., Kööp et al., 2016b; Render et al., 2019).

In CAIs, certain elements such as Ca (Jungck et al., 1984; Huang et al., 2012), Ti (Heydegger et al., 1979; Niederer et al., 1980, 1981, 1985; Niemeyer and Lugmair, 1981,

1984; Loss et al., 1994; Chen et al., 2009; Leya et al., 2009; Trinquier et al., 2009; Williams et al., 2016; Davis et al., 2018; Ebert et al., 2018; Render et al., 2019), Cr (Birck and Allègre, 1984; Birck and Allègre, 1985; Papanastassiou, 1986; Birck and Lugmair, 1988; Loss et al., 1994), Ni (Render et al., 2018), Sr (Myojo et al., 2018), Zr (Akram et al., 2013), Mo (Burkhardt et al., 2011; Shollenberger et al., 2018a), Hf (Peters et al., 2017), and W (Kruijer et al., 2014), show resolvable ε-level (parts per ten thousand deviation from a standard) variation. However, other elements, such as Ba, Nd, Sm (Brennecka et al., 2013; Shollenberger et al., 2018a), Er, and Yb (Shollenberger 2018b), do not exhibit resolvable variation in the measured CAIs. The Ba, Nd, Sm, Er, and Yb isotopic data are largely based on measurements of different element cuts that were separated from the same CAIs, which could possibly have resulted in a biased view on the presumed isotopic homogeneity of these elements in the CAI-forming region. We also note that these previous isotopic studies of CAIs have focused predominantly on inclusions from the Allende CV chondrite, which is known to have been altered by secondary processes on its parent body (e.g., Krot et al., 1998 and references therein). Moreover, only a few CAIs from other CV, CO, CM, and ordinary chondrites have been analyzed thus far. This leads to the question of whether these previously analyzed CAIs are representative of CAIs from other chondrites and chondrite groups, and by extension, the broader CAI-forming region in the solar nebula.

Therefore, to improve our understanding of the isotopic composition of the CAI-forming region as a whole, it is important to conduct analyses of CAIs from a variety of chondrite types, and particularly from primitive meteorites that have not undergone extensive secondary alteration. The Fe-peak elements (with $22 \leq Z \leq 30$) are of particular

interest because they can be used to probe the late evolution of massive stars and the interstellar medium and thereby ascertain the potential contribution from stellar sources to our Solar System. Additionally, Fe-peak elements constitute a significant fraction of the total mass of meteoritic and terrestrial planet-building material as they are the constituents of major rock-forming minerals. In this study of CAIs from several CV and CK chondrites, we focus on the isotopic composition of the Fe-peak element Ti (Z = 22), which is enriched in CAIs compared to CI chondrites by a factor of 2 to 20, depending on the sample. Titanium has five stable isotopes (^{46}Ti, ^{47}Ti, ^{48}Ti, ^{49}Ti, and ^{50}Ti) and the ratios of these isotopes to one another in CAIs preserve information about their nucleosynthetic sources as well as the degree of isotopic heterogeneity in the early solar nebula.

The first studies of Ti isotopes in CAIs were conducted nearly four decades ago (e.g., Heydegger et al., 1979; Niederer et al., 1980, 1981, 1985; Niemeyer and Lugmair, 1981, 1984), and these studies noted the presence of Ti isotopic anomalies in CAIs. To better resolve these anomalies, recent studies during the last decade have taken advantage of analytical advances to conduct higher precision Ti isotopic measurements of CAIs (e.g., Leya et al., 2009; Trinquier et al., 2009; Davis et al., 2018; Ebert et al., 2018; Render et al., 2019). However, of the ~106 Ti isotopic analyses of CAIs from CV chondrites reported in the literature, ~96 are from Allende, and the rest are from 4 other CV chondrites Leoville, Vigarano, Efremovka, and Northwest Africa (NWA) 2364. Six CAIs from 3 ordinary chondrites, 12 CAIs from 7 CO chondrites, and 8 CAIs from CM2 chondrite Jbilet Winselwan have also been measured for their Ti isotopic compositions.

Because CAIs from only a few meteorites have been reported previously for their Ti isotopic compositions, there exists the possibility of a biased dataset. Therefore, to

improve our understanding of the isotopic composition of the CAI-forming region, it is important to conduct a more comprehensive study of the Ti isotopic compositions of CAIs from multiple chondrite classes. To this end, we report here the mass-independent Ti isotopic compositions of 23 CAIs (belonging to different petrologic and geochemical types) not only from the Allende CV chondrite but also from 7 different CV and CK chondrites. This study reports the first measurements of the Ti isotopic compositions of CAIs from CK chondrites.

2.2 Samples and Methods

2.2.1 Sample Description

The sample set studied here includes 11 CAIs from the Allende $CV3_{ox}$ chondrite and 12 CAIs from 7 other CV3 (including oxidized, reduced, and anomalous subgroups) and CK3 chondrites; a summary of the characteristics of these samples is shown in Table 2.1. They include both coarse-grained (type A and B) and fine-grained CAIs. The 11 coarse- and fine-grained CAIs studied here from the Allende $CV3_{ox}$ chondrite (hereafter "Allende CAIs") were previously characterized by Brennecka et al. (2010). Multiple elements were separated from these Allende CAIs and their isotopic compositions have been reported previously, including for U (Brennecka et al., 2010), Sr, Mo, Ba, Nd, and Sm (Brennecka et al., 2013), Te (Brennecka et al., 2017), Ni (Render et al., 2018), Er, Yb, and Hf (Shollenberger et al., 2018b). Four coarse-grained CAIs studied here, i.e., Homer (from CK3 NWA 4964), Bart (from CK3 NWA 6254), Marge (from $CV3_{ox}$ NWA 6619), and Lisa (from $CV3_{ox}$ NWA 6991) (hereafter referred to as "Simpson CAIs"), were characterized previously and isotopic compositions of Ba, Er, Mo, Nd, Sm, Sr, and

Yb have been reported for these CAIs (Shollenberger et al., 2018a,b). Eight additional coarse- and fine-grained CAIs, i.e., ZT1 and ZT2 from $CV3_{red}$ Leoville, ZT3 from $CV3_{ox}$ NWA 6991, ZT4 and ZT5 from $CV3_{an}$ NWA 7891, and ZT7, ZT8, and ZT9 from $CV3_{ox}$ NWA 3118, were obtained for this work and have not been characterized previously (hereafter "ZT CAIs"). Since the Allende and Simpson CAIs studied here have already been characterized and described previously (Brennecka et al., 2010; Shollenberger et al., 2018a), in the following we provide a description and characterization of only the 8 ZT CAIs.

Table 2.1. List of the CAIs included in this study.

CAI	Meteorite	Mass (g)	wt.% Ti	CAI Type	REE Pattern	Other Elements Analyzed
CAI 164	Allende ($CV3_{ox}$)	0.705	0.31	Coarse, B	Group I	Ni[1], Sr[2], Mo[2], Te[3], Ba[2], Nd[2], Sm[2], Er[4], Yb[4], Hf[4], U[5]
CAI 165	Allende ($CV3_{ox}$)	2.838	0.09	Coarse, B/A1	Group III	Ni[1], Sr[2], Mo[2], Te[3], Ba[2], Nd[2], Sm[2], Er[4], Yb[4], Hf[4], U[5]
CAI 166	Allende ($CV3_{ox}$)	0.173	0.33	Fine-grained	Group II	Ni[1], Sr[2], Te[3], Ba[2], Nd[2], Sm[2], U[5]
CAI 167	Allende ($CV3_{ox}$)	0.368	0.13	Fine-grained	Group II	Ni[1], Sr[2], Te[3], Nd[2], Sm[2], U[5]
CAI 168	Allende ($CV3_{ox}$)	1.343	0.17	Coarse, A	Group I	Ni[1], Sr[2], Te[3], Ba[2], Nd[2], Sm[2], Er[4], Yb[4], Hf[4], U[5]
CAI 170	Allende ($CV3_{ox}$)	0.199	0.43	Coarse, B1	Group I	Sr[2], Te[3], Ba[2], Nd[2], Sm[2], Er[4], Yb[4], U[5]
CAI 171	Allende ($CV3_{ox}$)	0.199	0.27	Coarse, B	Group III	Ni[1], Mo[2], Te[3], Ba[2], Nd[2], Sm[2], Er[4], Yb[4], U[5]
CAI 172	Allende ($CV3_{ox}$)	0.441	0.35	Coarse, B	Group I	Ni[1], Sr[2], Mo[2], Te[3], Ba[2], Nd[2], Sm[2], Er[4], Yb[4], Hf[4], U[5]
CAI 173	Allende ($CV3_{ox}$)	0.607	0.31	Fine-grained	Group III	Ni[1], Sr[2], Mo[2], Te[3], Ba[2], Nd[2], Sm[2], Er[4], Yb[4], Hf[4], U[5]
CAI 174	Allende ($CV3_{ox}$)	0.441	0.45	Coarse, B	Group I	Ni[1], Sr[2], Mo[2], Te[3], Ba[2], Nd[2], Sm[2], Er[4], Yb[4], Hf[4], U[5]
CAI 175	Allende ($CV3_{ox}$)	0.310	0.08	Fine-grained	Group II	Ni[1], Sr[2], Te[3], Ba[2], Nd[2], Sm[2], U[5]
Homer	NWA 4964 (CK3)	0.136	0.27	Coarse, C	Group II	Ni[1], Sr[6], Mo[6], Ba[6], Nd[6], Sm[6], Yb[4]
Marge	NWA 6619 ($CV3_{ox}$)	0.112	0.42	Coarse, B	Group III	Ni[1], Sr[6], Mo[6], Ba[6], Nd[6], Sm[6], Er[4], Yb[4]
Bart	NWA 6254 (CK3)	0.069	0.75	Coarse, C	Group III	Ni[1], Sr[6], Mo[6], Ba[6], Nd[6], Sm[6], Er[4], Yb[4]
Lisa	NWA 6991 ($CV3_{ox}$)	0.053	0.61	Coarse, B1	Group I	Ni[1], Sr[6], Mo[6], Ba[6], Nd[6], Sm[6], Er[4], Yb[4]
ZT1	Leoville ($CV3_{red}$)	0.018	1.06	Coarse, B1	Group I	-
ZT2	Leoville ($CV3_{red}$)	0.042	0.71	Coarse, B1	Group II	-
ZT3	NWA 6991 ($CV3_{ox}$)	0.0088	0.35	Fine-grained	Group II	-
ZT4	NWA 7891 ($CV3_{an}$)	0.0035	1.04	Coarse, CTA	Group I	-
ZT5	NWA 7891 ($CV3_{an}$)	0.0017	0.10	Coarse	Group II	-
ZT7	NWA 3118 ($CV3_{ox}$)	0.0057	0.78	Coarse, CTA	Group I	-
ZT8	NWA 3118 ($CV3_{ox}$)	0.0084	0.95	Coarse, CTA	Group III	-
ZT9	NWA 3118 ($CV3_{ox}$)	0.0031	0.30	Fine-grained	Group II	-

[1]Render et al., 2018, [2]Brennecka et al., 2013, [3]Brennecka et al., 2017, [4]Shollenberger et al., 2018b, [5]Brennecka et al., 2010, [6]Shollenberger et al., 2018a. $CV3_{ox}$ = CV3 oxidized subgroup; $CV3_{red}$ = CV3 reduced subgroup; $CV3_{an}$ = CV3 anomalous subgroup; CTA = compact type A.

A fragment of each of the ZT CAIs and the surrounding matrix was embedded in epoxy and polished to produce 1-in. round thick sections. Samples were then characterized using the JEOL JXA-8520F electron microprobe in the Eyring Materials Center at Arizona State University (ASU). The physical characteristics and classification

of the ZT CAIs are provided in Table 2.1 and back-scattered electron (BSE) images showing the mineralogy of these CAIs are shown in Fig. 2.1. Chemical mapping of each of the sections of these CAIs revealed minimal, if any, secondary alteration products.

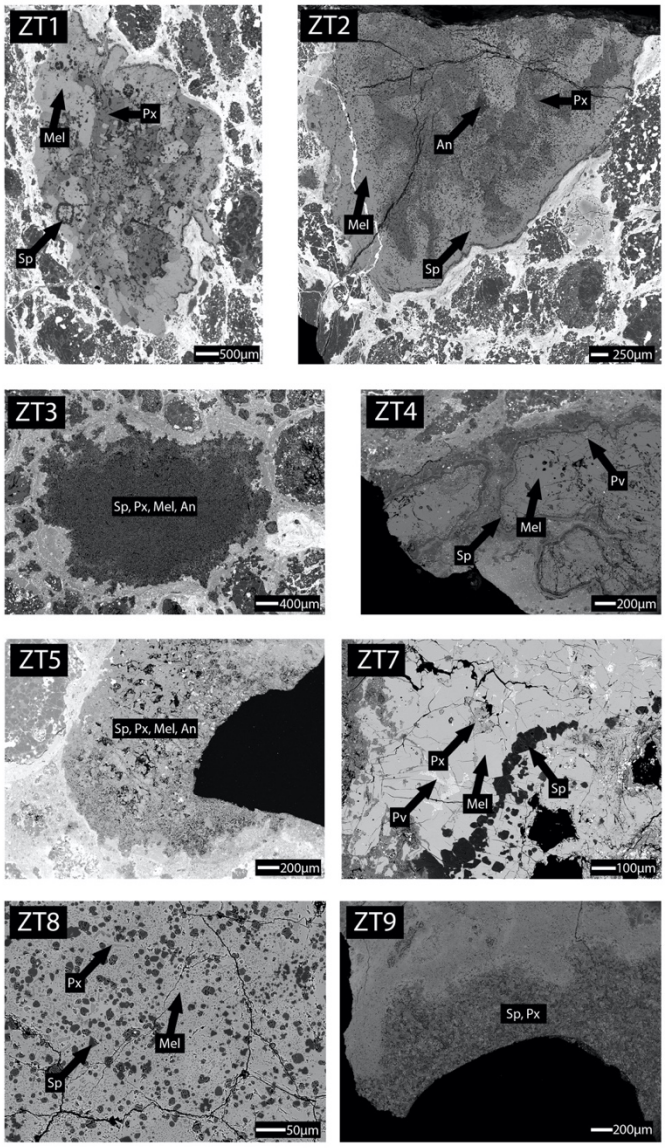

Fig. 2.1 Back-scattered electron (BSE) images of the 8 ZT CAIs studied here. ZT1 is a coarse-grained type B1 CAI from the $CV3_{red}$ chondrite Leoville; it possesses a mantle of melilite (Mel) surrounding a core enriched in pyroxene (Px) and spinel (Sp). ZT2 is a coarse-grained type B1 CAI from the $CV3_{red}$ chondrite Leoville; it possesses a mantle of melilite (Mel) surrounding a core enriched in pyroxene, spinel, and anorthite (An). ZT3 is a fine-grained spinel-pyroxene CAI from the $CV3_{ox}$ chondrite NWA 6991; in addition to abundant spinel and pyroxene, ZT3 also contains some melilite and anorthite. ZT4 is a coarse-grained compact type A (CTA) CAI from the $CV3_{an}$ chondrite NWA 7891; this

CAI features a spinel-rich rim and an interior abundant in melilite that encloses some perovskite (Pv) grains. ZT5 is a coarse-grained CAI from the $CV3_{an}$ chondrite NWA 7891; it contains spinel, pyroxene, melilite, and anorthite. ZT7 is a coarse-grained CTA CAI from the $CV3_{ox}$ chondrite NWA 3118; this CAI features a spinel-rich rim and an interior abundant in melilite that encloses grains of pyroxene, perovskite, and spinel. ZT8 is a coarse-grained CAI from the $CV3_{ox}$ chondrite NWA 3118 that most closely resemble a CTA CAI; it features abundant melilite enclosing grains of pyroxene and spinel. ZT9 is a fine-grained spinel-rich inclusion from the $CV3_{ox}$ chondrite NWA 3118.

2.2.2. Sample Extraction

All sample handling and extraction of the ZT CAIs was conducted under clean conditions in the Isotope Cosmochemistry and Geochronology Laboratory (ICGL) at ASU; sample handling and extraction of other CAIs studied here (Allende CAIs and Simpson CAIs) was described by Brennecka et al. (2010; 2017) and Shollenberger et al. (2018a). The ZT CAIs were extracted from meteorite slabs using clean dental tools under a microscope, and care was taken to ensure that matrix material was not included in the extracted samples. Because Ti is a weight percent element in CAIs and is significantly enriched relative to the average chondrite matrix composition, the isotopic compositions of these extracted CAIs are unlikely to be affected by the incorporation of small amounts of matrix material. To ensure sufficient sample material for the isotopic analyses, the majority of each CAI was extracted for those analyses; however, an effort was made to reserve representative fractions of each CAI for characterization (described in the section above).

2.2.3. Analytical Methods

2.2.3.1 Clean Laboratory Reagents

To ensure low procedural blanks, all reagents used during the course of this work were obtained or prepared as follows. We obtained SEASTAR™ Hydrofluoric (HF) acid and VWR BDH ARISTAR® ULTRA hydrogen peroxide (H_2O_2). Nitric acid (HNO_3) was twice distilled from trace metal grade acid using the sub-boiling Savillex DST-1000 Acid Purification System. Hydrochloric acid (HCl) was distilled once from trace metal grade acid using the Savillex DST-1000. To purify water used for acid dilutions and chromatography, reverse osmosis (RO) water was passed through a Millipore Super-Q® water purification system (resistivity ~18 MΩ) and a Millipore Milli-Q® water purification system with a 0.1µm final filter (resistivity >18.4 MΩ).

2.2.3.2 Sample Digestion and Concentration Measurements

The sample digestion and elemental concentration measurement procedures for the ZT CAIs is described here and was described previously for the Allende CAIs and Simpson CAIs by Brennecka et al. (2010) and Shollenberger et al. (2018a), respectively. The extracted ZT CAI samples were powdered in a clean agate mortar and pestle. The powdered samples were first treated with a 3:1 ratio of concentrated HF and HNO_3 on a hot plate, dried down, and then loaded into Parr bombs in a 2:1 ratio of concentrated HF and HNO_3. Samples were digested in Parr bombs at 190 ºC for >96 h. They were then dried down and brought into solution repeatedly in HCl, followed by HNO_3. Following digestion and dissolution, a 5% aliquot of each sample solution was reserved for measuring elemental concentrations using the Thermo Scientific iCAP-Q quadrupole

inductively coupled plasma mass spectrometer (ICPMS) in the W. M. Keck Foundation Laboratory for Environmental Biogeochemistry at ASU. Varying fractions of the remaining sample solutions (having a minimum of 5μg Ti per sample) were chemically processed to purify Ti as described below. In addition to CAI samples, we used similar procedures for dissolving and chemically processing (for Ti purification) terrestrial rock standards (BCR-2 and AGV-1) and a powdered and homogenized bulk sample of the Allende CV chondrite. Based on repeated analyses of terrestrial rock standards, we estimate an uncertainty (2SD) of ±5% for Ti and REE concentrations.

2.2.3.3 Titanium Purification Chemistry

Titanium purification was conducted via ion exchange column chromatography using TODGA and AG1-X8 resins in the ICGL at ASU after the methods of Zhang et al. (2011). The procedure we used for the Allende and Simpson CAI solutions (procedure 1) is detailed below in Table 2.2. For the ZT CAIs, we modified the first column to be pressurized for more efficient processing (procedure 2 in Table 2.2). In doing this, we replaced the Bio-Rad polypropylene column with a 2 mL Eichrom 50-100 mesh DGA resin cartridge connected to the bottom of a 30 mL BD Slip-Tip Syringe reservoir. This setup was then pressurized using clean, dry air connected via an in-house built manifold and set to a pressure that resulted in the passage of approximately 1 mL of acid per minute. We also modified the collection steps by rinsing the column with 10 mL 6N HNO_3 instead of the 12M HNO_3 + 1 wt.% H_2O_2 step. This resulted in the co-elution of Ti and Fe. An Fe separation column modified after the methods of Arnold et al. (2004) was then used to separate Ti from Fe, producing a purified Ti cut. In addition to being faster,

this modified chemistry reduces the number of HF column chemistry steps, thereby improving safety and efficiency. In both procedures described here for Ti purification, typical Ti yields exceeded 95%. The average total procedural blank for all chemical processing including sample digestion and Ti purification was ~10 ng of Ti. The CAI samples were chemically processed for Ti purification in batches of 2-5 samples; solutions of the BCR-2 or AGV-1 terrestrial rock standards and/or the bulk Allende CV chondrite were similarly processed along with each batch of CAI samples.

Table 2.2. Titanium purification chemistry methods

Procedure 1: Ti column chemistry used for Allende and Simpson CAIs

Column 1: TODGA, 50-100 mesh, 2 mL

Step	Reagent	Volume (mL)
Resin Cleaning	3M HNO_3	10
Resin Cleaning	3M HNO_3 - 1.0 wt% H_2O_2	10
Resin Cleaning	MQ H_2O	4
Conditioning	12M HNO_3	15
Load Sample	12M HNO_3	10
Elute Matrix	12M HNO_3	10
Elute Ti	12M HNO_3 - 1.0 wt% H_2O_2	10
Elute Fe	3M HNO_3	10
Elute Zr and Hf	3M HNO_3 - 0.3M HF	20
Elute REE	0.2M HF	20

Column 2: AG1-X8, 200-400 mesh, 0.8 mL

Step	Reagent	Volume (mL)
Resin Cleaning	3M HNO_3	10
Resin Cleaning	MQ H_2O	2
Resin Cleaning	0.4M HCl - 1.0M HF	6
Resin Cleaning	9M HCl - 0.01M HF	5
Resin Cleaning	MQ H_2O	5
Conditioning	4M HF	6
Load Sample	4M HF	2.5
Elute Matrix	4M HF	10
Elute V	0.4M HCl - 1.0M HF	10
Elute Ti	9M HCl - 0.01M HF	5

Procedure 2: Ti column chemistry used for ZT CAIs

Column 1: TODGA 50-100 mesh, 2 mL cartridges

Step	Reagent	Volume (mL)
Resin Cleaning	MQ H_2O	4
Conditioning	12M HNO_3	15
Load Sample	12M HNO_3	10
Elute Matrix	12M HNO_3	10
Elute Ti and Fe	6M HNO_3	10
Elute Excess Fe	3M HNO_3	10
Elute Zr and Hf	3M HNO_3- 0.3M HF	20
Elute REE	0.2M HF	20

Column 2: AG1-X8, 200-400 mesh, 1 mL

Step	Reagent	Volume (mL)
Resin Cleaning	3M HNO_3	10
Resin Cleaning	MQ H_2O	2
Resin Cleaning	6M HCl	6
Conditioning	6M HCl	6
Load Sample	6M HCl	2.5
Elute Ti	6M HCl	10
Elute Fe	0.5M HCl	10

2.2.3.4 Titanium Isotope Measurements

Titanium isotopic data were acquired with the Thermo Finnigan Neptune multicollector inductively coupled plasma mass spectrometer (MC-ICPMS) at ASU using a jet sample cone and an H-skimmer cone in high-resolution mode (i.e., with a mass resolving power >8000). Samples were introduced through an Elemental Scientific Apex-Q desolvating system attached to a self-aspirating PFA with an uptake rate of 100 μL/min. An uptake time of 90 s and a wash time between consecutive sample and standard measurements of 120 s were used. Each run for a sample, standard, or blank comprised 50 cycles with an 8 s integration time per cycle. Over the course of this study, the purified Ti samples and standards were analyzed at concentrations of 1-3 ppm, and the typical sensitivity was a ^{48}Ti signal of ~25V. Data were collected by switching between two different cup configurations. The intensities of ^{44}Ca, ^{46}Ti, ^{47}Ti, ^{48}Ti, and ^{49}Ti were measured in the first cup configuration, followed by measurement of ^{47}Ti, ^{49}Ti, ^{50}Ti, ^{51}V, and ^{52}Cr intensities with the second cup configuration. Measurements of ^{44}Ca, ^{51}V, and ^{52}Cr were used to correct for isobaric interferences on the Ti masses. All the data reduction was performed offline.

Mass-independent Ti isotopic compositions are reported relative to a SPEX Ti standard for the Allende CAIs and the NIST 3162a Ti standard for the Simpson and ZT CAIs after correction for instrumental and natural mass-dependent fractionation using sample-standard bracketing and internal normalization to ^{49}Ti/^{47}Ti applying the exponential mass fractionation law,

$$R = r\left[1 + \frac{\Delta m}{m}\right]^{\beta}$$

where R is the true isotopic ratio, r is the measured isotopic ratio, $\Delta m/m$ is the relative mass difference of the measured Ti isotopes, and β represents the instrumental mass bias. Instrumental mass bias (β) corrections were calculated using:

$$\beta = \frac{\ln\left[\frac{\left(\frac{^{49}Ti}{^{47}Ti}\right)_{true}}{\left(\frac{^{49}Ti}{^{47}Ti}\right)_{measured}}\right]}{\ln\left[\frac{M_{49}}{M_{47}}\right]}$$

where (^{49}Ti/^{47}Ti)$_{true}$ is assumed to be 0.749766 (Niederer et al., 1981), and M_{47} and M_{49} are the masses of ^{47}Ti and ^{49}Ti. Titanium isotopic anomalies are reported in ε notation, i.e., parts per ten thousand deviation from the standard, as defined below:

$$\varepsilon\ ^{i}Ti = \left[\frac{\left(^{i}Ti/_{^{47}Ti}\right)_{sample}}{\left(^{i}Ti/_{^{47}Ti}\right)_{standard}} - 1\right] * 10^{4}$$

Where i is mass 46, 48, or 50 and ratios have been internally normalized.

To assess the accuracy and precision of our methodology for Ti isotopic analyses (including chemical separation and mass spectrometry), we analyzed purified Ti from the BCR-2 or AGV-1 terrestrial rock standard as well as from a bulk sample of the Allende CV chondrite along with unknown samples during each analytical session on our MC-ICPMS.

Our external reproducibilities based on repeat measurements of NIST 3162a Ti, SPEX Ti, and BCR-2 and AGV-1 rock standards (chemically processed for Ti purification in the same way as the CAI samples) over the course of this study are ± 0.17, ± 0.07, and ± 0.17 (2SD) for ε^{46}Ti, ε^{48}Ti, and ε^{50}Ti, respectively (Fig. 2.2).

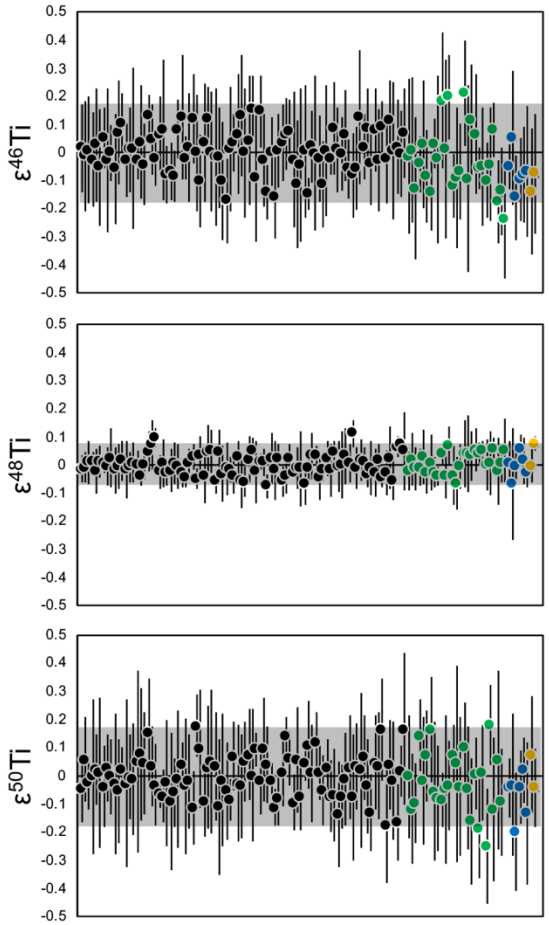

Fig. 2.2 The external reproducibilities (2SD) for ε^{46}Ti, ε^{48}Ti, and ε^{50}Ti (shown as the gray band) based on repeat runs of NIST 3162a Ti (black circles), SPEX Ti (green circles), and terrestrial rock standards BCR-2 (blue circles) and AGV-1 (orange circles). External reproducibilities (2SD) are ± 0.17 for ε^{46}Ti, ± 0.07 for ε^{48}Ti, and ± 0.17 for ε^{50}Ti.

2.3. Results

2.3.1 Rare Earth Element Concentrations

The rare earth element (REE) concentrations in the Allende CAIs and the Simpson CAIs studied here for their Ti mass-independent isotopic compositions were reported previously by Brennecka et al. (2010) and Shollenberger et al. (2018a). These data along with the REE abundances measured in this study in the ZT CAIs are given in Table 2.3 and illustrated in Fig. 2.3. Nine of these 23 CAIs show relatively unfractionated

(group I) REE patterns interpreted to represent condensation from a gas of solar composition (Martin and Mason, 1974; MacPherson, 2013). Eight CAIs show highly fractionated (group II) REE patterns that are depleted in the most refractory and most volatile REEs and are interpreted to represent a more complex condensation history (Mason and Martin, 1977). Specifically, these REE patterns are thought to result from fractional condensation in which a hibonite component containing the most refractory REEs was first removed by condensation and then the remaining REEs (except the most volatile ones) were condensed (Boynton, 1975; Davis and Grossman, 1979; MacPherson and Davis, 1994). Six samples exhibit slightly fractionated (group III) REE patterns, which are thought to be associated with multiple heating/cooling events under changing redox conditions (Ruzicka et al., 2012). In this study, all of the fine-grained CAIs exhibit fractionated REE patterns while coarse-grained CAIs (with some exceptions) generally exhibit unfractionated REE patterns.

Table 2.3. REE concentrations in the CAIs studied here, normalized to the CI chondrite values of Lodders (2003) (uncertainty is ± 5%, 2SD); data for Allende CAIs (CAIs 164–168 and CAIs 170-175) and Simpson CAIs (Homer, Marge, Bart, and Lisa) from Brennecka et al. (2010) and Shollenberger et al. (2018a), respectively.

Sample	La	Ce	Pr	Nd	Sm	Eu	Gd	Tb	Dy	Ho	Er	Tm	Yb	Lu
CAI 164	7.7	8.1	8.3	8.5	8.9	9.6	8.1	8.8	8.6	8.4	8.9	8.4	10.0	9.2
CAI 165	5.8	5.0	6.1	6.5	6.3	4.4	5.2	5.8	5.7	5.7	6.0	5.3	3.2	5.9
CAI 166	22.4	23.8	24.2	24.8	25.8	4.2	14.5	13.5	10.2	2.4	0.9	20.6	0.8	0.2
CAI 167	20.2	18.7	21.2	21.3	21.4	3.1	9.1	8.0	5.7	1.6	1.1	14.7	2.1	0.7
CAI 168	8.4	8.7	8.8	9.0	9.2	10.9	8.4	9.1	8.9	8.9	9.6	8.6	9.9	10.2
CAI 170	12.6	12.3	12.8	12.0	13.3	15.8	12.5	14.4	13.8	13.5	13.8	14.8	14.8	12.9
CAI 171	12.5	14.4	14.3	13.1	14.2	10.3	10.1	12.1	13.2	19.6	22.8	15.6	7.5	22.6
CAI 172	22.0	21.3	23.2	22.5	25.0	31.0	25.0	28.7	28.4	28.6	30.4	27.8	31.6	28.8
CAI 173	19.5	17.4	20.5	20.3	21.9	9.7	20.3	24.3	23.6	22.6	23.2	21.9	8.4	20.2
CAI 174	28.6	27.1	27.4	26.0	28.2	36.5	26.5	31.8	31.8	32.0	34.2	31.2	36.2	33.3
CAI 175	52.9	44.1	51.2	50.7	45.9	4.4	39.4	42.1	35.2	14.4	7.6	42.2	4.9	1.6
Homer	6.9	6.8	6.5	6.3	6.1	2.6	1.7	1.5	1.1	0.6	0.6	5.2	4.8	0.5
Marge	17.1	16.0	17.1	17.7	16.6	11.0	12.0	12.0	11.2	8.9	8.9	18.8	11.3	9.0
Bart	23.6	23.1	24.7	26.7	28.2	22.3	29.4	29.6	29.3	27.9	28.2	27.8	17.6	25.0
Lisa	20.7	20.4	20.2	20.7	20.6	21.9	20.1	20.2	20.4	19.8	20.4	20.3	18.9	20.2
ZT1	20.5	20.0	18.5	20.2	21.0	20.6	19.1	20.9	22.7	26.8	30.1	23.0	22.7	29.4
ZT2	19.1	20.5	20.2	22.5	23.7	13.7	9.7	8.9	6.8	3.3	2.6	20.7	12.0	2.5
ZT3	5.8	18.1	11.0	9.2	15.7	6.4	1.7	1.6	1.3	0.4	0.3	17.1	5.0	0.3
ZT4	6.7	7.5	6.5	7.3	7.3	16.5	7.7	7.2	7.2	7.0	6.8	6.3	7.4	6.4
ZT5	0.52	1.39	0.55	0.54	0.55	7.08	0.29	0.29	0.29	0.16	0.10	0.90	2.87	0.08
ZT7	15.4	14.8	15.3	17.0	18.4	23.2	15.9	16.4	17.2	16.5	17.0	18.3	14.8	16.5
ZT8	19.0	19.4	17.9	20.0	20.1	13.4	18.1	19.1	20.6	19.3	21.0	19.7	14.2	19.8
ZT9	24.3	23.4	23.6	26.1	25.2	2.8	11.9	9.3	6.1	1.2	0.5	20.2	2.1	0.2

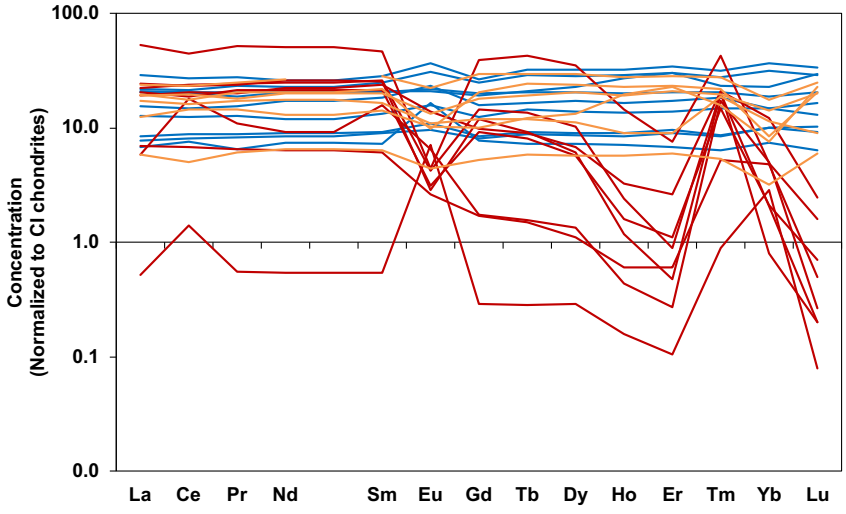

Fig. 2.3. REE abundances in the CAIs in this study normalized to REE abundances in CI chondrites (Lodders, 2003). Blue lines represent CAIs with unfractionated REE patterns (group I), orange lines represent CAIs with slightly fractionated REE patterns (group III), and red lines represent CAIs with fractionated REE patterns (group II) (Martin and Mason, 1974; Mason and Martin, 1977; Mason and Taylor, 1982). Data for the Allende CAIs and Simpson CAIs are reproduced from Brennecka et al. (2010) and Shollenberger et al. (2018a), respectively.

2.3.2 Titanium Isotopic Compositions

The mass-independent Ti isotopic compositions (internally normalized to $^{49}Ti/^{47}Ti = 0.749766$ and expressed in ε notation defined in Eq. 3 above) for each of the 23 CAIs studied here are given in Table 2.4. The $\varepsilon^{46}Ti$ values range from +1.12 (± 0.30) to +1.98 (± 0.17) for the Allende CAIs analyzed here and range from +1.21 (± 0.35) to +1.83 (± 0.17) for the other CV3 and CK3 CAIs. The $\varepsilon^{48}Ti$ values range from +0.22 (± 0.11) to +0.49 (± 0.12) for the Allende CAIs and from +0.15 (± 0.21) to 0.52 (± 0.07) for the other CV3 and CK3 CAIs. The $\varepsilon^{50}Ti$ values (shown in Fig. 2.4) range from +7.74 (± 0.17) to +9.70 (± 0.38) for the Allende CAIs and from +8.88 (± 0.17) to +11.43 (± 0.17) for the other CV3 and CK3 CAIs.

Also shown in Table 2.4 are the mass-independent Ti isotopic compositions of the terrestrial rock standards and the bulk sample of the Allende CV chondrite. We note that our data for the terrestrial rock standards BCR-2 and AGV-1 do not show any Ti isotopic anomalies within the uncertainties. Furthermore, our data for the Allende bulk sample are consistent with the range of previously reported values (Leya et al., 2007; Trinquier et al., 2009; Zhang et al., 2011). These results demonstrate the accuracy of our methodologies (chemical processing and mass spectrometry) for Ti isotopic analyses.

Table 2.4. Titanium isotopic compositions (normalized to $^{49}Ti/^{47}Ti = 0.749766$) of the CAIs studied here, as well as of 4 aliquots of bulk Allende CV3 chondrite and 6 aliquots of the BCR-2 and 2 aliquots of the AGV-1 terrestrial rock standards. The reported error is either the internal error (2SE) based on the number of runs (n) of each sample or the external reproducibility (2SD) shown in Fig. 2.2, whichever is larger.

Sample	Type	REE Pattern	$\varepsilon^{46}Ti$	$\varepsilon^{48}Ti$	$\varepsilon^{50}Ti$	n
CAI 164	Coarse, B	Group I	1.48 ± 0.17	0.43 ± 0.08	9.19 ± 0.22	3
CAI 165	Coarse, B/A1	Group III	1.80 ± 0.17	0.37 ± 0.07	9.20 ± 0.20	3
CAI 166	Fine-grained	Group II	1.36 ± 0.28	0.37 ± 0.07	8.67 ± 0.31	3
CAI 167	Fine-grained	Group II	1.54 ± 0.20	0.31 ± 0.07	8.55 ± 0.17	3
CAI 168	Coarse, A	Group I	1.12 ± 0.30	0.32 ± 0.09	9.00 ± 0.35	3
CAI 170	Coarse, B1	Group I	1.98 ± 0.17	0.44 ± 0.18	9.70 ± 0.22	3
CAI 171	Coarse, B	Group III	1.24 ± 0.17	0.22 ± 0.11	7.74 ± 0.17	3
CAI 172	Coarse, B	Group I	1.64 ± 0.17	0.35 ± 0.07	9.55 ± 0.17	3
CAI 173	Fine-grained	Group III	1.56 ± 0.17	0.31 ± 0.12	9.11 ± 0.25	3
CAI 174	Coarse, B	Group I	1.62 ± 0.17	0.36 ± 0.07	9.06 ± 0.17	3
CAI 175	Fine-grained	Group II	1.84 ± 0.23	0.49 ± 0.12	9.59 ± 0.28	3
Homer	Coarse, C	Group II	1.80 ± 0.17	0.15 ± 0.21	11.43 ± 0.17	6
Marge	Coarse, B	Group III	1.68 ± 0.17	0.50 ± 0.22	9.33 ± 0.19	6
Bart	Coarse, C	Group III	1.60 ± 0.17	0.47 ± 0.14	9.37 ± 0.19	6
Lisa	Coarse, B1	Group I	1.68 ± 0.17	0.48 ± 0.15	9.43 ± 0.17	6
ZT1	Coarse, B1	Group I	1.21 ± 0.35	0.36 ± 0.07	9.50 ± 0.17	2
ZT2	Coarse, B1	Group II	1.63 ± 0.17	0.46 ± 0.09	9.07 ± 0.17	3
ZT3	Fine-grained	Group II	1.69 ±0.17	0.38 ± 0.07	10.68 ± 0.17	3
ZT4	Coarse, CTA	Group I	1.72 ± 0.17	0.52 ± 0.07	9.30 ± 0.17	6
ZT5	Coarse	Group II	1.40 ± 0.39	0.34 ± 0.07	9.04 ± 0.17	2
ZT7	Coarse, CTA	Group I	1.53 ± 0.17	0.40 ± 0.07	8.88 ± 0.17	3
ZT8	Coarse, CTA	Group III	1.56 ± 0.17	0.43 ± 0.07	9.18 ± 0.17	3
ZT9	Fine-grained	Group II	1.83 ± 0.17	0.29 ± 0.07	10.64 ± 0.17	6
Bulk Allende[1]			0.47 ± 0.34	-0.08 ± 0.23	3.08 ± 0.17	3
Bulk Allende[2]			0.52 ± 0.29	-0.01 ± 0.07	3.39 ± 0.17	5
Bulk Allende[2]			0.48 ± 0.17	-0.02 ± 0.07	3.40 ± 0.24	2
Bulk Allende[2]			0.57 ± 0.17	0.00 ± 0.07	3.13 ± 0.25	25
BCR-2[1]			-0.05 ± 0.17	0.01 ± 0.07	-0.04 ± 0.17	5
BCR-2[1]			0.05 ± 0.17	-0.07 ± 0.20	-0.03 ± 0.25	3
BCR-2[2]			-0.16 ± 0.17	0.00 ± 0.07	-0.20 ± 0.21	5
BCR-2[2]			-0.09 ± 0.17	0.06 ± 0.07	-0.04 ± 0.17	5
BCR-2[2]			-0.08 ± 0.17	0.02 ± 0.09	0.02 ± 0.12	5
BCR-2[2]			-0.07 ± 0.23	-0.03 ± 0.07	-0.13 ± 0.25	5
AGV-1[2]			-0.14 ± 0.23	0.00 ± 0.07	0.08 ± 0.21	5
AGV-1[2]			-0.07 ± 0.21	0.08 ± 0.09	-0.04 ± 0.17	5

[1]Sample processed using procedure 1 [2]Sample processed using procedure 2 (procedures are defined in section 2.3.3 and given in Table 2.2).

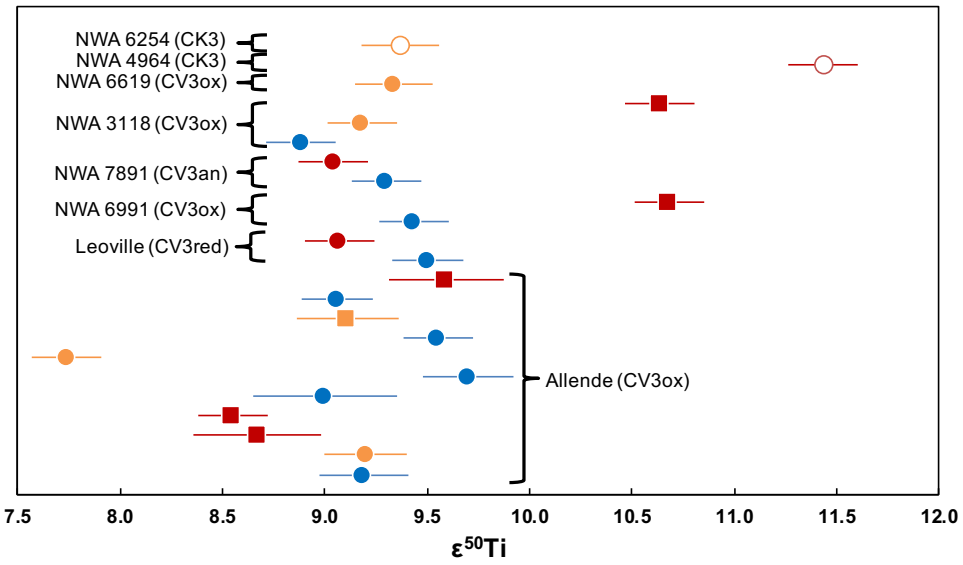

Fig. 2.4. The ε^{50}Ti values for fine-grained (squares) and coarse-grained (circles) CAIs analyzed here from the CV (filled symbols) and CK (open symbols) chondrites. Blue symbols represent CAIs with unfractionated (group I) REE patterns, orange symbols represent CAIs with slightly fractionated REE (group III) patterns, and red symbols represent CAIs with fractionated (group II) REE patterns.

The ε^{50}Ti values measured in our samples are within with the range established by previous studies of CAIs from CV, CO, CM, and ordinary chondrites (Fig. 2.5). However, the narrower range in our study could be a sampling issue given the number of CAIs analyzed here. Nevertheless, the median ε^{50}Ti value of the CAIs reported in our study is ~9, similar to that of all previously measured CAIs in the literature (Heydegger et al., 1979; Niederer et al., 1980, 1981, 1985; Niemeyer and Lugmair, 1981, 1984; Loss et al., 1994; Chen et al., 2009; Leya et al., 2009; Trinquier et al., 2009; Williams et al., 2016; Simon et al., 2017; Davis et al., 2018; Ebert et al., 2018; Render et al., 2019).

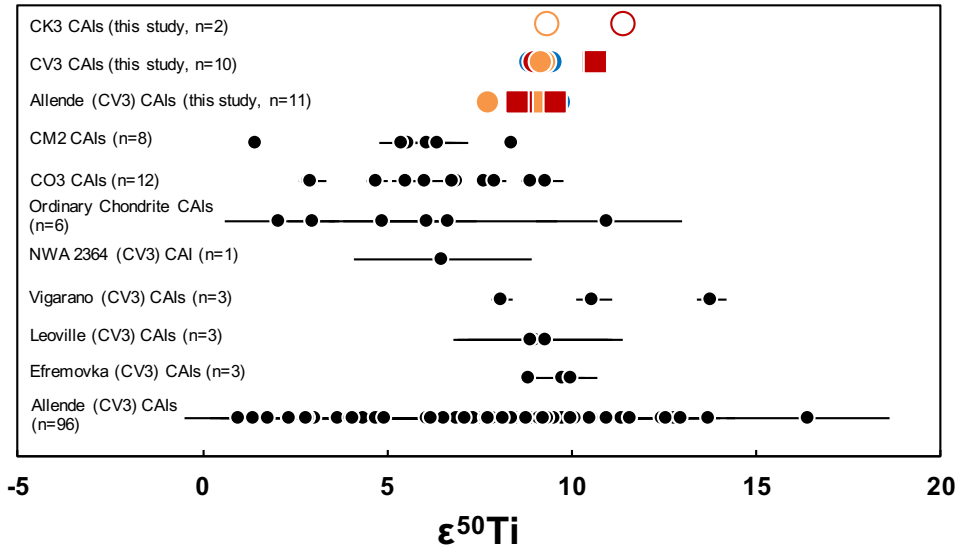

Fig. 2.5. ε^{50}Ti values shown for CAIs reported in this study (colored symbols) and in previous studies (black symbols). Data for previously studied CAIs (black symbols) are from CV3 chondrites Allende (Heydegger et al., 1979; Niederer et al., 1980, 1981, 1985; Niemeyer and Lugmair, 1981, 1984; Chen et al., 2009; Leya et al., 2009; Trinquier et al., 2009; Williams et al., 2016; Simon et al., 2017; Davis et al., 2018), Leoville (Niederer et al., 1981, 1985), Efremovka (Leya et al., 2009; Trinquier et al., 2009), Vigarano (Loss et al., 1994), and NWA 2364 (Simon et al., 2017), as well as 3 ordinary chondrites (Ebert et al., 2018), 7 CO3 chondrites (Ebert et al., 2018; Render et al., 2019), and CM2 chondrite Jbilet Winselwan (Render et al., 2019). Data reported in this study (colored symbols) represent the fine-grained (squares) and coarse-grained (circles) CAIs from CV (filled symbols) and CK (open symbols) chondrites; blue symbols represent CAIs with unfractionated (group I) REE patterns, orange symbols represent CAIs with slightly fractionated REE (group III) patterns, and red symbols represent CAIs with fractionated (group II) REE patterns.

2.4. Discussion

2.4.1 The Relationship Between REE Patterns, CAI Size, and Ti Isotopic Anomalies

Differences in thermal conditions and processing in the CAI-forming region of the nebula are thought to be the cause of fractionated REE patterns in individual CAIs. These conditions could potentially cause selective destruction of isotopically distinct presolar phases (as was suggested by Trinquier et al., 2009) such that there could be a correlation between the degree of fractionation in the REEs and in the magnitude of

certain isotopic anomalies. In an effort to assess the potential relationship between REE patterns and Ti isotopic anomalies, we plot ε^{50}Ti versus chondrite-normalized La/Lu ratios (i.e., $[La/Lu]_{CI}$) for CAIs from both this study and the recent study by Davis et al. (2018) (Fig. 2.6). In general, as can be seen in Fig. 2.6, the largest ε^{50}Ti values are reported in fine-grained CAIs with fractionated REE patterns (i.e., $[La/Lu]_{CI} >> 1$). However, there does not appear to be any clear relationship between ε^{50}Ti values and the degree of fractionation of the REE patterns in CAIs. The lack of correlation between La/Lu and ε^{50}Ti suggests that the processes leading to the homogenization of isotopic anomalies in CAIs were likely distinct from the thermal conditions that created the observed REE patterns.

The $^{26}Al/^{27}Al$ ratios inferred in CAIs by MacPherson et al. (2012) suggest that although the CAI formation interval was very short (potentially extending less than ~20,000 years), thermal reprocessing of CAIs continued for as long as ~200,000 years. If, in fact, there is an age difference between fine-grained CAIs (interpreted to record the beginning of CAI formation) and coarse-grained CAIs (which may have experienced remelting and reprocessing at a somewhat later time), the observation that the highest ε^{50}Ti values are observed in fine-grained CAIs with fractionated REE patterns could indicate homogenization and dilution of the ε^{50}Ti values through time in the CAI-forming region in the solar nebula. In fact, Peters et al. (2017) reported a wider spread in W isotopic compositions in fine-grained CAIs compared to coarse-grained CAIs and suggested that this could be the result of fine-grained CAIs being less subject to homogenization processes. However, the observation that some coarse-grained (i.e., thermally reprocessed) CAIs have canonical $^{26}Al/^{27}Al$ ratios suggests that there may not

be a clear age difference between coarse-grained and fine-grained CAIs (MacPherson et al., 2017).

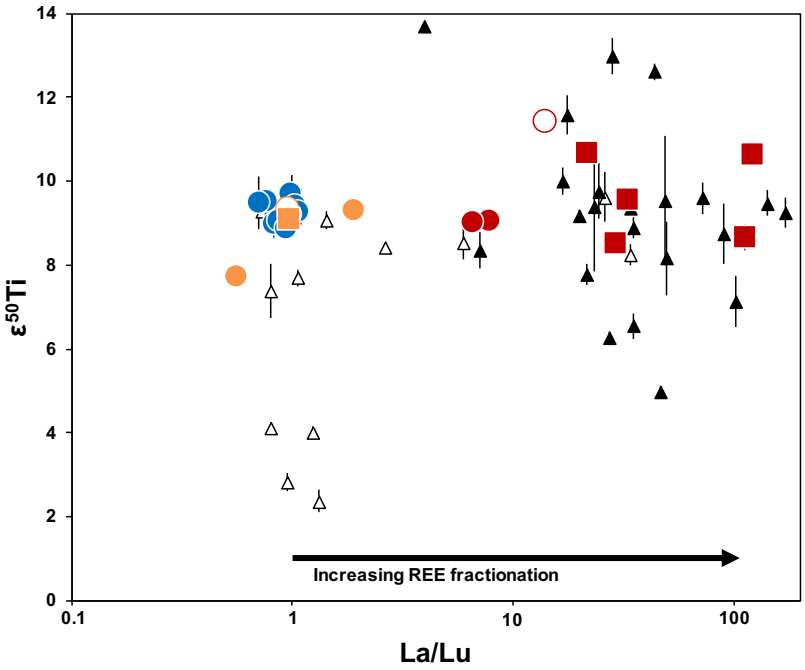

Fig. 2.6. Plot of ε^{50}Ti values versus chondrite-normalized La/Lu ratios (i.e., $[La/Lu]_{CI}$) in CAIs. Colored symbols represent the fine-grained (squares) and coarse-grained (circles) CAIs analyzed here from CV (filled symbols) and CK (open symbols) chondrites. Blue symbols represent CAIs with unfractionated (group I) REE patterns, orange symbols represent CAIs with slightly fractionated REE (group III) patterns, and red symbols represent CAIs with fractionated (group II) REE patterns. Open triangles represent coarse-grained CAIs and filled black triangles represent fine-grained CAIs from the Allende CV chondrite from Davis et al., 2018.

Another possible clue to the source of variability in the mass-independent Ti isotopic compositions of CAIs may be in their sizes. Specifically, we find a wider spread in ε^{50}Ti values in smaller CAIs (Fig. 2.7). A possible interpretation of this observation is that the larger CAIs incorporated sufficient quantities of isotopically anomalous carriers such that they have a bulk composition (i.e., with a median ε^{50}Ti value of ~9) that is broadly representative of the nebular region in which they formed. In contrast, the smaller CAIs may have sampled the nebula at a scale where the isotopically anomalous

carriers were heterogeneously distributed. However, given the limited number of exceptionally large samples (>500 mg), any interpretation of this observation must be viewed with caution.

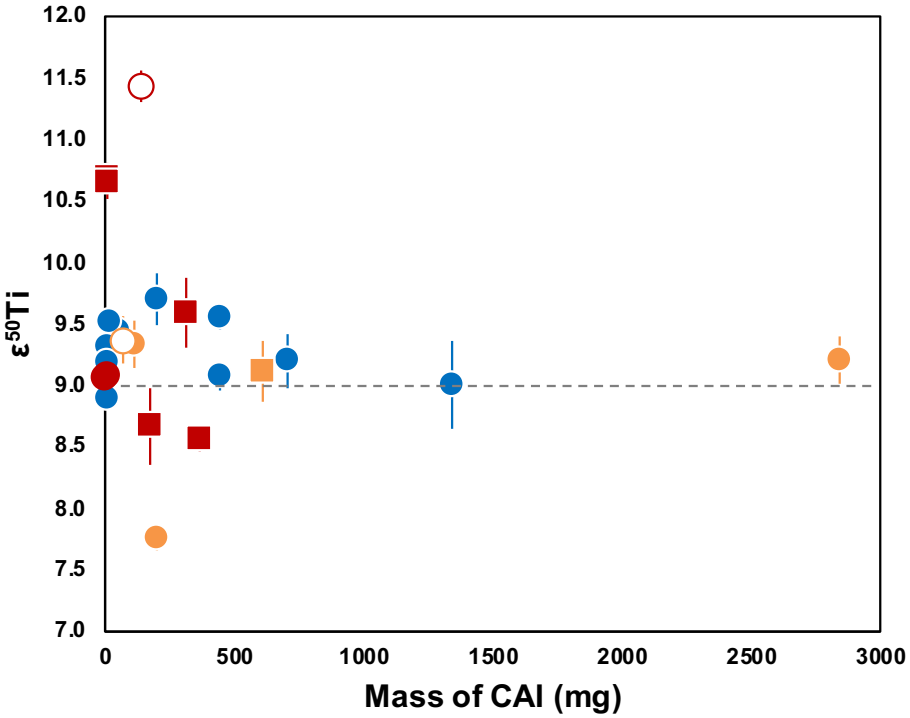

Fig. 2.7. Plot of ε^{50}Ti values versus the mass of CAIs analyzed in this study (with the median ε^{50}Ti ~9 shown as the horizontal dashed line). Colored symbols represent the fine-grained (squares) and coarse-grained (circles) CAIs analyzed here from CV (filled symbols) and CK (open symbols) chondrites. Blue symbols represent CAIs with unfractionated (group I) REE patterns, orange symbols represent CAIs with slightly fractionated REE (group III) patterns, and red symbols represent CAIs with fractionated (group II) REE patterns.

2.4.2 Implications for the CAI-forming Region in The Solar Nebula

One goal of determining the mass-independent Ti isotopic compositions of a variety of CAI types from different primitive chondritic meteorites is to ascertain whether CAIs are part of a single population that formed within a single region of the solar nebula or instead come from distinct populations that may have formed in distinct regions. We

note that even though there are resolvable differences in the Ti isotopic compositions between individual samples in this data set, these samples have a median value for their mass-independent Ti isotopic compositions (e.g., ε^{50}Ti ~9) that is indistinguishable from that of all previously analyzed CAI samples (Fig. 2.5). As such, the CAIs studied here from different CV and CK chondrites can be considered members of the same population as all previously measured CAIs from CV, CO, CM, and ordinary chondrites (Fig. 2.5), suggesting that all of these CAIs originated from a single (albeit poorly mixed) reservoir. A common source reservoir for CV, CO, CM, and ordinary chondrite CAIs was recently suggested by Ebert et al. (2018) and Render et al. (2019) based on a similar observation.

A single formation region for CAIs is also suggested by the Mo isotopic compositions of the Simpson CAIs (from CV and CK chondrites) (Shollenberger et al., 2018a), which are consistent with previously reported Mo isotopic compositions of CAIs from the Allende CV chondrite (Burkhardt et al., 2011; Brennecka et al., 2013). This single formation region is additionally supported by previous studies of O isotopes (McKeegan et al., 1998; Guan et al., 2000a) and Al-Mg systematics (Russell et al., 1996; Guan et al., 2000b), which indicate that CAIs from carbonaceous and non-carbonaceous chondrites share a common formation region and similar formation timescales.

2.4.3 The Relationship Between ^{46}Ti and ^{50}Ti

Previously reported mass-independent Ti isotopic compositions of CAIs, along with the CAI data reported here, display a correlation between ε^{46}Ti and ε^{50}Ti with a slope of 5.98 ± 0.29 and an intercept of –0.61 ± 0.46 (black line in Fig. 2.8; Leya et al., 2009; Trinquier et al., 2009; Davis et al., 2018; Render et al., 2019; this study). Bulk

samples of carbonaceous meteorites, non-carbonaceous meteorites, Earth, Moon, and Mars (e.g., Trinquier et al., 2009; Zhang et al., 2011, 2012) display a correlation between ε^{46}Ti and ε^{50}Ti with a slope of 5.38 ± 0.19 and an intercept of –0.12 ± 0.07. When the bulk Solar System materials data and CAI data are combined, the resulting correlation line has a slope of 5.60 ± 0.12 and an intercept of –0.14 ± 0.07.

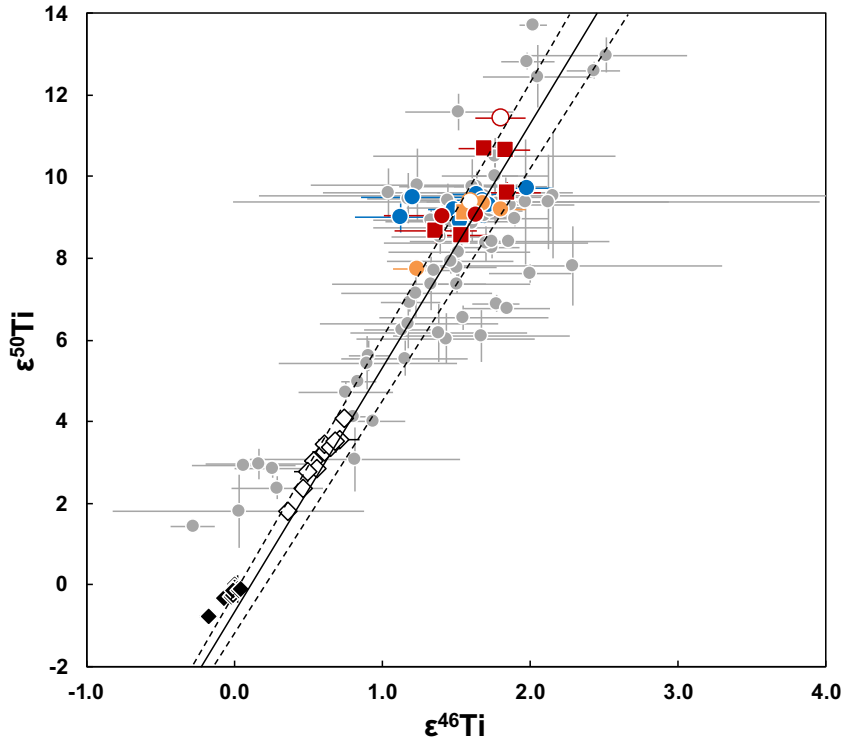

Fig. 2.8. A plot of ε^{50}Ti values versus ε^{46}Ti values for the CAIs analyzed here (colored symbols), CAIs from the literature (gray circles; Leya et al., 2009; Trinquier et al., 2009; Davis et al., 2018; Ebert et al., 2018; Render et al., 2019), and bulk samples of a variety of Solar System materials (open diamonds are carbonaceous meteorites and filled black diamonds are non-carbonaceous meteorites, Earth, Moon, and Mars; Trinquier et al., 2009; Zhang et al., 2011, 2012). The data reported in this study are for fine-grained (squares) and coarse-grained (circles) CAIs from CV (filled symbols) and CK (open symbols) chondrites. Blue symbols represent CAIs with unfractionated (group I) REE patterns, orange symbols represent CAIs with slightly fractionated REE (group III) patterns, and red symbols represent CAIs with fractionated (group II) REE patterns. The solid black line and dashed error envelope lines represent a best-fit regression for all CAIs plotted here (including CAIs from this study and the literature).

The majority of the CAIs studied here from CV and CK chondrites and previously from CV, CO, CM, and ordinary chondrites fall on the ε^{46}Ti-ε^{50}Ti correlation line for CAIs (black line in Fig. 2.8). This is additional evidence for a common source reservoir for CV, CK, CO, CM, and ordinary chondrite CAIs, as discussed above as well as by Ebert et al. (2018) and Render et al. (2019). The correlation between ε^{46}Ti and ε^{50}Ti observed in bulk meteorites and planets as well as in CAIs does not lend itself to a simple explanation since ^{46}Ti and ^{50}Ti are produced in distinct nucleosynthetic sources. Because these isotopes likely reside in different presolar carriers, Trinquier et al. (2009) suggest that it is unlikely that this correlation is simply the result of heterogeneous distribution of presolar solids in the early solar nebula. These authors argue instead that the protosolar disk was well-mixed in terms of the distribution of presolar carriers (presumably primarily silicates) that subsequently underwent secondary thermal processing, leading to selective destruction and loss of silicate presolar carriers. Davis et al. (2018) note that the correlation between ε^{46}Ti and ε^{50}Ti must reflect mixing between a ^{46}Ti- and ^{50}Ti-poor reservoir and a ^{46}Ti and ^{50}Ti-rich reservoir, and that the enriched reservoir itself must have resulted from the mixing of materials from two distinct reservoirs to account for the enrichment in both these isotopes that are produced by distinct nucleosynthetic mechanisms.

Some CAIs, however, fall off the ε^{46}Ti-ε^{50}Ti correlation line for CAIs (Fig. 2.8). Likewise, many hibonite-rich inclusions such as PLACs and SHIBs (which can have ε^{50}Ti values ~100 times larger than the CAIs studied here) do not display correlation between ε^{46}Ti and ε^{50}Ti (e.g., Kööp et al., 2016a,b). Interestingly, PLAC-like CAIs with smaller isotopic anomalies ($\left|\delta^{50}\mathrm{Ti}\right| \leq 25‰$) studied by Kööp et al. (2016b) fall on the

correlation line, while those with larger anomalies do not. According to Kööp et al. (2016b), these data indicate that while the ^{46}Ti component may have been present in the formation reservoir of these hibonite-rich inclusions, it was initially decoupled from the ^{50}Ti component. Kööp et al. (2016b) further suggest that hibonite-rich inclusions with smaller anomalies formed after the onset of the process that resulted in the coupling of ^{46}Ti and ^{50}Ti in the early Solar System, and after the objects with larger anomalies had already formed. The fact that some CAIs also fall off the correlation line may indicate that they formed immediately prior to, or during, the process that resulted in the coupling of ^{46}Ti and ^{50}Ti in the solar nebula.

2.4.4 Titanium Isotopic Anomalies as Tracers of Mixing in the Solar Nebula

The Ti isotopic composition of early Solar System materials such as CAIs can be used as a proxy for mixing in the nebular disk and as an indicator of the presolar source(s) of materials incorporated into the solar nebula. Recent work by Kööp et al. (2016b) found that in hibonite-rich CAIs, the largest ^{50}Ti anomalies (positive and negative) occurred in objects with the most ^{16}O-poor compositions. These authors suggest that this relationship could be due to a physical link between isotopically anomalous presolar components and an ^{16}O-poor reservoir, which may have been the primordial solar nebular dust. The Kööp et al. (2016b) model suggests that the large anomalies in ε^{50}Ti could have been the result of a heterogeneous distribution of anomalous isotopic carriers in the relatively unprocessed, ^{16}O-poor primordial dust reservoir. Furthermore, the progressively smaller range of ^{50}Ti anomalies in the hibonite-rich CAIs with greater ^{16}O-enrichment implied mixing between unprocessed and highly processed dust (further

implying that the nebular gas with which the highly processed dust equilibrated, presumably during thermal processing, must have been ^{16}O-rich). This is similar to a model proposed by Krot et al. (2010) suggesting that initial components of dust and gas in the solar nebula were isotopically heterogeneous, including a ^{16}O-rich primordial gas reservoir and a ^{16}O-poor primordial dust reservoir. The Krot et al. (2010) model suggests that differences in Δ^{17}O between rocky bodies in the Solar System, as well as enrichments and depletions seen in different isotope systems in different extraterrestrial materials, could result from different degrees of isotopic equilibration (due to variations in the extent of thermal processing) between the isotopically distinct gas and dust reservoirs in the solar nebula.

Therefore, according to the model of Kööp et al. (2016b), thermal processing of primordial dust (resulting in equilibration of this isotopically heterogeneous dust with nebular gas), as well as progressive mixing of unprocessed primordial dust with the highly processed dust, could cause isotopic heterogeneities in the solar nebula to homogenize over time. This model is at odds with that proposed by Trinquier et al. (2009), which contends that thermal processing would instead cause preferential volatilization of less stable isotopically anomalous carriers that were initially homogeneously distributed, thus leading to formation of isotopically anomalous nebular reservoirs. Kööp et al. (2016b) argue against the Trinquier et al. (2009) model by noting that Ti-bearing refractory phases would be among the last to evaporate and the first to recondense, thus limiting the efficiency of thermal processing as a means of creating isotopic anomalies in these elements. Leya et al. (2009) similarly challenge the Trinquier et al. (2009) model on the basis that bringing enough Ti into the vapor phase and

maintaining it there, as required by that model, would require extremely high temperatures that would likely cause most other solids to also evaporate. As such, thermal processes involving complete, or nearly complete, volatilization and recondensation are likely to be efficient in homogenizing isotopic anomalies in an initially poorly mixed reservoir and diluting them over time.

The data presented here, along with previous work, suggest that the isotopic anomalies in CAIs provide a record of the progressive homogenization through time of an isotopically heterogeneous solar nebula. As suggested by Dauphas et al. (2002), the isotopic heterogeneity of the solar nebula could either have been a primordial feature owing to heterogeneous distribution of presolar carrier phases (inherited from the interstellar medium) or instead from an initially homogeneous distribution of presolar carrier phases via nebular processes such as granular sorting or dust-gas decoupling. In either case, if Solar System materials subsequently homogenized through time, we would expect the earliest formed solids to sample the most isotopically heterogeneous early nebula and thus to record the largest isotopic anomalies. Refractory inclusions such as PLACs, PLAC-like CAIs, and FUN CAIs have low inferred initial $^{26}Al/^{27}Al$ ratios, which, combined with their large nucleosynthetic anomalies, suggest that they formed prior to the injection of ^{26}Al in the early Solar System (Wasserburg et al., 1977; Ireland, 1990; Liu et al., 2009; Kööp et al., 2016a,b).

PLACs and PLAC-like CAIs have $\varepsilon^{50}Ti$ values with a range of ~3000 (Zinner et al., 1986; Fahey et al., 1987; Hinton et al., 1987; Ireland, 1990; Sahijpal et al., 2000; Liu et al., 2009; Kööp et al., 2016b) while FUN CAIs have an $\varepsilon^{50}Ti$ range of ~300 (Niederer et al., 1985; Papanastassiou and Brigham, 1989; Loss et al., 1994; Williams et al., 2016,

2017; Kööp et al., 2018). SHIBs have variable inferred $^{26}Al/^{27}Al$ ratios (ranging from zero to near-canonical) and an $\varepsilon^{50}Ti$ range of ~1000 (Fahey et al., 1987; Ireland, 1988, 1990; Sahijpal et al., 2000; Liu et al., 2009; Kööp et al., 2016a). However, Kööp et al. (2016a) note that certain samples at the extreme end of this range may in fact be better classified as PLAC-like CAIs and that most SHIBs have an $\varepsilon^{50}Ti$ range of ~200. As discussed by Liu et al. (2012), this suggests that SHIBs may have formed while ^{26}Al was being admixed into the Solar System but was not yet homogenized and thus formed at a time intermediate between ^{26}Al-free refractory inclusions (i.e., FUN CAIs) and CAIs that are characterized by canonical initial abundances of ^{26}Al (e.g., Jacobsen et al., 2008; Kita et al., 2013) and smaller isotopic anomalies ($\varepsilon^{50}Ti$ range of ~10; Heydegger et al., 1979; Niederer et al., 1980, 1981, 1985; Niemeyer and Lugmair, 1981, 1984; Loss et al., 1994; Leya et al., 2009; Trinquier et al., 2009; Williams et al., 2016; Simon et al., 2017; Davis et al., 2018; Ebert et al., 2018; Render et al., 2019; this study). These data are consistent with progressive isotopic homogenization of the solar nebula through time and suggest that CAIs, such as those studied here, could have been formed towards the last stages of homogenization of large-scale isotopic heterogeneity in the Solar System (Fig. 2.9).

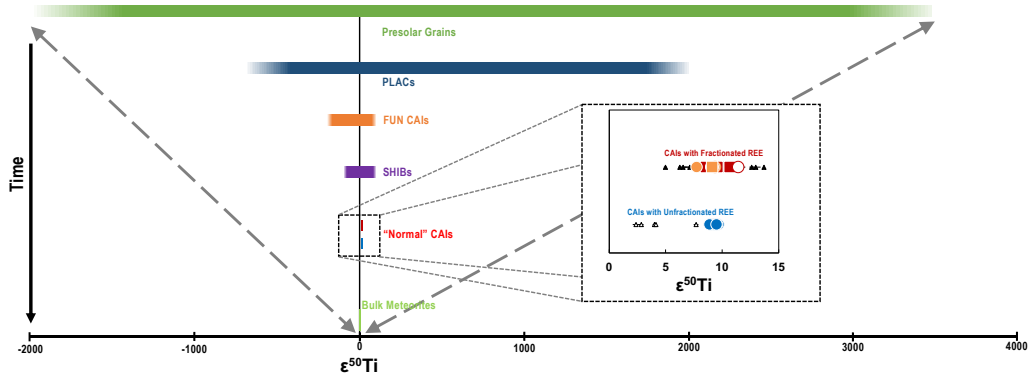

Fig. 2.9. A schematic diagram following the model of Kööp et al. (2016b). Here we show the possible relative chronology of formation of various refractory components in primitive chondritic meteorites based on the progressive homogenization through time of Ti isotopic anomalies. Data for presolar grains, PLACs, FUN CAIs, and SHIBs are from the literature (Niederer et al., 1985; Zinner et al., 1986; Fahey et al., 1987; Hinton et al., 1987; Papanastassiou and Brigham, 1989; Ireland, 1988, 1990; Ireland et al., 1991; Hoppe et al., 1994; Loss et al., 1994; Alexander and Nittler, 1999; Sahijpal et al., 2000; Amari et al., 2001a, 2001b; Huss and Smith, 2007; Zinner et al., 2007; Liu et al., 2009; Kööp et al., 2016a,b, 2018; Williams et al., 2016, 2017; Gyngard et al., 2018). Data for CAIs are from this study and Davis et al. (2018). In the inset, colored symbols represent the fine-grained (squares) and coarse-grained (circles) CAIs analyzed here from CV (filled symbols) and CK (open symbols) chondrites. Blue symbols represent CAIs with unfractionated (group I) REE patterns, orange symbols represent CAIs with slightly fractionated REE (group III) patterns, and red symbols represent CAIs with fractionated (group II) REE patterns; open triangles represent coarse-grained CAIs and filled black triangles represent fine-grained CAIs from the Allende CV chondrite from Davis et al., 2018.

Finally, it is important to consider the implications of certain elements exhibiting resolved isotopic variability between individual CAIs, while other elements do not. For example, previous analyses of several of the same CAIs studied here show indistinguishable (within the analytical uncertainties) mass-independent isotopic compositions of Sr, Ba, Nd, Sm, Er, Yb, and Hf, and these data have been interpreted to reflect a homogeneous isotopic reservoir for CAI formation (Brennecka et al., 2013; Shollenberger et al., 2018a,b). This is in contrast with the resolvable isotopic variation observed in Mo (Shollenberger et al., 2018a), Ni (Render et al., 2018) and Ti (this study)

in these same samples. The different extents of isotopic variation observed in different elements may be related to the characteristics of distinct carrier phases of these elements. For example, during thermal processing in the nebula, elements primarily sequestered in more refractory phases may have preserved some amount of isotopic variability due to incomplete homogenization, while those elements in less refractory phases may have been homogenized more effectively.

2.5. Conclusions

In this study, we measured the mass-independent Ti isotopic compositions of 23 CAIs of diverse petrologic and geochemical types (11 from the Allende CV chondrite and 12 from 7 other CV and CK chondrites) with the goal of ascertaining whether previously reported Ti isotopic values for CAIs are representative of the broader CAI-forming region. The implications of this work are as follows:

1) Our data show that there may be a greater degree of Ti isotopic variability among CAIs with fractionated REE patterns (generally fine-grained) compared to their counterparts with unfractionated REE patterns (generally coarse-grained). However, there is no significant correlation between the degree of REE fractionation and ε^{50}Ti in these CAIs, suggesting that the processes leading to homogenization of isotopic anomalies in CAIs were likely distinct from the nebular thermal processing that created the observed REE patterns.
2) The resolved variation and range in ε^{50}Ti values of the samples studied here indicate that Ti isotopic variability was present in the CAI-forming region of the early Solar System. Nevertheless, CAIs from CV and CK chondrites appear to

define a single population (i.e., characterized by a median ε^{50}Ti value of ~9) along with CAIs found in CO, CM, and ordinary chondrites. A strong correlation, similar in character to that previously reported in bulk Solar System materials, exists between ε^{46}Ti and ε^{50}Ti for most measured CAIs. Taken together, these observations imply that CAIs from CV, CK, CO, CM, and ordinary chondrites formed in a single CAI-forming region.

3) Although a strong correlation exists between ε^{46}Ti and ε^{50}Ti for the majority of CAIs, some CAIs – among those studied here and previously – fall off this correlation line. These CAIs may represent an intermediate stage in the processes responsible for homogenizing isotopic anomalies in the solar nebula and imparting the correlation between ^{46}Ti and ^{50}Ti observed in Solar System materials.
4) The Ti isotopic data for CAIs, combined with recent studies of the Ti isotopic compositions of PLACs, SHIBs, and FUN CAIs, suggest that CAIs were likely formed during the final stages of large-scale Solar System homogenization.

Acknowledgements: We thank Laurence Garvie for his assistance with the selection and acquisition of samples, Axel Wittman for his assistance with the electron microprobe analyses, and Celeste Brennecka for editorial inputs during manuscript preparation. We also thank Frederic Moynier for his editorial handling, and Stefan Peters and an anonymous reviewer for their constructive comments that improved the manuscript.

Funding: This work was supported by NASA grant NNX15AH41G to M. W. and a Sofja Kovalevskaja Award from the Alexander von Humboldt Foundation to G. A. B.

Note: This chapter appears as a published paper in *Geochimica et Cosmochimica Acta* 263, 13–30 (2019).

CHAPTER 3

CHROMIUM AND TITANIUM ISOTOPIC COMPOSITIONS OF CALCIUM-ALUMINUM-RICH INCLUSIONS: CLUES TO THE FORMATION OF DISTINCT ISOTOPIC RESERVOIRS IN THE EARLY SOLAR SYSTEM

3.1 Introduction

Calcium-aluminum-rich inclusions (CAIs) are highly refractory objects found in chondritic meteorites and are the earliest-dated solids to form in the Solar System at ~4.567 Ga (e.g., Amelin et al., 2010; Connelly et al., 2012, 2017). In addition to ancient absolute ages from Pb-Pb chronometry, the short-lived ^{26}Al-^{26}Mg chronometer has shown that most CAIs exhibit an inferred initial $^{26}Al/^{27}Al$ ratio of $\sim 5 \times 10^{-5}$ suggesting that these objects formed during a short time interval of less than 200,000 years (Jacobsen et al., 2008; MacPherson et al., 2012; Kawasaki et al. 2019; Liu et al., 2019). As such, CAIs record a snapshot of the earliest stage of the isotopic evolution of the Solar System and provide important constraints on protoplanetary disk dynamics (e.g., Desch et al., 2018). Chondritic meteorites contain a variety of refractory components such as platy hibonite crystals (PLACs), spinel-hibonite inclusions (SHIBs), and Fractionated and Unidentified Nuclear effect (FUN) CAIs that contain significantly larger mass-independent isotopic anomalies compared to the more abundant "normal" CAIs that are the focus of this study (and which we will simply refer to as CAIs from hereon). Previous studies have shown that CAIs record mass-independent anomalies in most elements, reflecting formation in a nebular isotopic reservoir distinct from those in which bulk chondrites and terrestrial planets were formed (e.g., Dauphas and Schauble, 2016). Whereas the isotopes of certain

elements show resolvable ε-level (parts per ten thousand deviation from a standard) mass-independent variability, others do not. The characterization of these isotopic anomalies is an important step towards constraining the nucleosynthetic processes that produced the ingredients of the solar protoplanetary disk as well as the mixing processes that occurred during the early evolution of our Solar System. Isotopic anomalies in the Fe-peak elements ($22 \leq Z \leq 30$) are of particular importance because their nucleosynthetic origin in the late evolution of massive stars and supernovae aid in identifying potential contributions from these materials to the early Solar System.

The isotopic compositions of Cr and Ti have previously been utilized as important tracers of Solar System dynamics and evolution. The neutron-rich isotopes of these two elements, ^{54}Cr and ^{50}Ti, are particularly useful because they are produced in variable amounts in Type Ia, Type II, and electron-capture supernovae (e.g., Clayton, 2003; Wanajo et al., 2013; Davis et al., 2018) and can be used to trace the incorporation of materials from these sources into the early Solar System as well as the genetic relationships between meteorite parent bodies. A significant recent finding was the discovery of an isotopic dichotomy between "non-carbonaceous chondritic" (NC) and "carbonaceous chondritic" (CC) Solar System materials that is observed in a wide range of isotope systems, including Cr and Ti (Warren, 2011). These two distinct isotopic reservoirs are suggested to be represented by objects of inner (NC) and outer (CC) Solar System provenance that were likely separated because of the formation and growth of Jupiter (Kruijer et al., 2017). An open question is whether this isotopic dichotomy reflects isotopic heterogeneity inherited from the parent molecular cloud via infalling material, or if it resulted from thermal processing, transport, and mixing occurring within the

protoplanetary disk. As recordkeepers of the earliest-sampled nebular reservoir in the nascent Solar System, CAIs may hold important clues to answering this question. The potential role of CAIs in the formation of planetary-scale isotopic reservoirs has been investigated in recent work through the measurement of anomalies in multiple isotope systems within the same CAIs (e.g., Brennecka et al. 2013; 2020). The models of Burkhardt et al. (2019) and Nanne et al. (2019) suggest that CAIs record the isotopic composition of infalling material from the molecular cloud into our protoplanetary disk, and they may therefore reveal important information about the timing of infall and the nucleosynthetic sources contributing to this material.

The formation age of CAIs is commonly used to define "time zero" for early Solar System chronology, and it is important to consider their time of formation in the broader context of Solar System formation processes. Solar mass stars are thought to form from collapse of denser regions of their parent molecular clouds and transition to pre-main sequence stars within ~1 million years (Cieza et al., 2007). This is longer than the time period of formation recorded by CAIs, which have previously been associated with the period of collapse and accretion on to the protostar (class 0) (Wood, 2004; Connelly et al., 2012) or the transition of the evolved protostar (class I) to the T-Tauri stage of the proto-Sun (class II) ~1 million years later (Ciesla et al., 2010; Dauphas et al., 2011; Yang and Ciesla, 2012; Brennecka et al., 2020). A link between CAIs and particular stages of star formation can help to further place CAI formation and the formation of the NC and CC isotopic reservoirs into astrophysical context.

Although CAIs from CV, CK, CM, CO, and ordinary chondrites have been analyzed previously for their Ti isotopic compositions, only CAIs from two CV

chondrites, Allende and Vigarano, have been analyzed previously for their Cr isotopic compositions. It is noted that CV3 chondrites, particularly Allende, are known to have been altered by secondary processes on their parent body (e.g., Krot et al., 1998). Furthermore, very few of the CAIs from Allende and Vigarano have been measured previously for both their Cr and Ti isotopic compositions. Therefore, it is important to measure both the Cr and Ti isotopic compositions of CAIs from multiple chondritic meteorites to accurately characterize the compositional range of CAIs in ε^{50}Ti vs. ε^{54}Cr space and to evaluate the types of materials inherited by the solar protoplanetary disk, the relationship between the timing of CAI formation and the different stages of star formation, and the role of CAIs in formation of the planetary-scale isotopic dichotomy in the early Solar System. In this work, we measured both Cr and Ti isotopic compositions in the same suite of CAIs from a variety of CV and CK chondrites; this work represents the first reported Cr isotopic composition of a CAI from a CK chondrite.

3.2 Samples and Methods

3.2.1 Sample Description

The sample set studied here includes 11 CAIs from 6 CV chondrites (including oxidized and reduced subgroups) and 1 CK chondrite. The Ti isotopic compositions of six of these CAIs were measured previously by Torrano et al. (2019): ZT1 and ZT2 from $CV3_{red}$ Leoville, ZT3 from $CV3_{ox}$ NWA 6991, ZT5 from $CV3_{ox}$ NWA 7891, and ZT7 and ZT8 $CV3_{ox}$ NWA 3118. Five additional new CAIs were obtained for this work: ZT6 from NWA 2900 (classified as a CV3 but reclassified as a CK3.8 by Torrano et al., 2020), ZT10 from $CV3_{ox}$ NWA 6991, ZT13 and ZT14 from $CV3_{ox}$ Axtell, and Saguaro

from $CV3_{red}$ NWA 5508. A summary of the characteristics of these samples is shown in Table 3.1.

Table 3.1. List of the CAIs included in this study.

CAI	Meteorite	Mass (mg)	CAI Type	REE Pattern
ZT1	Leoville ($CV3_{red}$)	18	CG, B1	Group I
ZT2	Leoville ($CV3_{red}$)	42	CG, B1	Group II
ZT3	NWA 6991 ($CV3_{ox}$)	8.8	FG	Group II
ZT5	NWA 7891 ($CV3_{ox}$)	1.7	CG	Group II
ZT6	NWA 2900 (CK3.8)	30.5	CG	Group I
ZT7	NWA 3118 ($CV3_{ox}$)	5.7	CG, CTA	Group I
ZT8	NWA 3118 ($CV3_{ox}$)	8.4	CG, CTA	Group III
ZT10	NWA 6991 ($CV3_{ox}$)	7.0	FG	Group II
ZT13	Axtell ($CV3_{ox}$)	20.2	CG	Group I
ZT14	Axtell ($CV3_{ox}$)	24.4	FG	Group II
Saguaro	NWA 5508 ($CV3_{red}$)	220.3	CG, B2	Group I

$CV3_{ox}$ = CV3 oxidized subgroup; $CV3_{red}$ = CV3 reduced subgroup; CG = coarse-grained; FG = fine-grained; CTA = compact type A.

3.2.2 Sample Extraction

All sample handling was conducted in the Isotope Cosmochemistry and Geochronology Laboratory (ICGL) at Arizona State University (ASU). The extraction of CAIs ZT1, ZT2, ZT3, ZT5, ZT7, and ZT8 was described by Torrano et al. (2019) and the CAIs ZT6, ZT10, ZT13, ZT14, and Saguaro, which are reported here for the first time, were extracted following the same procedures.

3.2.3 Analytical Methods

3.2.3.1 Sample Digestion and Concentration Measurements

The extracted CAIs were powdered using a clean agate mortar and pestle. Samples were treated with a 3:1 ratio of concentrated HF and HNO_3 on a hot plate, dried down, and then loaded into Parr bombs in a 2:1 ratio of concentrated HF and HNO_3. Parr bombs were placed in an oven at 190ºC for >96 h. Following Parr bomb digestion,

samples were dried down and then brought into solution repeatedly in HCl followed by HNO_3. An aliquot of ~5% of each sample solution was reserved for elemental concentration measurements using the Thermo Scientific iCAP-Q quadrupole inductively coupled plasma mass spectrometer in the W. M. Keck Foundation Laboratory for Environmental Biogeochemistry. Aliquots of the remaining ~95% of the sample solutions were then processed for Cr and Ti purification. Similar digestion procedures were used for the terrestrial rock standards BCR-2 and AGV-1 and a powdered and homogenized bulk sample of the Allende CV3 chondrite. Based on repeated analyses of standards, we estimate an uncertainty (2SD) of ±5% for elemental concentrations.

3.2.3.2 Chromium Purification via Column Chromatography

All Cr purification chemistry was conducted in the ICGL at ASU following the methods of Yamakawa et al. (2009) with modifications based on Larsen et al. (2016) to control Cr speciation and thereby improve Cr elution yields (Table 3.2). The Cr yields of all samples and standards exceeded 90%, and the average total procedural blank was less than 2 ng of Cr. Briefly, the first column separated Fe from other elements and used 1 mL of pre-cleaned Bio-Rad AG1-X8 200-400 mesh anion resin loaded onto a Bio-Rad polypropylene column (h = 42 mm, d = 5.5 mm). The sample was loaded onto the column in 1 mL of 6M HCl and Cr was eluted immediately in 5 mL of 6M HCl, along with Ni, Na, Ti, V, Mg, Ca, and Al. The final steps removed Fe (in 8 mL of 0.5M HCl) and Zn (in 6 mL of 3M HNO_3). The second column separated Cr from Ni and rare earth elements (REEs) using 1 mL of Bio-Rad AG50W-X8 200-400 mesh anion resin loaded onto a Bio-Rad polypropylene column. The speciation of Cr in chloride form must be

controlled to ensure proper elution of Cr on this column, as discussed by Larsen et al. (2016). In order to promote the formation of Cr(III)-Cl complexes, samples were fluxed on the hot plate in ~0.2 mL of concentrated HCl for 5 h at 120 ºC (with samples slowly rolled every ~20 minutes to ensure all solution remained in a bead in the bottom of the Teflon beaker) prior to loading on the second column. Once removed from the hot plate, sample solutions were diluted with MQ H_2O to make 2.4 mL of 1M HCl and immediately loaded on the second column. The Cr was eluted in 7 mL of 1M HCl, and remaining elements were eluted in 8 mL of 6M HCl. The third column further purified Cr from remaining elements including Na, Ti, and V, using 0.3 mL of Bio-Rad AG1-X8 200-400 mesh anion resin loaded onto a column made from a heat shrink Teflon tube (h = 23.3 mm, d = 4.05 mm). The speciation of Cr is also important for this column, so all samples were first placed in 1.5 mL of 1M HNO_3 and heated in an oven at 50 ºC for 24 h. Samples were then removed from the oven, diluted with MQ H_2O to make 3 mL of 0.5M HNO_3, and immediately loaded onto the column. After elution of Na, Ti, and V (plus other remaining elements) in 0.5M HNO_3, 0.5M HF, and 1M HCl, Cr was eluted in 5 mL of 6M HCl.

3.2.3.3 Additional Cr Purification to Prevent Isobaric Interference Effects

Total removal of Fe is critically important for the accurate high-precision measurement of Cr isotopes (specifically $^{54}Cr/^{52}Cr$) using a multicollector inductively coupled plasma mass spectrometer (MC-ICPMS) because ^{54}Fe is a direct isobaric interference on ^{54}Cr. Any residual Fe originating from the sample which is not completely separated during column chemistry is likely to be isotopically fractionated,

complicating the ability to accurately account for the interference of ^{54}Fe on ^{54}Cr. In Fig. 3.1, we have calculated the effect of isotopically mass-fractionated residual Fe ($\delta^{56}Fe$ = –1, –2, –5, and –10 ‰) on measured $\varepsilon^{54}Cr$ values following a typical Fe interference correction assuming unfractionated $^{56}Fe/^{54}Fe$ (i.e. $\delta^{56}Fe$ = 0 ‰) and an identical isotopic instrumental mass bias for Cr and Fe. From these calculations, we conclude that a ratio of $^{56}Fe/^{52}Cr < 5\times10^{-4}$ should be attained to ensure no effect on $\varepsilon^{54}Cr$ beyond the analytical uncertainty.

Because of the small amount of Cr purified from these samples (~1–10 µg), attaining $^{56}Fe/^{52}Cr < 5\times10^{-4}$ requires maximum Fe blanks of ~0.5–5 ng. In order to ensure that these blank requirements were met for all samples, we added a post-column Fe-removal step to our Cr purification procedure. Following the third column, sample Cr cuts were brought up in a solution of 100µL of 10M HCL and approximately 10 beads of Bio-Rad AG1-X8 20-50 mesh anion resin were added. The sample beakers were then placed on an orbital shaker for 6 h to ensure sufficient bead interaction with the acid. Sample solutions were then pipetted out of the beaker containing the beads and added to new clean Teflon beakers. This method reliably achieved $^{56}Fe/^{52}Cr < 5\times10^{-4}$ (measured via MC-ICPMS) for all samples.

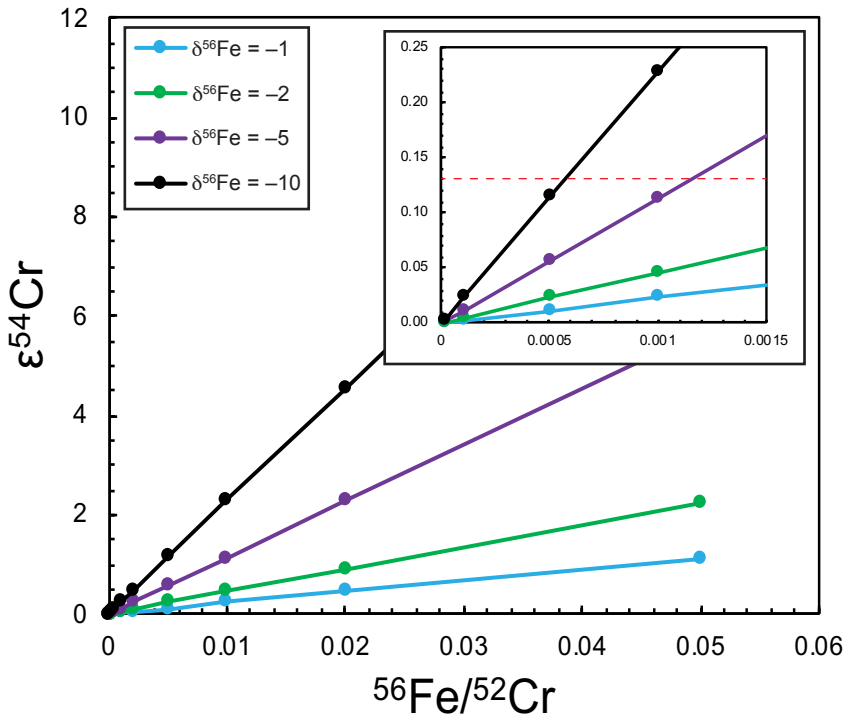

Fig. 3.1. Theoretical calculations of $\varepsilon^{54}Cr$ vs. $^{56}Fe/^{52}Cr$ show the potential effects of residual Fe on isotopic measurements of Cr via MC-ICPMS for varying degrees of Fe isotopic fractionation on the column. Inset shows finer scale plot with red dashed line indicating the analytical precision of the $\varepsilon^{54}Cr$ measurements. These calculations show that $^{56}Fe/^{52}Cr < 5\times10^{-4}$ should be attained for all samples prior to measurement.

Table 3.2. Cr purification procedure used in this study.

Column 1: AG1-X8, 200-400 mesh anion resin, 1 mL		
Step	Reagent	Volume (mL)
Condition Resin	3M HNO_3	10
Condition Resin	MQ H_2O	18
Condition Resin	6M HCl	12
Conditioning	6M HCl	6
Load Sample	6M HCl	1
Elute Cr	6M HCl	4
Elute Fe	0.5M HCl	8
Elute Zn	3M HNO_3	6

Column 2: AG50W-X8, 200-400 mesh cation resin, 1 mL		
Step	Reagent	Volume (mL)
Condition Resin	6M HCl	16
Condition Resin	MQ H_2O	32
Load Sample	1M HCl	2.4
Elute Cr	1M HCl	4.6
Strip Column	6M HCl	8

Column 3: AG50W-X8, 200-400 mesh cation resin, 0.3 mL		
Step	Reagent	Volume (mL)
Condition Resin	6M HCl	9
Condition Resin	MQ H_2O	12
Load Sample	0.5M HNO_3	3
Elute Na, Ti, V	0.5M HNO_3	1
Elute Na, Ti, V	0.5M HF	3
Elute Na, Ti, V	1M HCl	5
Elute Cr	6M HCl	5

Fe removal: AG1-X8 20-50 mesh anion resin, ~10 beads		
Step	Reagent	Volume (mL)
Fe Removal	10M HCl	0.100

3.2.3.4 Cr Isotopic Analyses

Chromium isotopic measurements were conducted on a Thermo Finnigan Neptune MC-ICPMS at ASU using a jet sample cone and an H-skimmer cone in high-resolution mode (i.e., with a mass resolving power >8000). Samples were introduced through an Elemental Scientific Apex-Q desolvating system attached to a self-aspirating PFA with an uptake rate of 100 µL/min. An uptake time of 90 s and a wash time between consecutive sample and standard measurements of 120 s were used. Each run for a sample, standard, or blank comprised 36 cycles with an 8 s integration time per cycle.

Purified Cr samples and standards were analyzed at 800 ppb, and the typical sensitivity for ^{52}Cr was ~25V. The intensities of ^{50}Cr, ^{52}Cr, ^{53}Cr, and ^{54}Cr were measured, along with ^{49}Ti, ^{51}V, and ^{56}Fe to monitor and correct for isobaric interferences. All data reduction was performed offline.

Mass-independent Cr isotopic compositions are reported relative to the SRM 979 Cr standard after correction for instrumental and natural mass-dependent fractionation using sample-standard bracketing and internal normalization to ^{50}Cr/^{52}Cr applying an exponential mass fractionation law and a ^{50}Cr/^{52}Cr ratio of 0.051859 (Shields et al., 1966). Chromium isotopic anomalies are reported in ε notation, i.e., parts per ten thousand deviation from the standard, as defined below:

$$\varepsilon\,^{x}Cr = \left[\frac{\left(^{x}Cr/_{^{52}Cr}\right)_{sample}}{\left(^{x}Cr/_{^{52}Cr}\right)_{standard}} - 1\right] * 10^{4}$$

Where x is mass 53 or 54 and ratios have been internally normalized.

To assess the accuracy and precision of our methodology for Cr isotope analyses (including chemical separation and mass spectrometry), we purified and measured Cr from bulk homogenized Allende CV3 chondrite alongside samples. Our external reproducibility (2SD) based on repeat measurements of pure Cr standards as well as terrestrial and meteoritic standards in our laboratory is ± 0.06 for ε^{53}Cr and ± 0.13 for ε^{54}Cr.

3.2.3.5 Titanium Purification and Isotopic Analyses

The Ti purification of the new CAIs presented here was conducted in the ICGL at ASU following "Procedure 2" described by Torrano et al. (2019) and shown in Table 2.2

of this dissertation. Ti yields exceeded 95% for all samples and standards with a total procedural blank of <10 ng of Ti. The BCR-2 and AGV-1 terrestrial rock standards and the homogenized bulk Allende CV chondrite were similarly processed alongside each batch of CAI samples.

Titanium isotopic measurements of the CAIs reported here for the first time were conducted using the Thermo Finnigan Neptune MC-ICPMS at ASU using a jet sample cone and an H-skimmer cone in high-resolution mode. Samples were introduced through a Cetac Aridus II desolvating nebulizer attached to a self-aspirating PFA with an uptake rate of 100 μL/min. An uptake time of 90 s and a wash time between consecutive sample and standard measurements of 120 s were used. Each run for a sample, standard, or blank comprised 50 cycles with an 8 s integration time per cycle. Purified Ti samples and standards were analyzed at a concentration of 1 ppm, and the typical sensitivity resulted in a ^{48}Ti signal of ~25V. Data were collected by switching between two different cup configurations: The intensities of ^{44}Ca, ^{46}Ti, ^{47}Ti, ^{48}Ti, and ^{49}Ti were measured in the first cup configuration, followed by measurement of ^{47}Ti, ^{49}Ti, ^{50}Ti, ^{51}V, and ^{52}Cr intensities with the second cup configuration. Intensities of ^{44}Ca, ^{51}V, and ^{52}Cr were used to correct for isobaric interferences on the Ti masses. All data reduction was performed offline. Mass-independent titanium isotopic compositions are reported relative to the NIST 3162a Ti standard after correction for instrumental and natural mass-dependent fractionation using sample-standard bracketing and internal normalization to ^{49}Ti/^{47}Ti applying an exponential mass fractionation law and a ^{49}Ti/^{47}Ti ratio of 0.749766 (Niederer et al., 1981). Titanium isotope anomalies are also reported in ε notation, as defined below:

$$\varepsilon\,^{x}Ti = \left[\frac{\left(^{x_{Ti}}/_{^{47}Ti}\right)_{sample}}{\left(^{x_{Ti}}/_{^{47}Ti}\right)_{standard}} - 1\right] * 10^{4}$$

Where x is mass 46, 48, or 50 and ratios have been internally normalized. Our external reproducibility (2SD) based on repeat measurements of pure Ti standards as well as terrestrial and meteoritic standards in our laboratory are ± 0.17 for ε^{46}Ti, ± 0.07 ε^{48}Ti, and ± 0.17 for ε^{50}Ti (2SD).

3.3. Results

3.3.1 Rare Earth Element Concentrations

The REE concentrations for a subset of the CAIs for which isotopic data are presented here were reported previously (Torrano et al., 2019). Those data along with the REE concentrations for the CAIs reported here for the first time are listed in Table 3.3 and illustrated in Fig. 3.2. Unfractionated group I REE patterns, interpreted to represent condensation from a gas of solar composition, are observed in five CAIs (Martin and Mason, 1974; MacPherson, 2013). Highly fractionated group II REE patterns—those interpreted to represent a complex condensation history resulting from fractional condensation where a refractory hibonite component was removed, followed by the condensation of the remaining REEs, are observed in six CAIs (Boynton, 1975; Mason and Martin, 1977; Davis and Grossman, 1979; MacPherson and Davis, 1994). A slightly fractionated group III REE pattern, interpreted to be associated with multiple heating/cooling events under changing redox conditions, is observed in one CAI (Ruzicka et al., 2012). In the sample set studied here, all fine-grained CAIs exhibit fractionated

REE patterns while coarse-grained CAIs (with some exceptions) generally exhibit unfractionated REE patterns.

Table 3.3. REE concentrations in the CAIs studied here, normalized to the CI chondrite values of Lodders (2003) (uncertainty is ± 5%, 2SD).

Sample	La	Ce	Pr	Nd	Sm	Eu	Gd	Tb	Dy	Ho	Er	Tm	Yb	Lu
ZT1[1]	20.5	20.0	18.5	20.2	21.0	20.6	19.1	20.9	22.7	26.8	30.1	23.0	22.7	29.4
ZT2[1]	19.1	20.5	20.2	22.5	23.7	13.7	9.7	8.9	6.8	3.3	2.6	20.7	12.0	2.5
ZT3[1]	5.8	18.1	11.0	9.2	15.7	6.4	1.7	1.6	1.3	0.4	0.3	17.1	5.0	0.3
ZT5[1]	19.9	53.1	20.9	20.7	20.8	269.6	11.0	10.9	11.0	6.0	4.0	34.3	109.2	3.0
ZT6	11.1	12.0	11.4	12.5	14.6	14.6	14.7	15.0	15.7	17.7	20.3	14.9	15.7	16.8
ZT7[1]	15.4	14.8	15.3	17.0	18.4	23.2	15.9	16.4	17.2	16.5	17.0	18.3	14.8	16.5
ZT8[1]	19.0	19.4	17.9	20.0	20.1	13.4	18.1	19.1	20.6	19.3	21.0	19.7	14.2	19.8
ZT10	2.9	5.4	4.2	3.8	6.1	2.9	1.2	1.2	0.9	0.3	0.2	6.3	2.2	0.2
ZT13	22.8	22.6	21.6	23.3	25.4	23.1	24.8	25.1	26.2	25.8	27.0	25.6	26.6	26.4
ZT14	7.9	7.3	7.9	8.7	8.8	4.1	2.1	1.9	1.5	0.5	0.3	10.2	4.3	0.2
Saguaro	3.3	3.0	3.1	3.5	3.5	4.7	4.4	4.1	4.0	3.5	3.2	3.2	3.3	3.0

[1]Data from Torrano et al. (2019)

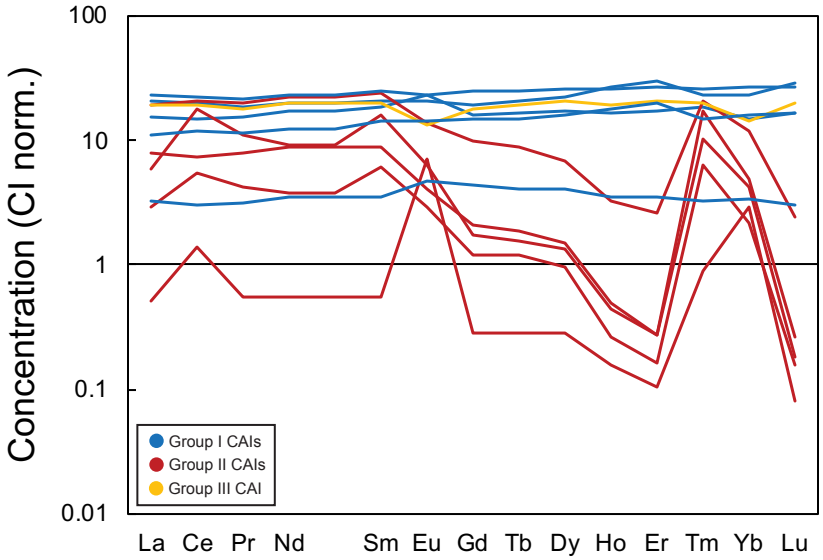

Fig. 3.2. REE abundances in the CAIs studied here normalized to REE abundances in CI chondrites (Lodders, 2003). Uncertainty is ± 5%, 2SD.

3.3.2 Cr and Ti Isotopic Compositions

The mass-independent Cr and Ti isotopic compositions of the CAIs studied here are shown in Table 3.4. Also shown in Table 3.4 are Cr and Ti isotopic compositions of the terrestrial rock standards AGV-1 and BCR-2 and the bulk Allende CV3 chondrite. We note that our data for the terrestrial rock standards BCR-2 and AGV-1 do not show

any Ti isotope anomalies within uncertainties. Furthermore, our data for the homogenized Allende bulk sample are consistent with previously reported values for both Cr and Ti isotopic compositions. These results demonstrate the accuracy of our chemical processing and mass spectrometry methods for Cr and Ti isotopic analyses. In the CAIs studied here, ε^{46}Ti values range from +0.89 (± 0.17) to +1.82 (± 0.17), ε^{48}Ti values range from +0.04 (± 0.07) to +0.55 (± 0.07), and ε^{50}Ti values range from +8.88 (± 0.17) to +10.68 (± 0.17). For Cr, ε^{53}Cr values range from –1.42 (± 0.12) to –0.31 (± 0.06) and ε^{54}Cr values range from +3.16 (± 0.13) to +7.28 (± 0.16). All ε^{53}Cr values have been corrected for the presence of radiogenic ^{53}Cr from the decay of ^{53}Mn by subtracting an estimated radiogenic ^{53}Cr component using the initial Solar System ^{53}Mn/^{55}Mn ratio of $6.28 \pm 0.66 \times 10^{-6}$ (Trinquier et al., 2008) and the ^{55}Mn/^{52}Cr ratios measured in these samples, and the uncertainty associated with this correction calculation has been incorporated into the reported uncertainty.

Table 3.4. Chromium and Ti isotopic compositions of the CAIs studied here, as well as bulk Allende CV3 chondrite and the BCR-2 and AGV-1 terrestrial rock standards. The reported error is either the internal error (2SE) based on the number of runs (n) of each sample or the external reproducibility (2SD), whichever is larger. The uncertainty associated with the radiogenic correction calculation has been incorporated into the reported error for ε^{53}Cr. For repeated standards, each line represents an aliquot processed separately.

Sample	ε^{46}Ti	ε^{48}Ti	ε^{50}Ti	n (Ti)	ε^{53}Cr	ε^{54}Cr	n (Cr)
ZT1[1]	1.21 ± 0.35	0.36 ± 0.07	9.50 ± 0.17	2	–1.42 ± 0.12	6.05 ± 0.13	6
ZT2[1]	1.63 ± 0.17	0.46 ± 0.09	9.07 ± 0.17	3	–1.17 ± 0.07	6.99 ± 0.16	3
ZT3[1]	1.69 ± 0.17	0.38 ± 0.07	10.68 ± 0.17	3	–0.61 ± 0.06	3.16 ± 0.13	7
ZT5[1]	1.40 ± 0.39	0.34 ± 0.07	9.04 ± 0.17	2	–0.64 ± 0.06	5.32 ± 0.15	3
ZT6	1.51 ± 0.17	0.55 ± 0.07	8.95 ± 0.20	4	–1.00 ± 1.46	5.37 ± 0.16	5
ZT7[1]	1.53 ± 0.17	0.40 ± 0.07	8.88 ± 0.17	3	–0.31 ± 0.06	3.41 ± 0.29	1
ZT8[1]	1.56 ± 0.17	0.43 ± 0.07	9.18 ± 0.17	3	–1.25 ± 0.06	7.28 ± 0.16	3
ZT10	0.89 ± 0.17	0.04 ± 0.07	10.45 ± 0.17	4	–0.62 ± 0.12	3.50 ± 0.13	5
ZT13	1.63 ± 0.26	0.41 ± 0.07	9.87 ± 0.27	5	–0.87 ± 1.84	5.66 ± 0.25	3
ZT14	1.74 ± 0.28	0.30 ± 0.07	9.16 ± 0.19	4	–0.61 ± 0.06	4.90 ± 0.13	5
Saguaro	1.82 ± 0.17	0.47 ± 0.10	9.38 ± 0.35	4	–1.03 ± 0.19	6.15 ± 0.31	4
AGV-1[1]	–0.14 ± 0.23	0.00 ± 0.07	0.08 ± 0.21	5			
AGV-1[1]	–0.07 ± 0.21	0.08 ± 0.09	–0.04 ± 0.17	5			
BCR-2[1]	–0.01 ± 0.17	–0.02 ± 0.08	–0.04 ± 0.17	8			
BCR-2[1]	–0.10 ± 0.17	0.01 ± 0.07	–0.09 ± 0.17	20			
BCR-2	–0.02 ± 0.34	0.09 ± 0.11	–0.15 ± 0.22	4			
Allende[1]	0.47 ± 0.34	–0.08 ± 0.23	3.08 ± 0.17	3			
Allende[1]	0.60 ± 0.17	0.00 ± 0.07	3.30 ± 0.17	32			
Allende	0.46 ± 0.17	0.01 ± 0.07	3.04 ± 0.21	4			
Allende					0.07 ± 0.06	0.81 ± 0.13	10
Allende					0.03 ± 0.06	0.88 ± 0.13	6

[1]Ti isotopic data from Torrano et al. (2019).

3.4. Discussion

3.4.1 The potential isotopic effect of matrix addition to CAIs

The significantly higher elemental abundance of Cr in carbonaceous chondrite matrix compared to CAIs combined with the low ε^{54}Cr values of the matrix means that a small addition of matrix material to a CAI, either because of parent body alteration, terrestrial alteration, or contamination during sample extraction, could have a substantial effect on the measured Cr isotopic composition. By using CI chondrites as a proxy for CAI-free carbonaceous chondrite matrix, we use a two-component mixing model in Fig. 3.3 to show that if the maximum ε^{54}Cr value measured in these CAIs is assumed to be the true matrix-free CAI value, the entire spread in ε^{54}Cr values for the CAIs measured here

could be accounted for by 0–30% addition of matrix material to the CAIs. The matrix endmember of mixing line A (+ symbols in Fig. 3.3) is defined by the elemental abundances (Cr = 2620 ppm, Ti = 458 ppm) and isotopic compositions (ε^{54}Cr = 1.58 ± 0.16, ε^{50}Ti = 1.85 ± 0.15) previously reported for CI chondrites (Shukolyukov and Lugmair, 2006; Trinquier et al., 2007, 2009; Qin et al., 2010; Zhang et al., 2012; Palme et al., 2014). The CAI endmember of the mixing line is defined by the mean elemental abundances (Cr = 418 ppm, Ti = 4218 ppm) in the CAIs studied here and in Torrano et al. (2019), the median value of ε^{50}Ti = 9 for CAIs studied here and in the literature, and the maximum value of ε^{54}Cr = 7.28 ± 0.16 for CAIs studied here. Because of the isotopic variability also observed in ε^{50}Ti, we have also plotted mixing line B (x symbols in Fig. 3.3). Mixing line B is defined by the same endmembers as mixing line A except for the ε^{50}Ti value for the CAI endmember, which is changed to the maximum value of ε^{50}Ti = 10.68 ± 0.17 for the CAIs studied here to illustrate that the CAIs with higher ε^{50}Ti values could also fall along such a mixing line. As illustrated in Fig. 3.3, minor amounts of matrix addition are unlikely to have any effect on the measured Ti isotopic compositions CAIs because of the much higher Ti elemental abundance in CAIs compared to carbonaceous chondrite matrix and thus cannot explain the observed Ti isotopic variability.

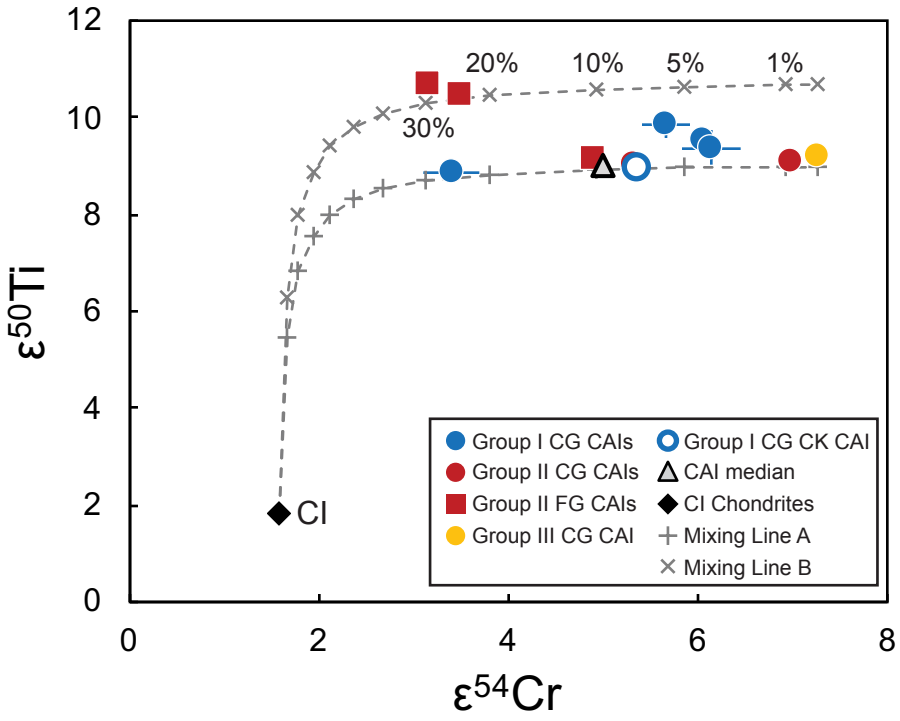

Fig. 3.3. ε^{50}Ti vs. ε^{54}Cr for the CAIs studied here, the median CAI isotopic composition, and the mean CI chondrite value along with mixing lines A and B (Heydegger et al., 1979; Niederer et al., 1980, 1981, 1985; Niemeyer and Lugmair, 1981, 1984; Birck and Allègre, 1984, 1985; Papanastassiou, 1986; Birck and Lugmair, 1988; Loss et al., 1994; Shukolyukov and Lugmair, 2006; Trinquier et al., 2007, 2009; Chen et al., 2009; Leya et al., 2009; Trinquier et al., 2009; Qin et al., 2010; Zhang et al., 2012; Palme et al., 2014; Williams et al., 2016; Simon et al., 2017; Davis et al., 2018; Ebert et al., 2018; Render et al., 2019; Torrano et al., 2019). Mixing lines are annotated with percentages showing percent matrix addition to a pure CAI composition.

Although Fig. 3.3 demonstrates that that the addition of ~0–30% matrix material to CAIs could account for the spread in ε^{54}Cr values measured here, additional data must be evaluated in order to determine whether matrix addition is in fact responsible. If matrix addition is the cause of the spread in ε^{54}Cr values, one would expect to see a correlation between the elemental concentration of Cr in the samples and the ε^{54}Cr values. A plot of ε^{54}Cr vs. ppm Cr for the CAIs measured here (Fig. 3.4) demonstrates that such a correlation does not exist. Although the lowest ε^{54}Cr value is measured in a

fine-grained CAI with a very high Cr concentration (ZT3), similarly low ε^{54}Cr values are also reported for CAIs with low Cr concentrations. This suggests that while matrix addition may at least partially account for the low ε^{54}Cr composition of ZT3, it cannot account for the full range of ε^{54}Cr values measured in the CAIs in this sample set. It is also important to note that previously published ε^{54}Cr values for CAIs span a range from ~0–8, including a handful of samples with ε^{54}Cr values below the ε^{54}Cr value of CI chondrites. Such values cannot be accounted for by matrix addition alone and therefore indicate that the variability in ε^{54}Cr observed in CAIs is inherent to the CAIs themselves.

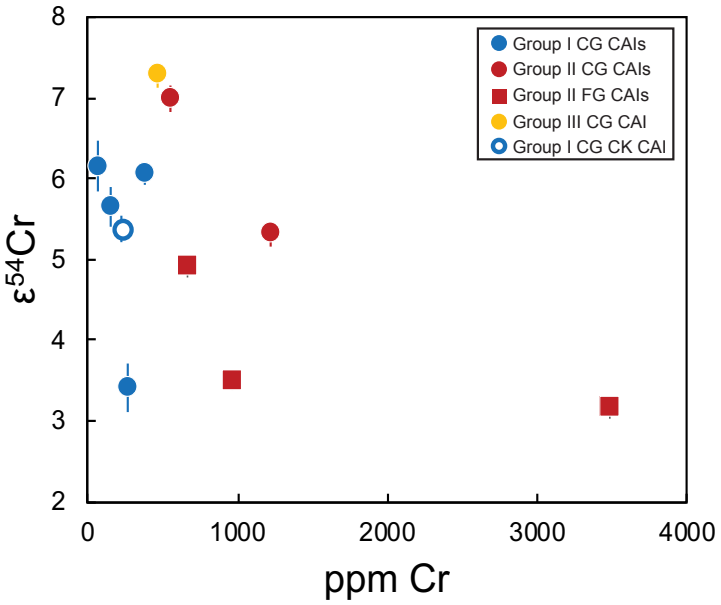

Fig. 3.4. ε^{54}Cr vs. ppm Cr for the CAIs studied here, showing no correlation. In general, the highest Cr concentrations are measured in the fine-grained CAIs (squares) and those with Group II REE patterns (red symbols), suggesting that fine-grained CAIs are more susceptible to matrix addition and/or that matrix addition may be more difficult to identify in these samples via optical microscope and electron microprobe analyses due to their fine-grained mineralogy.

3.4.2 The relationship between REE patterns and isotopic anomalies

Fractionated REE patterns in CAIs are considered to originate because of differences in thermal conditions and processing in the CAI-forming region of the nebula. If these conditions were responsible for selective destruction of isotopically distinct presolar phases (as suggested by Trinquier et al., 2009), one would expect to observe a correlation between the degree of fractionation in the REEs and the isotopic anomalies in CAIs. To assess whether such a correlation exists, in Fig. 3.5 we plot both ε^{50}Ti and ε^{54}Cr versus chondrite-normalized La/Lu ratios (i.e., $[La/Lu]_{CI}$) for CAIs in this study. While the highest ε^{50}Ti values are reported in fine-grained CAIs with fractionated REE patterns (i.e., $[La/Lu]_{CI} >> 1$), these CAIs do not have the highest ε^{54}Cr values. In neither case is there a clear correlation between isotopic compositions and the degree of fractionation of the REE patterns in CAIs. This lack of correlation suggests that the processes leading to the isotopic anomalies observed in CAIs were likely distinct from the conditions responsible for the observed REE patterns.

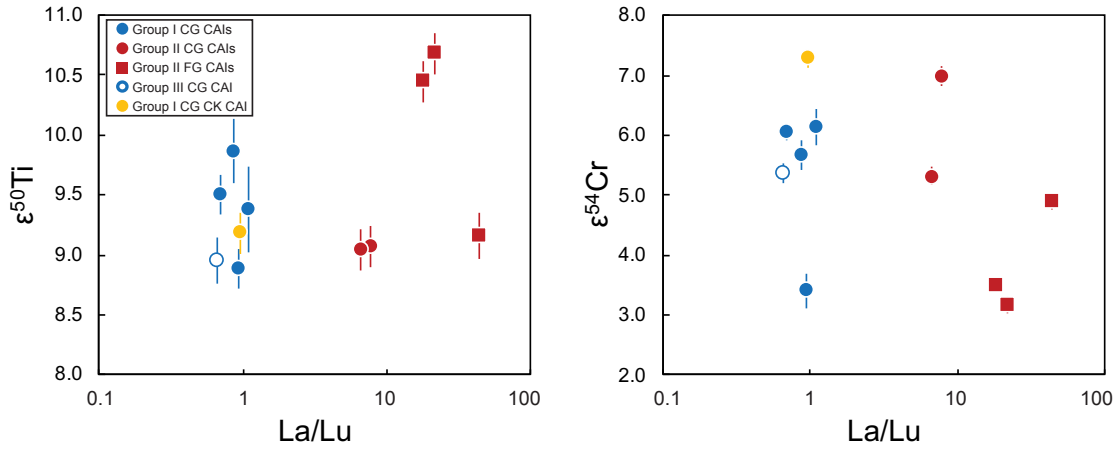

Fig. 3.5. The ε^{50}Ti (left) and ε^{54}Cr (right) values for the CAIs analyzed here plotted versus their chondrite-normalized La/Lu ratios (i.e., [La/Lu]/CI) (Lodders, 2003).

3.4.3 Clues to the origin of the NC–CC isotopic dichotomy

Following the discovery of the isotopic dichotomy between the NC and CC reservoirs in multiple isotope systems (e.g., Warren, 2011; Budde et al., 2016), it became necessary to ascertain whether these distinct isotopic reservoirs originated because of processes occurring within the protoplanetary disk or because of heterogeneity in the material inherited by the disk from the parent molecular cloud. The CC isotopic reservoir is enriched relative to the NC isotopic reservoir in supernova-derived neutron-rich isotopes including ^{50}Ti and ^{54}Cr in the direction of the isotopic composition of CAIs (Fig. 3.6). Because most CC materials contain CAIs and most NC materials do not, this appears to suggest that the addition of CAIs to the CC region could account for the observed dichotomy. However, the isotopic dichotomy is observed in both refractory elements such as Ti and Mo (which are abundant in CAIs) and non-refractory elements such as Cr and Ni (which are far less abundant in CAIs). The addition of CAI material to material of NC composition would therefore not have a significant effect on the isotopic composition of non-refractory elements on the scale of a region of the disk. This is reflected by the ε^{50}Ti vs. ε^{54}Cr mixing lines between NC meteorites and CAIs, which are hyperbolas that circumvent the CC region (black and gray dashed lines in Fig. 3.6, representing mixing of CAIs with ordinary chondrites and enstatite chondrites, respectively). Furthermore, even the refractory elements such as Ti that are abundant in CAIs cannot entirely account for the different between the NC and CC regions, as CAI-free CI chondrites have elevated ε^{50}Ti values compared to NC materials (Burkhardt et al., 2019). The presence of the isotopic dichotomy in neutron-rich isotopes of different volatilities also suggests that thermal processing and selective destruction of isotopically

anomalous presolar carriers (e.g., Trinquier et al., 2009) cannot be solely responsible for the observed isotopic dichotomy because these processes would be unlikely to preferentially affect only the carriers of supernova-derived neutron-rich isotopes. For these reasons, the isotopic dichotomy likely reflects the composition of material inherited from the molecular cloud and is less affected by processes occurring within the disk such as CAI transport and thermal processing.

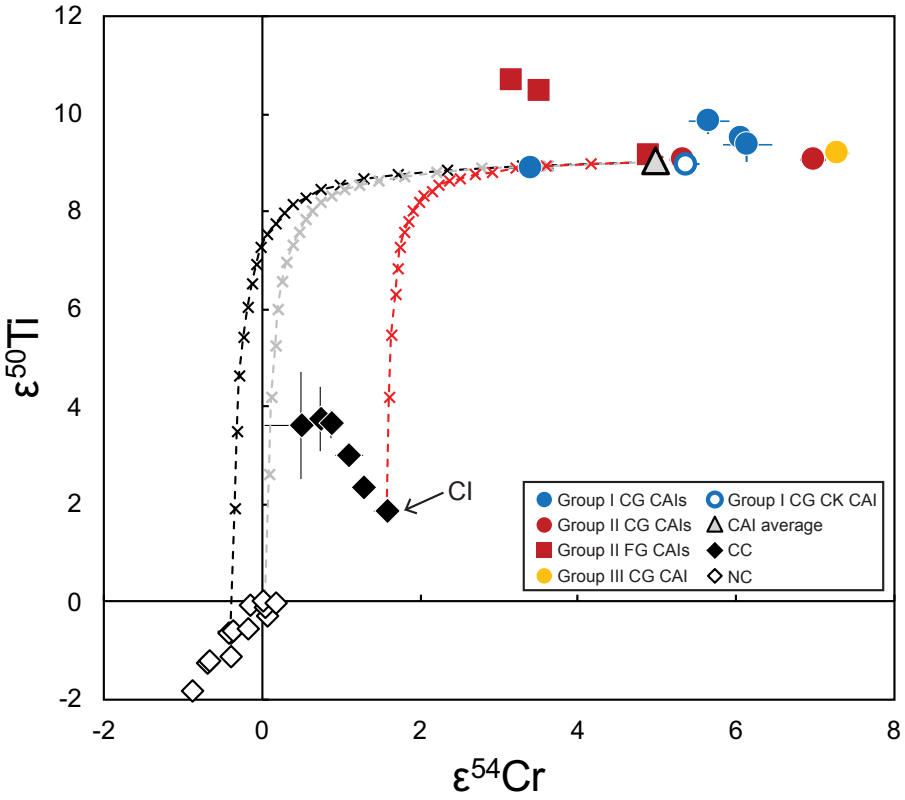

Fig. 3.6. ε^{50}Ti vs. ε^{54}Cr for bulk NC materials, CC materials, and CAIs studied here. The median isotopic composition of CAIs from this study and the literature is represented by the gray triangle (Heydegger et al., 1979; Niederer et al., 1980, 1981, 1985; Niemeyer and Lugmair, 1981, 1984; Birck and Allègre, 1984, 1985; Papanastassiou, 1986; Birck and Lugmair, 1988; Loss et al., 1994; Chen et al., 2009; Leya et al., 2009; Trinquier et al., 2009; Williams et al., 2016; Simon et al., 2017; Davis et al., 2018; Ebert et al., 2018; Render et al., 2019; Torrano et al., 2019). Isotopic data for NC and CC bulk meteorites are from the literature (Shukolyukov and Lugmair, 2006; Trinquier et al., 2007, 2009; Qin et al., 2010; Yamakawa et al., 2010; Zhang et al., 2011, 2012; Göpel et al., 2015). Mixing lines are shown between the median CAI value and ordinary chondrites (black dashed line), enstatite chondrites (gray dashed line), and CI chondrites (red dashed line).

For the mixing line calculation, elemental concentrations in bulk meteorites are from the compilation of Alexander et al. (2019) and references therein and the elemental concentrations for CAIs are the mean concentrations of the CAIs studied here and in Torrano et al. (2019). Each marker along the mixing lines represents a 5% increment of mixing.

Although the outward transport of CAIs and thermal processing occurring within the disk cannot entirely account for the isotopic dichotomy between the NC and CC regions, these processes may contribute to the orthogonal relationship between the slopes of the NC and CC isotopic regions in ε^{50}Ti vs. ε^{54}Cr space (Fig. 3.6). In ε^{50}Ti vs. ε^{54}Cr space, the NC materials define a positive correlation line, and the CAI-free CI chondrites, although part of the CC region, fall on an extension of this positive NC trend. The other carbonaceous chondrites, which all contain varying amounts of CAIs, plot above this line and define an inverse correlation between ε^{50}Ti and ε^{54}Cr that is orthogonal to the trend of NC meteorites (Fig. 3.6).

If the presence of CAIs was entirely responsible for the spread in both the Cr and Ti isotopic composition of CC meteorites, all CC meteorites should fall vertically along the mixing line between CAI-free CI chondrites and CAIs (red dashed line in Fig. 3.6) and both Cr and Ti isotopic compositions should be correlated with CAI abundance. Instead, CC meteorites fall along a trend that does not follow the CI–CAI mixing line, and the CI-normalized Al/Si ratios (which are proxies for CAI abundance) of CC meteorites are positively correlated with ε^{50}Ti but inversely correlated with ε^{54}Cr (Fig. 3.7). This suggests that while CAIs may exert the primary control on the ε^{50}Ti compositions of carbonaceous chondrites, they cannot explain the ε^{54}Cr compositions and other processes must therefore be responsible. One clue to the nature of the processes

controlling the ε^{54}Cr compositions of carbonaceous chondrites is the correlation between the ε^{54}Cr values and the degree of depletion in moderately volatile elements (Fig. 3.8). The thermal processing responsible for the chemical fractionation of moderately volatile elements may therefore be responsible for the spread in ε^{54}Cr compositions (Trinquier et al., 2009). If such thermal processing is responsible, it appears to have preferentially affected the isotopic composition of the non-refractory Cr (T_C = 1296) and not the refractory Ti (T_C = 1582) (Lodders, 2003).

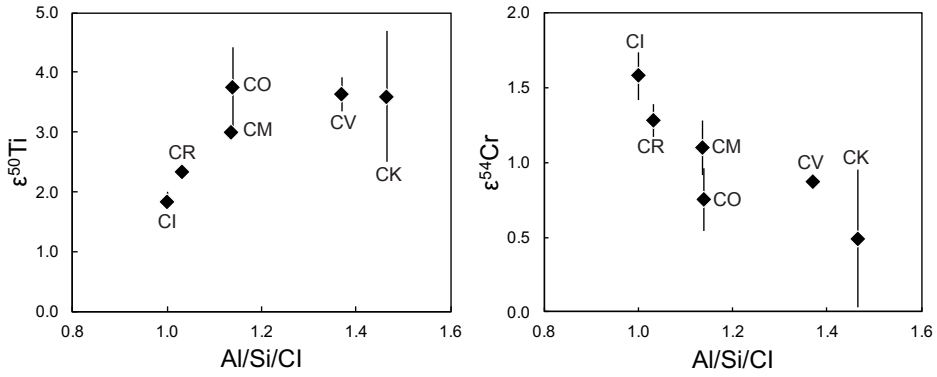

Fig. 3.7. The ε^{50}Ti (left) and ε^{54}Cr (right) anomalies vs. the Si- and CI-normalized Al abundances (a proxy for CAI abundance) in bulk carbonaceous chondrites. The ε^{50}Ti values are positively correlated with Al, while the ε^{54}Cr values are inversely correlated with Al. Figure adapted from Alexander et al. (2019) with isotopic data from Shukolyukov and Lugmair (2006), Trinquier et al., (2007, 2009), Qin et al. (2010), Yamakawa et al. (2010), Zhang et al. (2011, 2012), and Göpel et al. (2015), and elemental abundance data from the compilation of Alexander et al. (2019) and references therein.

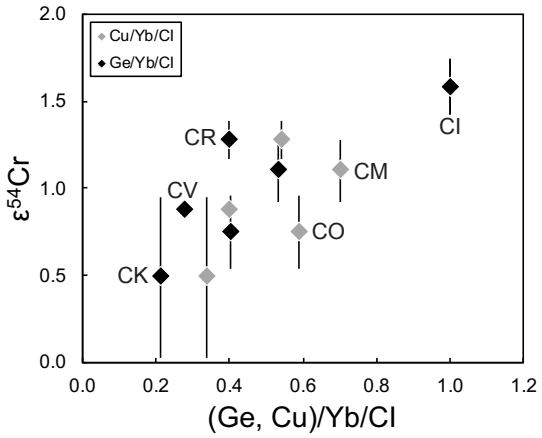

Fig. 3.8. ε^{54}Cr vs. Ge and Cu concentrations normalized to Yb and CI chondrites. Figure adapted from Trinquier et al. (2009) with concentration data from the compilation of Alexander et al. (2019) and isotopic data from Shukolyukov and Lugmair (2006), Trinquier et al., (2007), Qin et al. (2010), and Göpel et al. (2015).

The formation of the isotopic dichotomy as a result of the changing composition of material inherited from the molecular cloud rather than processes occurring within the disk is consistent with the model of Nanne et al. (2019) and Burkhardt et al. (2019), in which isotopically distinct stages of infalling material from the parent molecular cloud account for both the NC–CC isotopic dichotomy and the isotopic composition of CAIs. In this model, CAIs formed during an early infall stage of material enriched in the supernova-derived neutron-rich isotopes of elements such as Cr, Ni, Ti, and Mo, and recorded the isotopic composition of this material before being transported outwards via radial expansion. This also explains the similar oxygen isotopic composition of the Sun and CAIs if both formed primarily from the same early infalling material (McKeegan et al., 2011; Kööp et al., 2020). The later infalling material, depleted in supernova-derived neutron-rich isotopes and possessing an NC-like composition, then provided the majority of the mass of the inner disk.

After infall stopped, mass continued to be accreted by the proto-Sun because of inward transport of material (e.g., Yang and Ciesla, 2012). This inward transport would then cause some mixing to occur between the enriched early infalling material and the depleted inner disk, resulting in some dilution of its isotopic composition from that of CAIs. In order to prevent complete homogenization of the CC and NC isotopic reservoirs, this inward transport of material from the CC reservoir to the NC reservoir must have been obstructed prior to planetesimal formation in the CC reservoir (~1 Ma after CAI formation). This is achieved by the model of Kruijer et al. (2017), in which Jupiter's core grew to a size of ~20 Earth masses within 1 Ma of CAI formation and kept the NC and CC reservoirs separated for at least ~3–4 Ma. The resulting final CC reservoir isotopic composition is therefore intermediate between that of the earliest infalling material (the isotopic composition recorded by CAIs) and later infalling material (the isotopic composition recorded by the NC reservoir). The combined Nanne et al. (2019), Burkhardt et al. (2019), and Kruijer et al. (2017) models therefore explain (a) the observed isotopic dichotomy between the CC and NC regions and (b) the isotopic composition of CAIs.

In the context of these models for the formation of the NC–CC isotopic dichotomy, CAIs could provide insights into which stage(s) of star formation the Sun was experiencing during the period of CAI formation. It is thought that CAIs formed during the earliest stages of protoplanetary disk evolution, when our Sun was a class 0 (Wood, 2004; Connelly et al., 2012) or transitioning from a class I to II (Ciesla et al., 2010; Dauphas et al., 2011; Yang and Ciesla, 2012; Brennecka et al., 2020) young stellar object (YSO). The combined lifetime of class 0 and I YSOs is ~0.5 Ma (Evans et al., 2009), and

the combined lifetime of class 0, I, and II YSOs is ~1 Ma (Ciesla, 2010; Dauphas et al., 2011). These timescales are longer than the relative time difference of <0.2 Ma recorded by normal CAIs (Jacobsen et al., 2008; MacPherson et al., 2012; Kawasaki et al. 2019; Liu et al., 2019). The time period of CAI formation may have extended up to ~1 Ma but those CAIs formed during the first ~0.1 Ma of CAI formation—before the disk was drained of its mass and when outward radial transport was most efficient—are likely to be preferentially preserved in meteorites (Ciesla, 2010). As radial transport was most efficient around the time when infall stopped, the formation of CAIs preserved in meteorites likely corresponds to the transition between class I and class II YSOs (Yang and Ciesla, 2012) when the protoplanetary disk reached its maximum size and first reached temperatures of ~1,300 to 1,500 K (Whitney et al., 2003; Dauphas et al., 2011). It is possible that the rare FUN CAIs, which possess large nucleosynthetic isotopic anomalies and are depleted in ^{26}Al, may record a slightly earlier stage of infalling material that was more isotopically heterogeneous. Ensuing transport to the outer disk could then allow these solids to escape the conditions responsible for producing subsequently formed CAIs (Kita et al., 2013).

If the CAIs found in meteorites formed during a <0.2 Ma time period during the transition between class I and class II YSOs, then their isotopic compositions reflect that of the infalling material at this time. While the models of Nanne et al. (2019) and Burkhardt et al. (2019) require a broadly heterogeneous molecular cloud to account for the changing isotopic composition from the early infalling material to the late infalling material, the isotopic compositions of CAIs record smaller scale isotopic variability within the infalling material over a relatively short time period. This isotopic variability

could record either a) temporal changes in the isotopic composition of the infalling material during the <0.2 Ma time period of CAI formation, or b) spatial isotopic variability in the infalling material. Both of these scenarios may record inputs from other stellar sources such as supernovae. Nanne et al. (2019) discuss the temptation to link the early infalling material enriched in nuclides derived from supernovae to the proposed supernova trigger for the formation of the Solar System (Cameron and Truran, 1977) but point out that because the enriched supernova-derived nuclides do not provide any temporal constraints, the isotopic composition of the infalling material cannot be linked to a specific event. These isotopic data nevertheless provide important constraints on the isotopic composition of the infalling material inherited by our protoplanetary disk from the parent molecular cloud and suggest that the isotopic variability recorded by materials in our Solar System was inherited from this infalling material.

3.4.4 Identifying the sources contributing to the infalling material

Previously reported mass-independent Ti isotopic compositions of CAIs display a correlation between ε^{46}Ti and ε^{50}Ti with a slope of 5.98 ± 0.29 and an intercept of –0.61 ± 0.46 (black line in Fig. 3.9; Leya et al., 2009; Trinquier et al., 2009; Davis et al., 2018; Render et al., 2019; Torrano et al., 2019) and bulk samples of carbonaceous meteorites, non-carbonaceous meteorites, Earth, Moon, and Mars (e.g., Trinquier et al., 2009; Zhang et al., 2011, 2012) display a similar correlation with a slope of 5.38 ± 0.19 and an intercept of –0.12 ± 0.07. The CAIs measured here generally fall along the same correlation line, although some scatter about the line is observed (Fig. 3.9). This correlation is significant because the isotopes ^{46}Ti and ^{50}Ti are produced by distinct

nucleosynthetic sources: ^{46}Ti is produced during explosive oxygen- and silicon-burning at the top of the Si/S zone in Type II supernovae (SNII), whereas ^{50}Ti may be produced in multiple sources, including Type Ia supernovae (SNIa), the O/Ne and O/C zones of SNII (while it is destroyed in the explosive burning zones where other Ti isotopes are produced), and electron-capture supernovae (ECSN) (Wanajo et al., 2013; Davis et al., 2018). The correlation line likely represents the mixing between a ^{46}Ti- and ^{50}Ti-poor reservoir and a ^{46}Ti and ^{50}Ti-rich reservoir, and because of the distinct nucleosynthetic sources of these two isotopes, the reservoir enriched in both must have itself resulted from the mixing and processing of materials from two distinct reservoirs (one enriched in ^{46}Ti and the other enriched in ^{50}Ti). Therefore, these data suggest that material from at least three distinct isotopic reservoirs—likely different supernova sources or different zones of a single supernova—was present in the infalling material inherited from the molecular cloud.

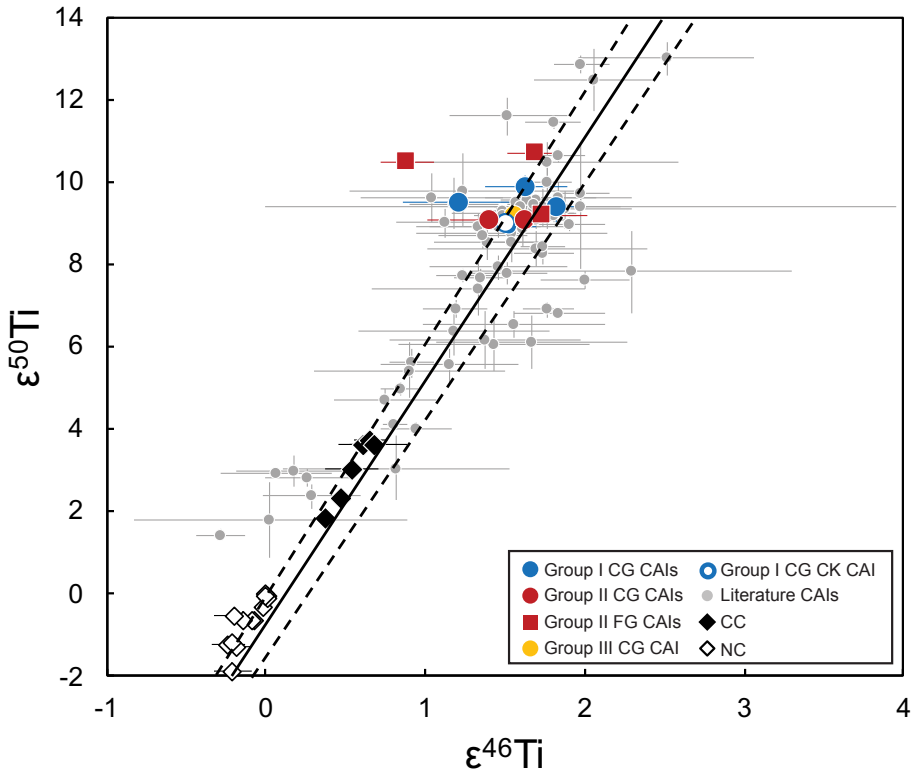

Fig. 3.9. (Left) A plot of ε^{46}Ti vs. ε^{50}Ti for the CAIs analyzed here (colored symbols), CAIs from the literature (gray circles; Leya et al., 2009; Trinquier et al., 2009; Davis et al., 2018; Ebert et al., 2018; Render et al., 2019; Torrano et al., 2019), and bulk samples of a variety of Solar System materials (white diamonds are carbonaceous meteorites and black diamonds are non-carbonaceous meteorites, Earth, Moon, and Mars; Trinquier et al., 2009; Zhang et al., 2011, 2012). The solid black line and dashed error envelope lines represent a best-fit regression for all CAIs plotted here (including CAIs from this study and the literature).

In ε^{53}Cr vs. ε^{54}Cr space, NC materials exhibit a negative trend while CC materials exhibit a positive trend (Fig. 3.10). These two isotopes are produced by different nucleosynthetic processes: ^{53}Cr is produced primarily during explosive silicon-burning in SNII and the majority of ^{54}Cr is produced in SNIa with some produced in SNII (Clayton, 2003; Dauphas et al., 2010). An additional cosmic source of ^{53}Cr is the decay of the short-lived isotope ^{53}Mn ($t_{1/2}$ = 3.74 Ma). The CAIs studied here appear to exhibit an inverse correlation, but it is unclear whether such an inverse correlation exists in all CAIs. This could be investigated by further high-precision analyses and may provide

important insights into the isotopic reservoirs that contributed material to our protoplanetary disk.

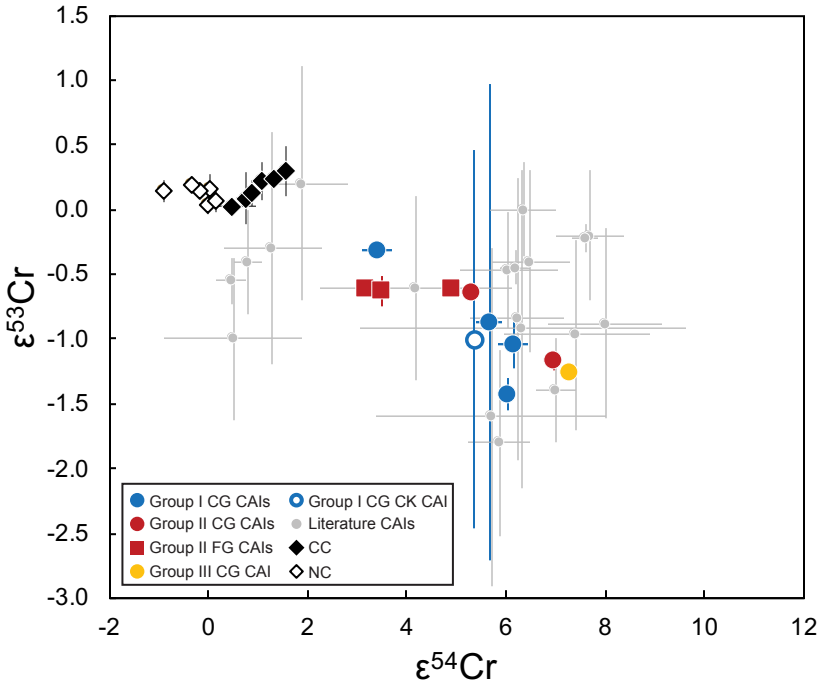

Fig. 3.10. ε^{53}Cr (corrected for radiogenic input) vs. ε^{54}Cr for the CAIs analyzed here (colored symbols), CAIs from the literature (gray circles; Birck and Allègre, 1984, 1985; Papanastassiou, 1986; Birck and Lugmair, 1988; Loss et al., 1994), and bulk samples of a variety of Solar System materials (white diamonds are carbonaceous meteorites and black diamonds are non-carbonaceous meteorites, Earth, Moon, and Mars; Trinquier et al., 2009; Zhang et al., 2011, 2012).

3.4.5 Isotopic variability in CAIs: Inherited or produced by processing in the disk?

One goal of measuring the Cr and Ti isotopic compositions of CAIs is to determine whether all CAIs formed within a common isotopic reservoir and to characterize the isotopic variability of their formation reservoir(s). The CAIs studied here show resolvable variation in both ε^{50}Ti and ε^{54}Cr that falls within the range established by previous studies of CAIs from CV, CM, CO, and ordinary chondrites for Ti and CAIs from CV chondrites for Cr (Fig. 3.11). The median values of ε^{50}Ti and ε^{54}Cr for the CAIs

reported here are ~9 and ~5, respectively, which are similar to the median values of previously measured CAIs in the literature (Heydegger et al., 1979; Niederer et al., 1980, 1981, 1985; Niemeyer and Lugmair, 1981, 1984; Birck and Allègre, 1984, 1985; Papanastassiou, 1986; Birck and Lugmair, 1988; Loss et al., 1994; Chen et al., 2009; Leya et al., 2009; Trinquier et al., 2009; Williams et al., 2016; Simon et al., 2017; Davis et al., 2018; Ebert et al., 2018; Burkhardt et al., 2019; Render et al., 2019; Torrano et al., 2019). These data support the conclusions of previous studies that all CAIs formed in a common isotopic reservoir that preserved some isotopic variability (Ebert et al., 2018; Render et al., 2019; Torrano et al., 2019).

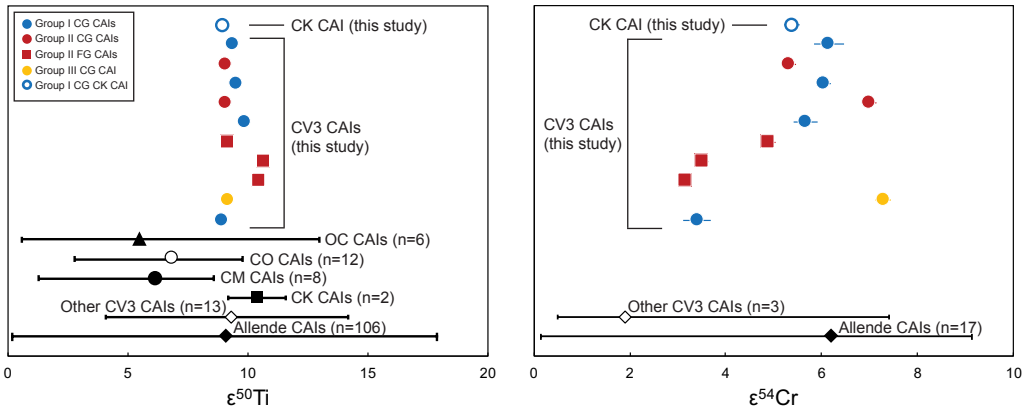

Fig. 3.11. The ε^{50}Ti and ε^{54}Cr values for the CAIs analyzed here (colored symbols) along with CAIs measured in previous studies. Literature data for CAIs from Allende (black diamond), other CV3 chondrites (white diamond), CK chondrites (black square), CM chondrites (black circle), CO chondrites (white circle), and ordinary chondrites (black triangle) from Heydegger et al., 1979, Niederer et al., 1980, 1981, 1985, Niemeyer and Lugmair, 1981, 1984, Birck and Allègre, 1984, 1985, Papanastassiou, 1986, Birck and Lugmair, 1988, Loss et al., 1994, Chen et al., 2009, Leya et al., 2009, Trinquier et al., 2009, Williams et al., 2016, Davis et al., 2018, Ebert et al., 2018, Render et al., 2019, Burkhardt et al., 2019, Torrano et al., 2019. For the literature data, symbols represent the median values and black bars represent the range of reported values.

While the CAIs studied here show resolvable variability in both ε^{54}Cr than ε^{50}Ti, a higher degree of variability is observed in ε^{54}Cr for the samples measured here (Fig. 3.11). As discussed in section 3.4.1, although the addition of matrix material to CAIs

could hypothetically account for at least some of the additional variability in ε^{54}Cr, this does not appear to be the case for the CAIs measured here. Instead, the observed variability is likely intrinsic to the CAIs. Another potential source of the additional ε^{54}Cr variability is aqueous alteration, but Sanborn et al. (2015) report no modification of ε^{54}Cr values in samples that have undergone extensive alteration. Furthermore, the CAIs studied here show few to no alteration phases. Therefore, the isotopic variability in both ε^{54}Cr and ε^{50}Ti likely reflect isotopic variability in the CAI-forming region inherited from infalling material, variable distribution of carrier phases, and/or thermal processing occurring within the disk.

If the isotopic heterogeneity of infalling material from the molecular cloud was solely responsible for the magnitude and variability of isotopic anomalies in CAIs, then ε^{50}Ti, ε^{54}Cr, and other isotopic anomalies such as Δ^{95}Mo should correlate in CAIs. However, no such correlation is observed (e.g., this study; Brennecka et al., 2020) and the isotopic variability in CAIs is therefore unlikely to be the result of heterogeneity in the infalling material alone. Trinquier et al. (2009) argued that thermal processing in the disk could cause preferential volatilization of less stable isotopically anomalous carriers that were initially homogeneously distributed and result in isotopic heterogeneity. However, it would be difficult for thermal processing to favor the same nucleosynthetic components for all elements despite their different carrier phases, which would be necessary to account for the isotopic variability measured in CAIs for both refractory and non-refractory elements unless each of these elements were present in similarly refractory phases (Nanne et al., 2019). It is also difficult to account for the associated evaporated matter in the protoplanetary disk resulting from such processes (Jacquet et al., 2019). Ti-

bearing refractory phases would be among the last to evaporate and first to recondense, limiting the efficiency of thermal processing for creating isotopic variability in Ti (Kööp et al., 2016b), and maintaining enough Ti in the vapor phase would require temperatures that would likely cause most other solids to also evaporate (Leya et al., 2009). For these reasons, it is also unlikely that thermal processing in the disk alone can account for the observed isotopic variability in CAIs.

Heterogeneous distribution of carrier phases of isotopic anomalies may contribute to the observed isotopic variability in CAIs. Sub-micron spinel grains that may have condensed in supernova outflows have been identified as likely carriers of Cr isotopic anomalies in multiple studies (Dauphas et al., 2010; Qin et al., 2011). Perovskite has been suggested as a candidate for the carrier of Ti isotopic anomalies because it is a highly refractory mineral present in most CAIs and contains Ca and Ti in the right proportion to explain the slope of the correlation between the isotopic anomalies measured for those elements (Dauphas et al., 2014). If such carrier phases were heterogeneously distributed in CAIs or CAI precursor material, or were variably affected by processing in the disk, this could account for some or all of the observed isotopic variability. Future investigations of carrier phases and the effects of disk processing on such phases are necessary to ascertain the relative contributions of heterogeneous carrier phase distribution, thermal processing, and inheritance during infall from the molecular cloud to the observed isotopic variability in CAIs.

3.5 Conclusions

In this study, we report the coupled mass-independent Cr and Ti isotopic compositions for 11 CAIs from 6 CV3 chondrites and one CK3 chondrite. The implications of this work are as follows:

1) There is no correlation between either the ε^{50}Ti or ε^{54}Cr isotopic compositions and chondrite-normalized La/Lu ratios in these CAIs, suggesting that the processes leading to the isotopic anomalies observed in CAIs were likely distinct from the conditions responsible for the observed REE patterns.
2) The offset of the CC isotopic reservoir from the NC isotopic reservoir towards the isotopic composition of CAIs in ε^{50}Ti vs. ε^{54}Cr space cannot be solely caused by the addition of CAIs to the CC region or the thermal processing of isotopically anomalous components within the disk. Instead, the observed ε^{50}Ti and ε^{54}Cr isotopic compositions of CAIs is consistent with previous models in which CAIs record the isotopic composition of early infalling material inherited by our protoplanetary disk from the parent molecular cloud and the composition of the CC region represents that of early infalling material that underwent some mixing with the later infalling material that makes up the NC region (e.g., Burkhardt et al., 2019; Nanne et al., 2019). The addition of CAIs to the CC region and thermal processing in the disk may, however, contribute to the range of ε^{50}Ti and ε^{54}Cr compositions observed in bulk carbonaceous chondrites.
3) A strong correlation exists between ε^{46}Ti and ε^{50}Ti for Solar System materials including CAIs and likely represents the mixing between a ^{46}Ti- and ^{50}Ti-poor

reservoir and a ^{46}Ti- and ^{50}Ti-rich reservoir. Because of the distinct nucleosynthetic sources of these isotopes, the reservoir enriched in both ^{46}Ti and ^{50}Ti must itself have resulted from the mixing of materials from two distinct reservoirs. Therefore, these data suggest that materials from at least three distinct nucleosynthetic sources are present in the CAI-forming region. While most CAIs studied here fall on this correlation line, some do not and may record an intermediate stage of mixing.

4) Resolvable variation in both the ε^{50}Ti and ε^{54}Cr isotopic compositions of CAIs is observed and likely results from a combination of thermal processing in the disk, isotopic heterogeneity inherited during infall from the parent molecular cloud, and carrier phase distribution. Median ε^{50}Ti and ε^{54}Cr values for these CAIs are similar to those reported previously in the literature for CAIs from CV, CK, CM, CO, and ordinary chondrites for ε^{50}Ti and for CAIs from CV chondrites for ε^{54}Cr, reaffirming that all CAIs formed in a single common isotopic reservoir with some preserved isotopic variability.

Acknowledgements: We thank Laurence Garvie for his assistance with the selection and acquisition of samples, and the Center for Meteorite Studies at ASU for providing samples. This work was supported by NASA grant NNX15AH41G to M. W.

CHAPTER 4

THE RELATIONSHIP BETWEEN CM AND CO CHONDRITES: INSIGHTS FROM CORRELATED CHROMIUM AND TITANIUM ISOTOPIC ANALYSES OF UNGROUPED CHONDRITES

4.1 Introduction

The isotopic compositions of meteorites provide forensic clues to the source region of their parent bodies and enable evaluation of potential genetic relationships between a given sample and known meteorite groups. Many previous studies have used oxygen isotope compositions of meteorites to identify common nebular source reservoirs and establish genetic relationships (e.g., Clayton and Mayeda, 1999). More recently, Cr and Ti isotopes have also been found to be useful isotopic tracers of distinct Solar System reservoirs (e.g., Warren, 2011; Sanborn et al., 2019). A fundamental dichotomy has been identified between "non-carbonaceous chondritic" (NC) and "carbonaceous chondritic" (CC) Solar System materials in a variety of isotope systems, including Cr, Ti, and O, and these isotopic reservoirs are considered to be represented by meteoritic materials of inner (NC) and outer (CC) Solar System provenance (Warren, 2011). These distinct isotopic reservoirs are thought to have coexisted from ~1 Ma to 3–4 Ma after Solar System formation, likely remaining separated because of the formation and growth of Jupiter (Kruijer et al., 2017). Therefore, the combined analysis of the isotopic compositions of multiple elements such as Cr and Ti in meteorites can serve as a powerful tracer for assessing potential genetic relationships between meteorite parent bodies.

The Mighei-like (CM) and Ornans-like (CO) carbonaceous chondrites are considered part of the CM–CO clan (Weisberg et al., 2006) on the basis of mineralogical and chemical similarities. The study of CM chondrites is especially timely because spectral properties and albedo measurements of CM chondrites are similar to those reported for the B-type asteroid Bennu and the C-type asteroid Ryugu by the OSIRIS-REx and Hayabusa2 missions, respectively (e.g., Hamilton et al., 2019; Kitazato et al., 2019; Lauretta et al., 2019). Similar formation conditions of CM and CO chondrite parent bodies have been suggested based on similarities in bulk elemental and O-isotope compositions (Kallemeyn and Wasson, 1981; Clayton and Mayeda, 1999; Weisberg et al., 2006; Greenwood et al., 2014) and chondrule and matrix olivine compositions (Frank et al., 2014; Schrader and Davidson, 2017). However, origin on distinct parent bodies for these two carbonaceous chondrite classes is suggested based on differences in bulk chondrule compositions (Rubin and Wasson, 1986), mean chondrule sizes (Schrader and Davidson, 2017), abundances of FeO-poor relict grains (Schrader and Davidson, 2017), mean matrix abundances (Weisberg et al., 2006), distinct cosmic-ray exposure ages (Eugster, 2003), Cr and Ti isotopes (e.g., Warren, 2011; Sanborn et al., 2019), and the absence of breccias containing both CM and CO chondrite materials. Quantitative modeling of meteorite parent body formation locations has further suggested that the CM and CO chondrite parent bodies accreted in nearby but distinct regions of the solar protoplanetary disk at different times (Sugiura and Fujiya, 2014; Desch et al., 2018).

A gap exists in three-oxygen isotope space between the compositions of CM and CO chondrites (Fig. 4.1), and this gap is populated by C2-ungrouped and anomalous CM chondrites that show affinities to both groups (e.g., Greenwood et al., 2019). These O-

isotope data suggest that either the CM and CO chondrites may share a single heterogeneous parent body or multiple CM and CO chondrite-related parent bodies may have formed in a common reservoir in the solar protoplanetary disk.

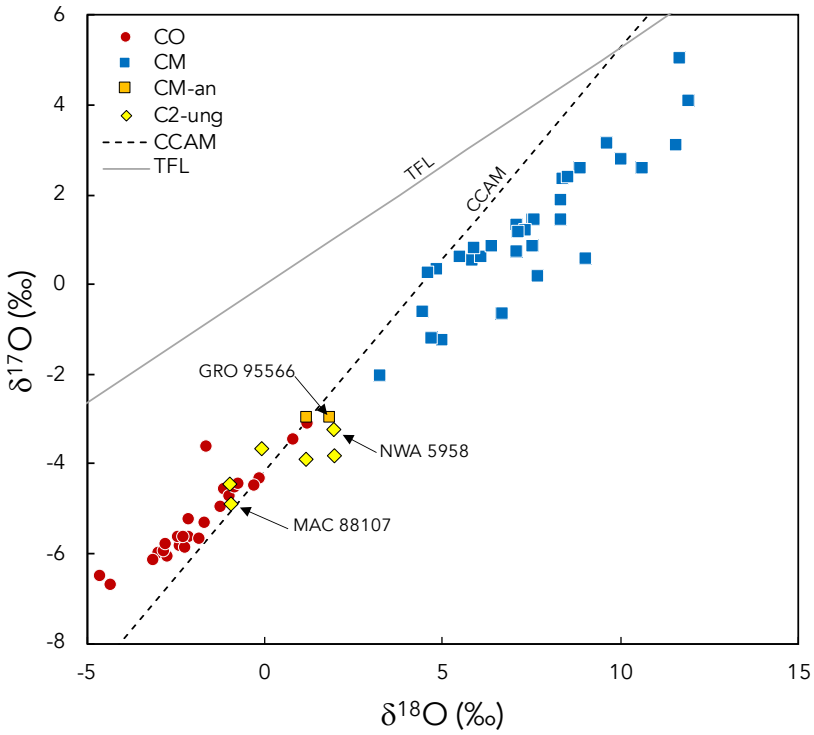

Fig. 4.1. Oxygen isotope compositions of CO, CM, CM-an, and C2-ungrouped chondrites (Clayton and Mayeda, 1999; Greenwood and Franchi, 2004; Haack et al., 2012; Hewins et al., 2014; Jacquet et al., 2016). Also plotted for reference are the terrestrial fractionation line (TFL; Clayton et al., 1973) and carbonaceous chondrite anhydrous mineral (CCAM) line (Clayton and Mayeda, 1977).

A difference in isotopic composition also exists between CM and CO chondrites in ε^{54}Cr vs. ε^{50}Ti space (e.g., Warren, 2011; Sanborn et al., 2019), but the ε^{54}Cr and ε^{50}Ti isotopic compositions of the ungrouped and anomalous chondrites that plot in the compositional gap between CM and CO chondrites in three-oxygen isotope space have not yet been determined. The primary focus of this study is to determine the Cr and Ti isotopic compositions of several CM and CO chondrites as well as of selected ungrouped chondrites documented to have similar mineralogic and/or geochemical characteristics

with the goal of providing better constraints on the relationship between CM and CO chondrites. The Cr and Ti isotopic compositional ranges of the CM and CO chondrite groups are not well constrained, and we have therefore measured the isotopic compositions of Isna (CO 3.8), Murchison (CM2), Murray (CM2), and Aguas Zarcas (CM2). Anomalous CM chondrite Grosvenor Mountains (GRO) 95566 was also measured. The ungrouped chondrites studied here with affinities to CM and CO chondrites include Elephant Moraine (EET) 83226, EET 83355, MacAlpine Hills (MAC) 87300, MAC 87301, MAC 88107, and Northwest Africa (NWA) 5958. We also measured the Cr and Ti isotopic compositions of several additional ungrouped chondrites with documented affinities to either the carbonaceous or ordinary chondrites, including LaPaz Ice Field (LAP) 04757, LAP 04773, Lewis Cliff (LEW) 85332, and Coolidge. In total, we report correlated Cr and Ti isotopic compositions for ten ungrouped chondrites, one anomalous CM chondrite, three CM chondrites, and one CO chondrite. Using these isotopic data, we assess potential genetic relationships between ungrouped chondrites and established chondrite groups, with a particular focus on evaluating the genetic relationship between CM and CO chondrites.

4.2 Samples and Methods

4.2.1 Sample Description

The samples studied here are listed in Table 4.1. Samples of nine meteorites were acquired from NASA's Antarctic Meteorite Collection. These samples, listed with their respective NASA split numbers following their sample names, are EET 83226,1, EET 83355,37, GRO 95566,34, LAP 04757,11, LAP 04773,7, LEW 85332,64, MAC

87300,77, MAC 87301,18, and MAC 88107,65. Samples of six meteorites were acquired from the Center for Meteorite Studies at Arizona State University (ASU). These samples, listed with their respective ASU sample numbers, are Aguas Zarcas ("A" from 2121_5 and "B" from 2121_6), Coolidge (397.2x), Isna (984,1), Murchison (828,27), Murray (635,2), and NWA 5958 (1743-3).

Table 4.1 List of the samples included in this study (uncertainty of elemental concentration values is ± 5%, 2SD).

Meteorite	Classification	Mass Powdered (mg)	Mass Dissolved (mg)	ppm Cr	ppm Ti
EET 83226	C2-ung	133.2	19.26	4103	875
EET 83355	C2-ung	228.3	32.25	4687	926
MAC 87300	C2-ung	137.0	32.59	4297	854
NWA 5958	C2-ung	523.2	35.45	6980	1393
LEW 85332	C3-ung	173.0	32.00	4493	726
MAC 88107	C3-ung	176.5	31.99	6586	1357
MAC 87301	C3-ung	198.5	44.20	2725	611
Coolidge	C4-ung	778.3	31.20	5500	1254
LAP 04757	Chondrite-ung	160.8	28.97	5067	834
LAP 04773	Chondrite-ung	214.2	27.20	3622	568
GRO 95566	CM-an	133.0	32.44	3381	682
Aguas Zarcas A[1]	CM2	82.6	64.35	5600	1096
Aguas Zarcas B[1]	CM2	137.3	56.48	3212	639
Murchison	CM2	356.9	45.90	5707	1176
Murray	CM2	333.9	49.30	3156	611
Isna	CO3.8	548.5	49.70	4372	872

[1]Aguas Zarcas A is the chondrule-poor lithology (~80 area%; Gattacceca, 2019) and Aguas Zarcas B is the chondrule-rich lithology (~20 area%; Gattacceca, 2019)

4.2.2 Analytical Methods

4.2.2.1 Sample Digestion and Concentration Measurements

Samples of Coolidge, EET 83226, EET 83355, GRO 95566, LAP 04757, LAP 04773, LEW 85332, MAC 87300, MAC 87301, MAC 88107, and NWA 5958 were crushed and powdered using a clean agate mortar and pestle in the Center for Meteorite Studies at ASU. Samples of Aguas Zarcas, Murchison, Murray, and Isna were crushed and powdered using a clean agate mortar and pestle in the Isotope Cosmochemistry and Geochronology Laboratory (ICGL) at ASU. All sample powders were treated with a 3:1

ratio of concentrated HF and HNO_3 on a hot plate, dried down, and then loaded into Parr bombs in a 2:1 ratio of concentrated HF and HNO_3. A ~5% aliquot of each sample solution was reserved for elemental concentration measurements using the Thermo Scientific iCAP-Q quadrupole inductively coupled plasma mass spectrometer in the W. M. Keck Foundation Laboratory for Environmental Biogeochemistry. Aliquots of the remaining ~95% of the sample solutions were then processed for Cr and Ti purification. Similar digestion procedures were used for the terrestrial rock standards BCR-2 and DTS-1 and a powdered and homogenized bulk sample of the Allende CV chondrite. Based on repeated analyses of standards, we estimate an uncertainty (2SD) of ±5% for elemental concentration measurements.

4.2.2.2 Chromium and Titanium Purification and Isotopic Analyses

Purification of Cr and Ti was conducted in the ICGL at ASU via column chromatography. The Cr purification chemistry followed the methods detailed in Chapter 3 of this dissertation, which were adapted from Yamakawa et al. (2009) and Larsen et al. (2016). Chromium yields for all samples and standards exceeded 95% with a procedural blank of less than 1 ng of Cr. The Ti purification chemistry followed the methods of Torrano et al. (2019), and Ti yields exceeded 95% for all samples and standards with a procedural blank of less than 5 ng of Ti.

Isotopic measurements of Cr and Ti were conducted on a Thermo Finnigan Neptune multi-collector inductively coupled plasma mass spectrometer (MC-ICPMS) at ASU using a jet sample cone and an H-skimmer cone in high-resolution mode (i.e., with a mass resolving power >8000). Samples were introduced through an Elemental

Scientific Apex-Q desolvating system attached to a self-aspirating PFA with an uptake rate of 100 μL/min for Cr, and through a Cetac Aridus II desolvating nebulizer attached to a self-aspirating PFA with an uptake rate of 100 μL/min for Ti. An uptake time of 90 s and a wash time between consecutive sample and standard measurements of 120 s were used. Each repeat of a sample, standard, or blank comprised 36 cycles for Cr and 50 cycles for Ti with an 8 s integration time per cycle.

Purified Cr samples and standards were analyzed at a concentration of 800 ppb with a typical sensitivity for ^{52}Cr of ~25V. The intensities of ^{50}Cr, ^{52}Cr, ^{53}Cr, and ^{54}Cr were measured, as were ^{49}Ti, ^{51}V, and ^{56}Fe to monitor and correct for isobaric interferences. Purified Ti samples and standards were analyzed at a concentration of 1 ppm with a typical sensitivity for ^{48}Ti of ~25V. Titanium isotope data were collected by switching between two different cup configurations. The intensities of ^{44}Ca, ^{46}Ti, ^{47}Ti, ^{48}Ti, and ^{49}Ti were measured in the first cup configuration, followed by measurement of ^{47}Ti, ^{49}Ti, ^{50}Ti, ^{51}V, and ^{52}Cr intensities with the second cup configuration, with the intensities of ^{44}Ca, ^{51}V, and ^{52}Cr used to correct for isobaric interferences on the Ti masses. All data reduction was performed offline.

The mass-independent Cr isotopic compositions are reported relative to the SRM 979 Cr standard after correction for instrumental and natural mass-dependent fractionation using sample-standard bracketing and internal normalization to ^{50}Cr/^{52}Cr applying an exponential mass fractionation law and a ^{50}Cr/^{52}Cr ratio of 0.051859 (Shields et al., 1966). The mass-independent Ti isotopic compositions are reported relative to the NIST 3162a Ti standard after correction for instrumental and natural mass-dependent fractionation using sample-standard bracketing and internal normalization to ^{49}Ti/^{47}Ti

applying an exponential mass fractionation law and a $^{49}Ti/^{47}Ti$ ratio of 0.749766 (Niederer et al., 1981). Isotopic compositions are reported in ε notation, i.e., parts per ten thousand deviation from the standard. Our external reproducibilities based on repeat measurements of standards in our laboratory are ± 0.13 (2SD) for $\varepsilon^{54}Cr$ and ± 0.13 (2SD) for $\varepsilon^{50}Ti$.

4.3. Results

4.3.1 Cr and Ti Isotopic Compositions

The mass-independent Cr and Ti isotopic compositions of the samples measured here are shown in Table 4.2 along with the isotopic compositions of the terrestrial rock standards BCR-2 and DTS-1 and the bulk homogenized Allende CV chondrite. Our data for the terrestrial standards do not show any isotopic anomalies within the uncertainties, and our data for the Allende bulk sample are consistent with previously reported values (e.g., Shukolyukov and Lugmair, 2006; Trinquier et al., 2007, 2008; Qin et al., 2010).

Table 4.2. The Cr and Ti isotopic compositions of the meteorites studied here, as well as bulk homogenized Allende CV chondrite and the BCR-2 and DTS-1 terrestrial rock standards. The reported error is either the internal error (2SE) based on the number of runs (n) of each sample or the external reproducibility (2SD), whichever is larger.

Meteorite	Classification	ε^{50}Ti	n	ε^{54}Cr	n
EET 83226	C2-ung	4.25 ± 0.13	6	0.93 ± 0.13	6
EET 83355	C2-ung	3.11 ± 0.13	3	0.76 ± 0.13	6
MAC 87300	C2-ung	4.67 ± 0.13	3	0.71 ± 0.14	6
NWA 5958	C2-ung	3.34 ± 0.13	5	1.18 ± 0.16	6
LEW 85332	C3-ung	2.42 ± 0.13	3	1.23 ± 0.13	6
MAC 88107	C3-ung	3.03 ± 0.13	6	1.11 ± 0.15	6
MAC 87301	C3-ung	4.12 ± 0.13	3	0.83 ± 0.14	6
Coolidge	C4-ung	2.67 ± 0.14	6	0.59 ± 0.13	6
LAP 04757	Chondrite-ung	–0.19 ± 0.13	1	–0.33 ± 0.13	6
LAP 04773	Chondrite-ung	–0.54 ± 0.13	3	–0.46 ± 0.16	6
GRO 95566	CM-an	3.50 ± 0.15	3	0.92 ± 0.13	3
Aguas Zarcas A	CM2	2.21 ± 0.18	6	0.98 ± 0.13	6
Aguas Zarcas B	CM2	2.86 ± 0.23	6	0.88 ± 0.13	6
Murchison	CM2	2.81 ± 0.13	5	1.10 ± 0.15	6
Murray	CM2	2.67 ± 0.13	6	0.84 ± 0.13	6
Isna	CO3.8	2.83 ± 0.13	6	0.66 ± 0.14	6
Allende	CV3	-	-	0.87 ± 0.13	6
Allende	CV3	-	-	0.94 ± 0.13	6
DTS-1	Ter. Std.	-	-	0.06 ± 0.13	6
BCR-2	Ter. Std.	–0.04 ± 0.13	5	-	-
BCR-2	Ter. Std.	–0.03 ± 0.17	6	-	-

4.4 Discussion

4.4.1 Constraining the range of Cr and Ti isotopic compositions for CM and CO chondrites

While the primary focus of this study is on the CM and CO chondrites and ungrouped chondrites potentially related to these chondrite groups, it is important to note the Cr and Ti isotopic compositions of all the carbonaceous chondrite groups. Overlaps in isotopic composition in ε^{50}Ti vs. ε^{54}Cr space are observed between certain groups, and the ε^{50}Ti vs. ε^{54}Cr fields for all carbonaceous chondrite groups are in close proximity to each other (Fig. 4.2). Nevertheless, clear separation between most groups and a general inverse correlation between ε^{50}Ti and ε^{54}Cr is observed. The carbonaceous chondrite group compositional fields are defined by limited data points that represent ε^{50}Ti and

ε^{54}Cr values from separate aliquots of individual meteorites measured by different laboratories or, in the case of the CR chondrites, separate meteorites altogether (see references in Fig. 4.2). The close proximity of these compositional fields, overlapping fields of some groups, limited data, and the prevalence of ε^{54}Cr and ε^{50}Ti compositions being reported for separate sample aliquots of inherently heterogeneous meteorites highlights the need for additional data to continue to accurately establish the carbonaceous chondrite group compositional fields and thereby further enable their use for accurate assessments of potential genetic relationships between samples.

Prior to this study, the compositional fields in ε^{50}Ti vs. ε^{54}Cr space for the CM and CO chondrite groups were defined by just two meteorites for each group (Fig. 4.2A). All other CM and CO chondrites measured for Cr or Ti isotopes were only measured for one element and not the other, limiting the usefulness of those data for the purpose of establishing compositional fields in ε^{50}Ti vs. ε^{54}Cr space. In this work, we have begun to address the need for additional correlated bulk carbonaceous chondrite data by measuring both the ε^{54}Cr and ε^{50}Ti isotopic compositions of single aliquots of three CM2 chondrites (Murray, Murchison, and Aguas Zarcas) and one CO3.8 chondrite (Isna). These new data are plotted in Fig. 4.2B and redefine the extent of the CM and CO chondrite fields compared to those shown in Fig. 4.2A.

The CO chondrite field for ε^{50}Ti extends from 2.83 ± 0.13 for CO3.8 Isna (this work) to 4.69 ± 0.12 for CO3.3 Felix (Trinquier at al., 2009). The previously lowest reported value for ε^{50}Ti was 3.46 ± 0.10 for CO3.5 Lancé (Zhang et al., 2012), so this study extends the lower boundary of the field. Additionally, a previous measurement of Isna reported an ε^{50}Ti value of 3.54 ± 0.07 (Trinquier et al., 2009), illustrating the Ti

isotopic heterogeneity present even within individual samples. The CO chondrite field for ε^{54}Cr has a comparatively small range that extends from 0.57 ± 0.11 for Lancé (Trinquier et al., 2007) to 1.02 ± 0.24 for Kainsaz (Shukolyukov and Lugmair, 2006), and the measurement of Isna from this study falls within this range.

The CM chondrite field for ε^{54}Cr previously extended from 0.93 ± 0.09 for Paris (Göpel et al., 2015) to 1.59 ± 0.11 for Niger (C2) (Göpel et al., 2015). Our study now extends the lower boundary to 0.84 ± 0.13 for Murray (a previous measurement of Murray obtained 1.13 ± 0.21; Shukolyukov and Lugmair, 2006). The CM chondrite field for ε^{50}Ti previously defined a narrow range from 2.84 ± 0.05 for Murray (Zhang et al., 2012) to the 3.03 ± 0.23 average of several measurements of Murchison, including some measurements that overlap with the Murray value (Trinquier et al., 2009; Zhang et al., 2011). In this study, we report a measurement of Murray (2.67 ± 0.13) and a measurement of Aguas Zarcas (2.21 ± 0.18) from its chondrule-poor lithology (~80 area%; Gattacceca, 2019) that extend the lower boundary of this range. We also measured a separate sample of Aguas Zarcas from its chondrule-rich lithology (~20 area%; Gattacceca, 2019) with an ε^{50}Ti composition of 2.86 ± 0.23, which is within error of previous CM chondrite values, further illustrating the Ti isotopic heterogeneity present within individual carbonaceous chondrites. Even with these added data, the CM and CO chondrites define distinct compositional fields in ε^{54}Cr vs. ε^{50}Ti space (Fig. 4.2B).

It is apparent from Fig. 4.2 that the addition of a small number of samples (in the case of the CM chondrites) or even a single sample (in the case of the CO chondrites) can significantly change the extent of the compositional field for a given carbonaceous chondrite group in ε^{54}Cr vs. ε^{50}Ti space. This is largely a factor of the limited existing

data and suggests that additional data will likely further redefine these compositional fields. The ungrouped chondrites that possess intermediate compositions that plot outside of the established compositional fields suggest the possibility that additional ungrouped samples and asteroid samples returned via sample return missions could potentially plot in such intermediate regions, which would then potentially signify a continuum of compositions. Future measurements of carbonaceous chondrites and returned carbonaceous asteroid samples will therefore continue to provide additional constraints on our understanding of the relationships among carbonaceous chondrite groups and their respective parent bodies.

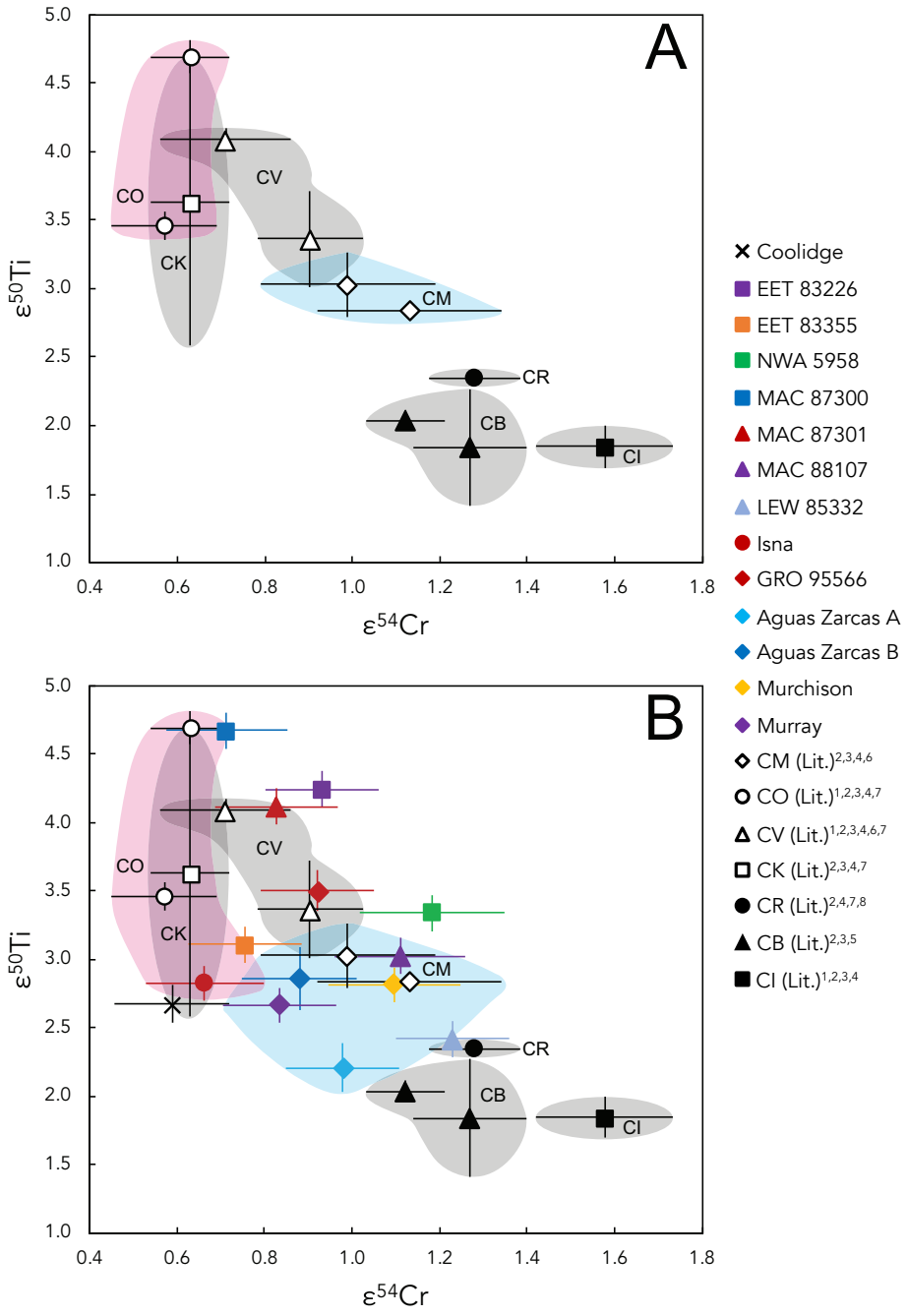

Fig. 4.2. A) $\varepsilon^{54}Cr$ vs. $\varepsilon^{50}Ti$ reported for carbonaceous chondrites in the literature prior to this study (black and white symbols). Literature data, as denoted by corresponding superscripts in the legend, are from: 1) Shukolyukov and Lugmair (2006) 2) Trinquier et al. (2007), 3) Trinquier et al. (2009), 4) Qin et al. (2010), 5) Yamashita et al. (2010), 6) Zhang et al. (2011), 7) Zhang et al. (2012), and 8) Sanborn et al. (2019). B) $\varepsilon^{54}Cr$ vs. $\varepsilon^{50}Ti$ for the samples studied here (colored symbols) plotted with values reported in the literature prior to this study (black and white symbols). Literature data points represent the $\varepsilon^{54}Cr$ and $\varepsilon^{50}Ti$ values of individual meteorites for CI, CB, CM, CO, CV, and CK

chondrites and the mean ε^{54}Cr and ε^{50}Ti values for CR chondrites. Shaded and labeled regions represent the data fields for each carbonaceous chondrite group in ε^{54}Cr vs. ε^{50}Ti space. The pink field represents CO chondrites, the blue field represents CM chondrites, and all other chondrite groups are represented by gray fields.

The variation in isotopic compositions among samples from the same chondrite group and among different aliquots of the same samples highlights both the importance and difficulty of representatively sampling inherently heterogeneous samples. We have made an effort in this work to measure the largest feasible sample sizes, but because of the sample-limited nature of some meteorites this will continue to be an issue worthy of attention in studies that analyze and interpret bulk meteorite data. A potential cause of isotopic heterogeneity in bulk carbonaceous chondrite measurements is the non-representative sampling of isotopically anomalous phases such as calcium-aluminum-rich inclusions (CAIs) and chondrules. CAIs (median ε^{50}Ti of ~9 and median ε^{54}Cr of ~5; e.g., Chapter 3 of this dissertation and references therein) are likely to have a more significant effect than chondrules, which have ε^{50}Ti and ε^{54}Cr anomalies of a generally smaller magnitude both above and below bulk carbonaceous chondrite compositions (e.g., Olsen et al., 2016; Gerber et al., 2017). The non-representative sampling of CAIs would also have a more significant effect on bulk ε^{50}Ti values than ε^{54}Cr because of the much higher elemental concentration of Ti in CAIs relative to carbonaceous chondrite matrix. This effect is illustrated in Fig. 4.3, in which a ~5% oversampling of CAI material from a bulk Allende CV chondrite composition is sufficient to cause a shift in ε^{50}Ti of ~1ε while ε^{54}Cr remains unaffected. Most of the spread in ε^{50}Ti of representatively sampled bulk carbonaceous chondrites is likely because of the varying CAI abundances inherent in the difference chondrite groups as documented by petrologic investigations (see Weisberg et

al., 2006 for a summary), but it is nevertheless important to consider the potential effects of sample heterogeneity.

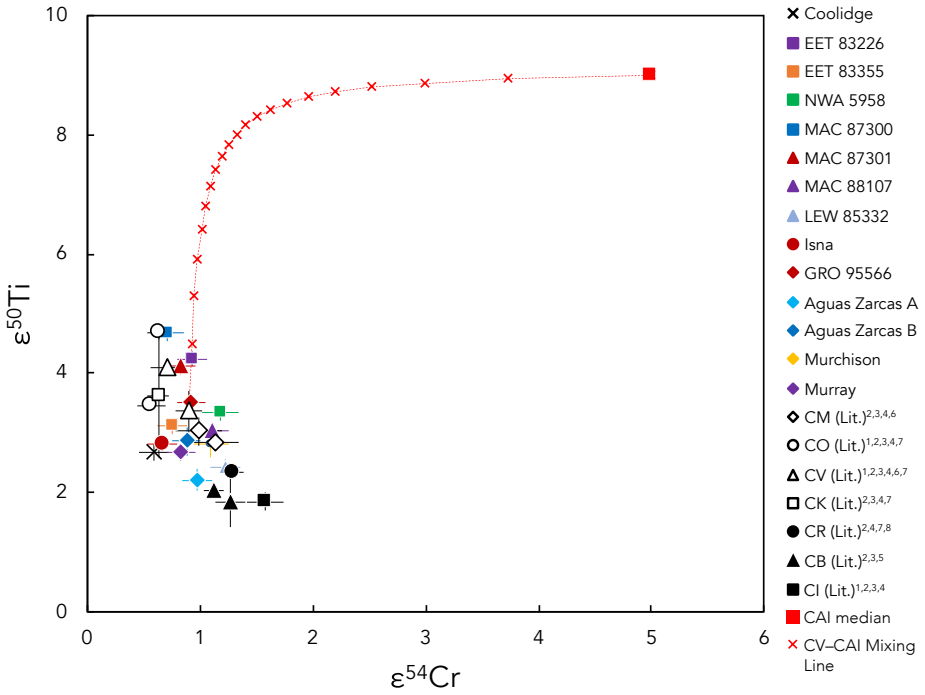

Fig. 4.3. A mixing line in $\varepsilon^{54}Cr$ vs. $\varepsilon^{50}Ti$ space between bulk Allende CV chondrite composition and median CAI composition plotted along with bulk carbonaceous chondrite data from this study and the literature (same references as literature data shown in Fig. 4.2). The CV endmember of the mixing line is defined by the elemental abundances (Cr = 3600, Ti = 899 ppm) and isotopic compositions ($\varepsilon^{54}Cr = 0.90 \pm 0.12$, $\varepsilon^{50}Ti = 3.36 \pm 0.36$) previously reported for Allende (e.g., Shukolyukov and Lugmair, 2006; Trinquier et al., 2007, 2009; Qin et al., 2010; Zhang et al., 2012; Alexander et al., 2019; Torrano et al., 2019; this study). The CAI endmember of the mixing line is defined by the mean elemental abundances (Cr = 418 ppm, Ti = 4218 ppm) in the CAIs studied by Torrano et al. (2019) and the median Cr and Ti isotopic compositions of CAIs from the literature ($\varepsilon^{50}Ti = 9$ and $\varepsilon^{54}Cr = 5$; e.g., Schauble and Dauphas, 2016 and references therein; Davis et al., 2018; Render et al., 2019; Torrano et al., 2019). Each "x" symbol on the mixing line represents a 5% increment of CAI addition to a bulk Allende composition.

In order to assess the potential contribution of non-representative sampling of anomalous phases in the samples studied here, we have compared the $\varepsilon^{50}Ti$ values to Ca and Al elemental abundances (as a proxy for CAI content) in the samples studied here (Fig. 4.4). We have focused on those samples which are paired or for which multiple

aliquots from the same meteorite were measured because this allows us to assess the effect of relative differences in elemental abundances that should be similar. If any of these measurements oversampled isotopically anomalous CAI material, we would expect to see elevated Ca and Al elemental abundances and a correspondingly elevated ε^{50}Ti isotopic composition. Such a correlation is seen between the paired samples MAC 87301 and MAC 87300, with an increase in both Ca and Al abundances of ~0.5 wt.% for MAC 87300 corresponding to an increase in ε^{50}Ti of ~0.5. Such a ~0.5 wt.% increase in Ca and Al abundances could potentially be accounted for by a ~5–10% oversampling of CAI material, which would correspond to a predicted increase in ε^{50}Ti of ~0–1 depending on the isotopic composition of the CAI, which is consistent with the measured ε^{50}Ti value. It must be considered, however, that such a correlation between Ca and Al abundances and ε^{50}Ti may simply reflect natural variations in elemental abundances and isotopic compositions of bulk meteorites (including natural variations in CAI abundances). No correlation between Ca and Al abundances and ε^{50}Ti is observed for the paired samples EET 83355 and EET 83226, and an inverse correlation is observed for two aliquots of Aguas Zarcas, suggesting that oversampling of CAIs was not a factor in the varying ε^{50}Ti values measured among these samples (Fig. 4.4). Furthermore, Murray and Murchison show a ~1 wt.% difference in Ca and Al abundances but ε^{50}Ti values that are the same within error (Fig. 4.4). Additionally, a general lack of correlation between Ca and Al abundances and ε^{50}Ti values is observed in the sample set as a whole. All bulk carbonaceous chondrites measured here exhibit Ca and Al abundances of ~1–2.5 wt.%, and our results suggest that most such variation is caused by natural sample variation and not oversampling of CAIs. Calculations of the potential effect of oversampling of CAIs

on ε^{50}Ti values, however, reiterate the necessity of careful sampling practices to ensure representative sampling of bulk meteorites.

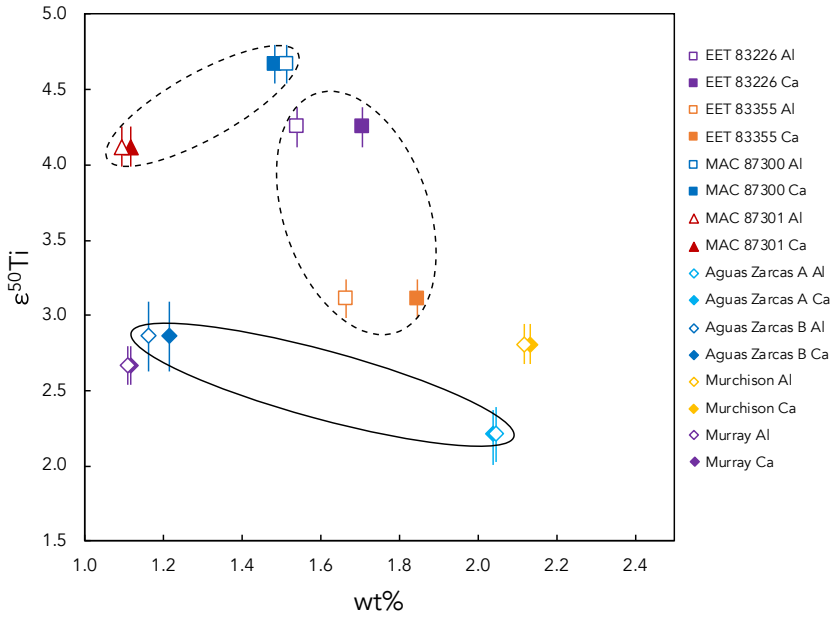

Fig. 4.4. ε^{50}Ti vs. wt.% for several samples studied here with wt.% Al indicated by open symbols and wt.% Ca indicated by filled symbols. The dashed ovals indicate paired meteorites EET 83226/83355 and MAC 87300/87301 and the solid oval indicates multiple aliquots of a single meteorite (Aguas Zarcas). Also plotted are Murchison and Murray.

4.4.2 Evaluating potential genetic relationships in ε^{50}Ti vs. ε^{54}Cr isotope space

The ε^{54}Cr and ε^{50}Ti compositions of ungrouped chondrites can be used to evaluate the potential genetic relationships between these samples and one or more known chondrite groups. In the following section, we discuss each of the ungrouped and anomalous samples measured here, review previous suggestions of genetic relationships with established chondrite groups, and evaluate these interpretations using the new isotopic data acquired in this study.

4.4.2.1 EET 83355 and EET 83226

EET 83355 is a C2 ungrouped chondrite that was suggested to be a heated CM chondrite based on bulk H, C, and N abundances (Alexander et al., 2013), but subsequent work revealed differences from the CM chondrites including lower phyllosilicate abundance (Garenne et al., 2014) and systematically lower carbonate C contents and carbonate $\delta^{13}C$ values (Alexander et al., 2015). This sample plots within the CO chondrite region in $\varepsilon^{54}Cr$ vs. $\varepsilon^{50}Ti$ space, but both its $\varepsilon^{54}Cr$ and $\varepsilon^{50}Ti$ values also overlap those defined by the CM chondrite region, suggesting a possible genetic relationship with both groups. This sample exhibits similarities to EET 83226, suggesting that they may be paired (Grossman, 1994). EET 83226 is a C2 ungrouped chondrite that exhibits compositional similarities to the CV-CK clan and CO chondrites, with chondrule diameters and matrix mineralogy consistent with classification as an anomalous CO chondrite (Abreu et al., 2018). Secondary mineralogy shows affinities to the CM, CR, and CI chondrites (Abreu et al., 2018), and reflectance spectra are similar to those of CM chondrites (Takir et al., 2019). Based on compositional and petrologic analyses, Abreu et al. (2018) proposed a classification as an anomalous CO chondrite and suggested this may be evidence that the CO chondrite parent body underwent low temperature aqueous alteration. In $\varepsilon^{54}Cr$ vs. $\varepsilon^{50}Ti$ space, EET 83226 plots outside of any established field, with an elevated $\varepsilon^{50}Ti$ composition similar to the CO, CV, and CK chondrites, and an $\varepsilon^{54}Cr$ composition similar to the CM and CV chondrites (Fig. 4.2). Its $\varepsilon^{50}Ti$ composition is distinct from EET 83355, while its $\varepsilon^{54}Cr$ is higher but within error of EET 83355. This suggests that these samples may be paired and the $\varepsilon^{50}Ti$ difference is more affected by sample heterogeneity than $\varepsilon^{54}Cr$ as discussed earlier. The $\varepsilon^{54}Cr$ and $\varepsilon^{50}Ti$ isotopic

compositions of EET 83355, combined with previous petrologic and compositional analyses, suggest that this sample may originate on the CO chondrite parent body or a parent body with similar petrologic and isotopic characteristics. If EET 83355 does share a parent body with EET 83226, the isotopic compositions suggest that these two samples may come from a distinct parent body that shares certain characteristics with both CM and CO chondrites.

4.4.2.2 MAC 87300, MAC 87301, and MAC 88107

MAC 87300 (C2-ung), MAC 87301 (C3-ung), and MAC 88107 (C3-ung) are ungrouped chondrites that have undergone little or no parent body alteration and were all initially classified as C2 chondrites (Satterwhite and Mason, 1988; Martinez and Mason, 1989). Further work by Sears et al. (1990) noted similarities between the thermoluminescence values among these samples and their similarity to those of the CO3 chondrites, suggesting either a potential extension of the CO3 chondrite field or a continuum between the CM, CO, and CI chondrites. Kallemeyn (1992) considered MAC 87300 and MAC 87301 to be paired based on their nearly identical thermoluminescence and lithophile and siderophile abundances, which are also similar to MAC 88107. These three meteorites exhibit refractory lithophile and refractory and common siderophile elemental abundances similar to the CM and CO chondrites, moderately volatile lithophile abundances similar to CO chondrites and distinct from CM chondrites, and abundances of siderophile and chalcophile elements more volatile than Au that are intermediate between CM and CO chondrites (Kallemeyn, 1992). These meteorites also fall between CM and CO chondrites for Zn/Mn vs. Al/Mn abundance ratios, with a slight

affinity towards CO chondrite composition (Kallemeyn, 1992). Based on these compositional data, Kallemeyn (1992) suggested that MAC 87300, MAC 87301, and MAC 88107 should be considered an independent grouplet of ungrouped chondrites. Subsequent work has suggested that MAC 87300 is related to heated CM, CR, and CI chondrites based on its similar, albeit more Fe-rich, matrix composition (Zolensky et al., 1993), and both MAC 87300 and MAC 88107 also exhibit reflectance spectra similar to chondrites from these groups (Hiroi et al., 1997). Whole-rock oxygen isotopic compositions, however, are dissimilar to those of CM chondrites (Clayton and Mayeda, 1999), and instead led those authors to suggest that MAC 87300 and MAC 88107 are related to the CO, CV, or CK chondrites. Additional measurements of the O-isotope compositions of fayalite, magnetite, and chondrule olivine in MAC 88107 (Krot and Nagashima, 2012) and comparison with measurements of those phases in CO chondrites led Doyle et al. (2013) to suggest the reclassification of MAC 88107 as a CO3.1 chondrite. The primary mineralogy of CAIs in MAC 87300 and MAC 88107 additionally support a relationship with the CO3 chondrites, although the presence of phyllosilicates suggests that CAIs from these meteorites have experienced a greater degree of aqueous alteration than that experienced by the CO3 chondrites (Russell et al., 2000).

In ε^{54}Cr vs. ε^{50}Ti space, MAC 87300 falls within the CO chondrite field and has one of the highest ε^{50}Ti values measured in a carbonaceous chondrite, similar to the CO3.3 chondrite Felix (Trinquier et al., 2009), although it also overlaps with CM chondrite ε^{54}Cr values (Fig. 4.2). MAC 87301 does not fall within the CO or CM fields, instead plotting near the CV chondrites (Fig. 4.2). It does, however, exhibit a ε^{50}Ti composition similar to CO chondrites and a ε^{54}Cr composition similar to CM chondrites

that overlaps with CO chondrites (and MAC 87300), suggesting intermediate characteristics between these groups. MAC 88107 falls in the CM chondrite region close to the Murchison compositions measured here and Murray compositions measured previously, with elevated ε^{54}Cr compositions compared to the CO chondrites, MAC 87300, and MAC 87301 (Fig. 4.2). These data are consistent with the pairing of MAC 87300 and MAC 87301, which overlap in ε^{54}Cr and have a difference in ε^{50}Ti that could be explained by sample heterogeneity and/or non-representative sampling of isotopically anomalous components that effect ε^{50}Ti more than ε^{54}Cr values. The isotopic data collected in this study suggest that MAC 87300 and MAC 87301 likely originated on a common parent body similar in precursor material and formation region to the CO chondrites but distinct from the parent body of MAC 88107, which was likely closer in composition and formation region to the CM chondrite parent body.

4.4.2.3 Coolidge

Coolidge is a C4 ungrouped chondrite that was initially thought to be related to the CV chondrites (Kallemeyn and Wasson, 1982). However, a combination of petrographic characteristics such as matrix and chondrule abundances combined with a bulk composition that is not consistent with established carbonaceous chondrite groups for Zn/Mn vs. Al/Mn, Sb/Ni vs. Ir/Ni, and Ga/Mg vs. Sb/Mg, led Kallemeyn and Rubin (1995) to consider Coolidge to be part of a grouplet with Loongana 001 that is distinct from the established carbonaceous chondrite groups. In ε^{54}Cr vs. ε^{50}Ti space, Coolidge plots close to the CO chondrite field with an ε^{54}Cr composition similar to the CO chondrites and an ε^{50}Ti composition that overlaps with CO, CM, and CK values,

suggesting a potential relationship with multiple groups (Fig. 4.2). Furthermore, the isotopic data presented here provide further evidence that Coolidge is not related to the CV chondrites. Although Coolidge shows an affinity for the CO chondrites based on Cr and Ti isotopic data, petrologic and compositional differences detailed in previous studies suggest that this isotopic affinity is likely because of formation in a common region and not on a common parent body.

4.4.2.4 GRO 95566

GRO 95566 (CM-an) exhibits refractory lithophile abundances intermediate between the CV–CK and CM–CO chondrites, CM-like volatile lithophile abundances, refractory lithophile abundances near CM, CO, and CV chondrites, CM-like volatile siderophile and chalcophile abundances, plots within the CM field in Zn vs. Sm space, and plots between the CM and CO fields in Sb vs. Ga space (Choe et al., 2010). The average chondrule diameter of 310 μm (Choe et al., 2010) is similar to the ~300 μm mean diameter reported for CM chondrites (e.g., Friedrich et al., 2015). The O-isotope composition of GRO 95566 is ^{16}O-rich for a CM chondrite (Fig. 4.1; Clayton and Mayeda, 1999), instead compositionally similar to CO chondrites. This O-isotope composition was the primary basis for its classification as an anomalous CM chondrite by Choe et al. (2010). GRO 95566 plots in the CV chondrite field in ε^{54}Cr vs. ε^{50}Ti space within error of Allende (Fig. 4.2). It exhibits an ε^{50}Ti composition similar to CO chondrites and an ε^{54}Cr composition similar to CM chondrites. The elevated ε^{50}Ti composition of GRO 95566 compared to CM chondrites may be an extension of the established CM chondrite field, thus increasing the overlap between the CV and CM

fields. The combination of isotopic, elemental, and petrologic data suggests that GRO 95566 may represent minimally altered material on the CM parent body (Choe et al., 2010) or may originate from a distinct parent body formed from similar precursor material in a similar region.

4.4.2.5 LEW 85332

LEW 85332 is a C3 ungrouped chondrite, and early work noted that it exhibits similar refractory lithophile and siderophile abundances to the CI and CR chondrites but has volatile siderophile abundances that are lower than the former and higher than the latter (Rubin and Kallemeyn, 1990). This sample also exhibits petrologic characteristics similar to the CO chondrites and was originally classified as a CO3 chondrite on the basis of its chondrule sizes (mean diameter = 170 μm; Mason, 1987; Rubin and Kallemeyn, 1990), which are similar to the mean values of 148 +132/–70 μm reported by Rubin (1989) for chondrules from CO chondrites. However, the refractory lithophile abundances and common and volatile siderophile abundances are inconsistent with those of CO or CM chondrites (Rubin and Kallemeyn, 1990). Additionally, matrix phyllosilicates suggest a relationship with CI and CR chondrites, but not CM chondrites (Brearley, 1997). A relationship with the CR chondrites was also suggested by petrologic characteristics and O-isotope compositions of the bulk meteorite and individual chondrules (Prinz et al., 1992, 1993; Clayton and Mayeda, 1999). Recent analyses of the bulk and insoluble organic matter (IOM) H-C-N elemental abundances and isotopic compositions demonstrate that this samples falls below the unheated CR water-IOM mixing line but above the heated CR chondrites (Alexander et al., 2018). Alexander et al.

(2018) further suggest that the IOM compositions and retention of metal may indicate origin on a distinct parent body that accreted water with a lower δD than the CR chondrites. Additional evidence that LEW 85332 is not a CR chondrite comes from its mean chondrule diameter of 170 μm (Rubin and Kallemeyn, 1990), which is smaller than the average diameter of 700 μm reported by Kallemeyn et al. (1994). Interestingly, LEW 85332 plots in the CR chondrite field in ε^{54}Cr vs. ε^{50}Ti space in agreement with O-isotope data (Fig. 4.2). It also overlaps with the CM chondrite field, suggesting that this sample records compositional features of multiple groups. LEW 85332 is therefore best considered an ungrouped chondrite possessing affinities to multiple groups and illustrates the importance of conducting comprehensive combined petrologic, *in situ* chemical, bulk elemental, and isotopic analyses for the purpose of evaluating genetic relationships and parent body origins. The apparent disagreement of different data sets in identifying a parent body origin of LEW 85332 suggests that this sample may originate from one of perhaps many diverse carbonaceous chondrite parent bodies that are not recorded by established chondrite groups. Instead, such parent bodies may have formed from similar precursor material or in nearby regions to multiple chondrite group parent bodies and thus record characteristics of multiple groups.

4.4.2.6 NWA 5958

NWA 5958 is a C2 ungrouped chondrite that exhibits depletion in moderately volatile elements similar to CM chondrites and an O-isotope composition that plots between the CM and CO chondrites (Jacquet et al., 2016). Based on petrographic and geochemical evidence, Jacquet et al. (2016) concluded that NWA 5958 is a CM-like C2

ungrouped chondrite that samples a parent body intermediate between those of CM and CO chondrites. In ε^{54}Cr vs. ε^{50}Ti space, NWA 5958 plots outside of any established carbonaceous chondrite field with an ε^{54}Cr composition similar to CM chondrites and an ε^{50}Ti composition similar to CO chondrites (Fig. 4.2). These data support the assertion of Jacquet et al. (2016) that NWA should be considered a CM-like C2 ungrouped chondrite that may share parent body characteristics with both CM and CO chondrites, including potentially sharing precursor material and/or a formation region.

4.4.2.7 LAP 04757 and LAP 04773

Approximately 90% of all classified meteorites fall into the H, L, and LL ordinary chondrite groups (Krot et al., 2013), which are based on characteristics such as bulk chemical and isotopic composition and oxidation state (e.g., Rubin, 2005). Some ungrouped chondrites show similarities to ordinary chondrites but are compositionally inconsistent with being from the established ordinary chondrite groups. Among these are those characterized by the low FeO abundances of their mafic silicates compared to the range observed in most H chondrites, which are referred to as the low-FeO chondrites (Russell et al., 1998). Several causes for the low-FeO nature of these meteorites were proposed by Wasson et al. (1993), including the incorporation of greater amounts of a reducing agent such as carbon, anomalous pressure and temperature conditions during metamorphism, and mixing with reducing agents in the parent body regolith. While Wasson et al. (1993) favored mixing with reducing agents on the parent body, subsequent studies suggested that the differences between the low-FeO chondrites and H chondrites were because of varying incorporation of nebular material and not parent body reduction

of H chondrites (McCoy et al., 1994; Russell et al., 1998; Troiano et al., 2011; Schrader et al., 2017). Based on petrologic evidence including the lack of low-FeO chondrite clasts in H chondrite breccias, it has been suggested that low-FeO chondrites represent a distinct ordinary chondrite parent body (McCoy et al., 1994).

Two paired samples studied here, LAP 04757 and LAP 04773, are ungrouped chondrites that were initially thought to be related to the acapulcoites or low-FeO chondrites (Righter, 2007). Further study of LAP 04757 led to its identification as a low-FeO chondrite based on similarities to H chondrites in bulk elemental composition, siderophile abundances, lithophile abundances, moderately volatile element abundances, opaque mineral abundances, and O-isotope compositions (Troiano et al., 2011). LAP 04773 is also considered to be a low-FeO chondrite (e.g., Yamaguchi et al., 2019). In ε^{54}Cr vs. ε^{50}Ti space, LAP 04773 plots within error of the H, L, and LL chondrites for both ε^{54}Cr and ε^{50}Ti (Fig. 4.5). LAP 04757 plots within error of the H, L, and LL chondrites for ε^{54}Cr and exhibits slightly elevated ε^{50}Ti that is nevertheless within error of the wide range defined by H chondrites (Fig. 4.5). Both samples plot in a distinct region from acapulcoites, confirming that they are unrelated to this meteorite group. These isotopic data provide support for the classification of LAP 04757 and LAP 04773 as low-FeO chondrites. Furthermore, the isotopic composition of LAP 04757 provides evidence that low-FeO chondrites originated from a distinct parent body and are not reduced H chondrites, consistent with the conclusion of McCoy et al. (1994).

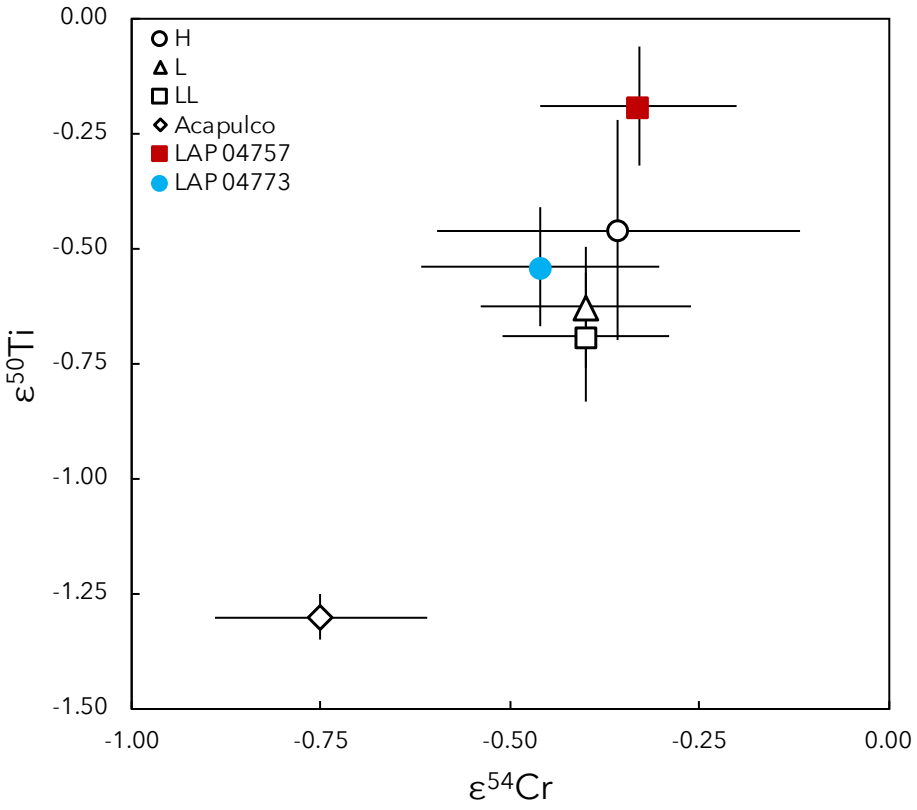

Fig. 4.5. $\varepsilon^{54}Cr$ vs. $\varepsilon^{50}Ti$ for LAP 04757 and LAP 04773 plotted along with H, L, and LL ordinary chondrites and Acapulco. The H, L, and LL data points represent the mean $\varepsilon^{54}Cr$ (from four H, two L, and three LL chondrites) and $\varepsilon^{50}Ti$ (from two H, three L, and four LL chondrites) values from the literature (Trinquier et al., 2007, 2009; Qin et al., 2010; Zhang et al., 2012).

4.4.3 Implications for the relationship between CM and CO chondrites

A close relationship between the CM and CO chondrites has been suggested based on bulk elemental and O-isotope compositions (e.g., Kallemeyn and Wasson, 1981; Clayton and Mayeda, 1999; Weisberg et al., 2006; Greenwood et al., 2014) as well as similar chondrule and matrix olivine compositions (Frank et al., 2014; Schrader and Davidson, 2017). Although the gap in three-oxygen isotope space between CM and CO chondrites may be considered an argument against a common parent body origin, it has been suggested that it could instead indicate a common parent body origin in which CO

chondrites sample an anhydrous core, CM chondrites sample aqueously altered outer material, and CO- and CM-like ungrouped chondrites sample an intermediate composition (e.g., Greenwood et al., 2014). Further isotopic analyses of individual bulk meteorites provide an additional method for an evaluation of this potential genetic relationship.

In ε^{54}Cr vs. ε^{50}Ti space and in three-oxygen isotope space, the CM and CO chondrites plot as distinct and adjacent fields (Fig. 4.1 and Fig. 4.2). Whereas aqueous alteration has been shown to affect bulk O-isotope compositions (e.g., Clayton and Mayeda, 1999; Schrader et al., 2011; 2014), Sanborn et al. (2015) showed that bulk ε^{54}Cr values are not affected by aqueous alteration. As discussed by Schrader and Davidson (2017), the fact that the distinct ε^{54}Cr values of CM and CO chondrites are unaffected by aqueous alteration is evidence that they originated from distinct parent bodies and not on a single parent body that experienced different degrees of aqueous alteration as proposed by Greenwood et al. (2014). Several C2 ungrouped and anomalous CM chondrites plot in the compositional gap between CM and CO chondrites in three-oxygen isotope space (Fig. 4.1), and in this study we measured two of these samples and several additional ungrouped chondrites with documented affinities to the CM and/or CO chondrites. In ε^{54}Cr vs. ε^{50}Ti space, the samples that plot in the compositional gap between CM and CO chondrites in three-oxygen isotope space (NWA 5958 and GRO 95566; Fig. 4.1) plot outside the established CM and CO chondrite fields (Fig. 4.2), suggesting that they likely originated on distinct parent bodies. The other ungrouped chondrites show varying degrees of isotopic similarity to the CM and/or CO chondrites, as well as other chondrite groups. Only one sample (EET 83355) overlaps with both the CM and CO chondrite

fields, and no clear trend or cluster of data between these fields is observed as might be expected if these samples represented intermediate compositions from a common parent body. Instead, these data, combined with previous O-isotope compositions, elemental abundances, and petrologic investigations, suggest that the CM, CO, and related ungrouped chondrites likely originated from distinct parent bodies that may have formed from similar precursor material and/or in nearby regions that shared isotopic similarities.

4.4.4 Implications for the formation time and location of ungrouped chondrite parent bodies

A speculative model proposed by Melosh et al. (2017) suggested that dynamical processes in the disk led to radial separation of distinct regions of dust separated by regions of gas, and that each individual band of dust in such a scenario was the formation region of the parent body of a distinct chondrite type. In this model, all parent bodies formed in a given band would preserve distinctive chemical and isotopic signatures of that region of the nebula. If the structure of the early Solar System did resemble this model, it is conceivable that the CM and CO chondrite parent bodies could have formed from adjacent or nearby dust bands. Ungrouped chondrites that exhibit similar properties to known groups could originate from distinct parent bodies formed from different regions of a common band of precursor material, from a common band at a different time, or from intermediate dust bands. Such a formation model could therefore explain observed chemical and isotopic similarities.

A quantitative model predicting the heliocentric distance of meteorite parent body formation based on age constraints and refractory abundances was put forward by Desch

et al. (2018). This model predicts that the carbonaceous chondrite parent bodies formed at ~2–5 Ma after the beginning of the Solar System outside the orbit of Jupiter beyond a pressure bump that prevented millimeter- and centimeter-sized particles from reaching the inner disk. This is consistent with concurrent work by Scott et al. (2018) that invoked formation in such a region to explain the enrichment of carbonaceous chondrites in refractory inclusions, refractory elements, and water. The robustness of the Desch et al. (2018) model is supported by its accurate prediction of spectral matches to asteroids, water content, and mean chondrule diameters. The model predicts that CO chondrites formed at 3.72 AU and 2.7 Ma and that CM chondrites formed later at 3.76 AU and 3.5 Ma. These ages of formation relative to the beginning of the Solar System (defined by CAIs) are based on previously reported Al-Mg ages of chondrules in CO and CM chondrites (Kurahashi et al., 2008), Mn-Cr ages of carbonate formation in CM chondrites (de Leuw et al. 2009; Fujiya et al. 2013; Jilly et al. 2014), timing of aqueous alteration in CM chondrites (Lee et al., 2012), and thermal modeling of CM and CO chondrites (Sugiura and Fujiya, 2014), and the heliocentric distances are based on refractory abundances (Scott and Krot, 2014). By comparison, the model predicts formation of CK chondrites at 3.6 AU and 2.2 Ma, CV chondrites at 3.6 AU and 2.6 Ma, CR chondrites at 3.84 AU and 4.0 Ma, and CI chondrites at >15 AU and 3.0 Ma after the beginning of the Solar System. Desch et al. (2018) suggest that heating of gas by spiral shocks caused by Jupiter, combined with parent-body thermal metamorphism, could explain why the CO, CV, and CK chondrites (which formed earlier and closer to Jupiter's pressure bump region) lack the water preserved in CM, CR, and CI chondrites. If heating caused by the pressure bump does explain the lower water content in CO chondrites, this heating may

have stopped by the time of formation of the CM chondrite parent body ~0.8 Ma later or may not have reached its formation region (Desch et al., 2018). The origin of CM and CO chondrites from distinct parent bodies that formed in regions separated spatially by ~0.04 AU and temporally by ~0.8 Ma is consistent with the distinct petrologic characteristics and isotopic compositions of these meteorites. In such a scenario, the ungrouped chondrites with documented affinities for CM and/or CO chondrites may therefore sample distinct parent bodies which formed near ~3.72–3.76 AU and at a time near ~2.7–3.5 Ma, thus sampling similar precursor material and isotopic reservoirs to the CM and CO chondrites.

4.4.5 Implications for asteroid sample return missions

Initial results from the OSIRIS-REx and Hayabusa2 spacecraft suggest that the spectral properties and albedo measurements of Bennu (B-type) and Ryugu (C-type) share similarities with CM chondrites (e.g., Hamilton et al., 2019; Kitazato et al., 2019; Lauretta et al., 2019), but features of other chondrite groups are present as well. For Bennu, spectral feature at 0.55 μm is likely indicative of the presence magnetite, which supports an affinity with both CI and CM chondrites (Lauretta et al., 2019). For Ryugu, no meteorites provide an exact match, but the closest analogs appear to be thermally metamorphosed CI chondrites and shocked CM chondrites (Kitazato et al., 2019). Additionally, there is an indication of the presence of Mg-rich phyllosilicates on Ryugu, which are known to be present in aqueously altered CI and CM chondrites (Kitazato et al., 2019). If Bennu and Ryugu are related to the CM chondrites, the Desch et al. (2018) model suggests that these asteroids likely formed near 3.76 AU at approximately 3.5 Ma

after the beginning of the Solar System. If these asteroids are instead related to CI chondrites, this would suggest formation at an earlier time and much greater heliocentric distance.

The results of our study demonstrate the diversity represented by the carbonaceous chondrites, particularly among those which show affinities to the CM and CO chondrites. Isotopic data, combined with elemental abundance measurements and petrologic investigations, suggest that the CM, CO, and related ungrouped chondrites likely originated from distinct parent bodies that may have formed from similar precursor materials and/or in nearby regions in the protoplanetary disk. Because of initial data suggesting that both Bennu and Ryugu are likely related to the CM chondrites, it is possible that these bodies formed from similar precursor materials and from a similar nebular reservoir. Suggestions of similarities to the CI chondrites further suggests that these asteroids may be similar to ungrouped chondrites that show affinities to multiple chondrite groups. Therefore, the samples returned from Bennu and Ryugu may provide important insights into the origins of such meteorites with the significant added benefit of geologic context. These samples will also provide a test of the accuracy of meteorite analog predictions based on remote sensing and potentially advance our ability to match carbonaceous chondrites in our collections to their parent asteroids.

4.5 Conclusions

In this study, we have measured the correlated Cr and Ti isotopic compositions of three CM2 chondrites, one CO3.8 chondrite, one anomalous CM chondrite, and ten ungrouped chondrites. The implications of this work are the following:

1) Previously, there was only limited data available for both the Cr and Ti isotope compositions of bulk carbonaceous chondrites. Here we report the Cr and Ti isotopic compositions of the three CM2 chondrites and one CO3.8 chondrite that significantly extend the compositional ranges defined by the CM and CO chondrites in ε^{54}Cr vs. ε^{50}Ti space. This highlights the need for additional data to better constrain these compositional ranges.
2) The Cr and Ti isotopic compositions of the ungrouped and anomalous chondrites studied here exhibit potential genetic relationships with the CM and CO chondrites, as well as with other chondrite groups. MAC 87300 plots in the CO chondrite field, MAC 88107 plots in the CM chondrite field, LEW 85332 overlaps with the CM and CR chondrite fields, and Coolidge, EET 83355, EET 83226, MAC 87301, GRO 95566, and NWA 5958 exhibit isotopic compositions suggesting potential relationships with multiple chondrite groups. Only one sample (EET 83355) overlaps with both the CM and CO chondrite fields. These data, combined with previous O-isotope compositions, elemental abundances, and petrologic investigations, suggest that the CM, CO, and related ungrouped chondrites likely originated from distinct parent bodies that may have formed from similar precursor materials and/or in nearby formation regions in the solar protoplanetary disk.
3) The Cr and Ti isotopic compositions of two ungrouped chondrites measured here, LAP 04757 and LAP 04773, support the classification of these meteorites as low-FeO ordinary chondrites and confirm that they are unrelated to the acapulcoites. These isotopic data also provide evidence that low-FeO ordinary chondrites

originated from a distinct parent body from other ordinary chondrites, which is consistent with conclusions from previous petrologic investigations.

4) Quantitative modeling of the formation location of meteorite parent bodies has suggested that CO chondrites formed at ~3.72 AU and ~2.7 Ma after the beginning of the Solar System and CM chondrites formed ~0.04 AU farther away and ~0.8 Ma later (Desch et al., 2018). In such a scenario, the ungrouped chondrites with documented affinities to the CM and/or CO chondrites may therefore originate from distinct parent bodies which formed near ~3.72–3.76 AU and at ~2.7–3.5 Ma after the beginning of the Solar System, thus sampling precursor materials and isotopic reservoirs similar to those of the CM and CO chondrite parent bodies.
5) Initial data has shown that both Bennu and Ryugu are likely related to CM chondrites, but suggestions of potential relationships with other groups such as CI chondrites indicate that these asteroids may be related to the ungrouped chondrites studied here that show affinities to multiple chondrite groups. The samples returned from Bennu and Ryugu by the OSIRIS-REx and Hayabusa2 missions may therefore provide important insights into the origins of such meteorites.

Acknowledgements: US Antarctic meteorite samples are recovered by the Antarctic Search for Meteorites (ANSMET) program which has been funded by NSF and NASA, and characterized and curated by the Department of Mineral Sciences of the Smithsonian Institution and Astromaterials Curation Office at NASA Johnson Space Center. Thank

you to the ASU Center for Meteorite Studies for providing samples of several meteorites for this study. This work was supported by NASA grant NNH19ZDA005K to Z. T. and M. W. and NASA grant NNX15AH41G to M.W.

CHAPTER 5

SUMMARY AND FUTURE DIRECTIONS

5.1 Summary

The goal of this dissertation was to use the combination of Cr and Ti isotopes in meteorites and their components to answer outstanding questions about our Solar System. For both these isotope systems, I first developed new methods for chemical purification that improved the efficiency and reliability of existing methods to ensure consistent yields as well as precise and accurate isotopic measurements. I then used the Cr and Ti isotopic compositions that I measured in CAIs to identify the initial ingredients inherited by our Solar System from the parent molecular cloud, assess the isotopic heterogeneity present in the early Solar System, and evaluate the role of CAIs in the isotopic evolution of our Solar System. I finally used the Cr and Ti isotopic compositions of bulk CM, CO, and ungrouped chondrites to evaluate the genetic relationship between the CM and CO chondrite parent bodies and assess potential relationships between ungrouped chondrites and established chondrite groups.

As the first solids formed in our Solar System ~4.567 billion years ago (e.g., Connelly et al., 2012, 2017), CAIs record a snapshot of the earliest stage of Solar System formation and their isotopic compositions provide clues to their role in the subsequent preservation of planetary-scale isotopic anomalies. Although CAIs from several chondrite groups had been measured previously for their Ti isotopic compositions, CAIs from only two meteorites had been measured for their Cr isotopic compositions and only a handful of CAIs had been measured for both their Cr and Ti isotopic compositions prior to this

dissertation work. This work is therefore an important step towards defining the range of Cr and Ti isotopic anomalies in the same CAIs from a variety of carbonaceous chondrites, which in turn provides constraints on the isotopic heterogeneity of the early Solar System and the role of CAIs in the planetary-scale isotopic dichotomy in the early Solar System.

The Cr and Ti isotopic compositions of CAIs of diverse petrologic and geochemical types from a variety of carbonaceous chondrites were measured with the goal of ascertaining whether previously reported isotopic compositions of CAIs from a limited number of meteorites were representative of the broader CAI-forming region. The observed variation in both ε^{50}Ti and ε^{54}Cr values of the CAIs measured here likely results from a combination of isotopic heterogeneity inherited during infall from the parent molecular cloud, heterogeneous carrier phase distribution, and thermal processing in the disk. Median ε^{50}Ti and ε^{54}Cr values for these CAIs are similar to those reported previously in the literature for CAIs from CV, CK, CM, CO, and ordinary chondrites for ε^{50}Ti and from CV chondrites for ε^{54}Cr, suggesting that all CAIs formed from a common isotopic reservoir characterized by some isotopic variability. A strong correlation exists between ε^{46}Ti and ε^{50}Ti for Solar System materials including CAIs and likely represents the mixing between a ^{46}Ti- and ^{50}Ti-poor reservoir and a ^{46}Ti- and ^{50}Ti-rich reservoir. Because of the distinct nucleosynthetic sources of these isotopes, the reservoir enriched in both ^{46}Ti and ^{50}Ti must itself have resulted from the mixing of materials from two distinct reservoirs. Therefore, these data show that materials from at least three distinct nucleosynthetic sources were present in the CAI-forming region. While most CAIs

studied here fall on this correlation line, some do not and may record intermediate stages of mixing.

The offset of the carbonaceous chondritic (CC) isotopic reservoir from the non-carbonaceous chondritic (NC) isotopic reservoir towards the isotopic composition of CAIs in ε^{50}Ti vs. ε^{54}Cr space cannot be solely caused by transport of CAIs from the NC to the CC region or the thermal processing of isotopically anomalous components within the disk. Instead, the observed ε^{50}Ti and ε^{54}Cr isotopic compositions of CAIs are consistent with models in which CAIs record the isotopic composition of early infalling material inherited by the solar protoplanetary disk from the parent molecular cloud; in such models, the composition of the CC region represents that of early infalling material that underwent some mixing with the later infalling material that characterizes the NC region (e.g., Nanne et al., 2019). However, the transport of CAIs to the CC region and thermal processing in the disk may additionally contribute to the range of ε^{50}Ti and ε^{54}Cr compositions observed in bulk carbonaceous chondrites.

The Cr and Ti isotopic compositions of the bulk CM, CO, and ungrouped chondrites were acquired with the goal of providing additional constraints on the relationship between CM and CO chondrites and assessing potential genetic relationships between ungrouped chondrites and established chondrite groups. Limited Cr and Ti isotopic data existed for CM and CO chondrites prior to this dissertation work, and isotopic data of potentially related ungrouped chondrites were primarily limited to oxygen isotope compositions. The three CM2 chondrites and one CO3.8 chondrite studied here extend the CM and CO chondrite compositional fields in ε^{54}Cr vs. ε^{50}Ti space. The ungrouped and anomalous chondrites analyzed here exhibit potential genetic

relationships with CM and CO chondrites in ε^{50}Ti vs. ε^{54}Cr space, as well as with other chondrite groups. These data, combined with previous oxygen isotope compositions, elemental abundances, and petrologic investigations, suggest that the CM, CO, and related ungrouped chondrites likely originated from distinct parent bodies that formed from isotopically similar precursor materials in similar formation regions. Using the quantitatively modeled formation regions of Desch et al. (2018), these distinct parent bodies may have formed near ~3.72–3.76 AU around ~2.7–3.5 Ma after CAI formation. The asteroids Bennu and Ryugu are likely related to CM and/or CI chondrites based on spectral analyses, but uncertainties in these matches raises the possibility that they may be similar to ungrouped chondrites that show affinities with these carbonaceous chondrite groups. The samples returned from Bennu and Ryugu by the OSIRIS-REx and Hayabusa2 missions may therefore provide insights into the origins of such meteorites.

The Cr and Ti isotopic analyses reported in this dissertation provide important new constraints on the earliest stages of Solar System formation and genetic relationships between meteorite bodies. The analytical development conducted during this work provides improved methods for the efficient and reliable acquisition of precise and accurate isotopic data. Additionally, new knowledge gained during this work has prompted new questions to be investigated by future studies. These potential topics for future investigations are discussed in the following sections.

5.2 Future Directions

The work in this dissertation naturally points to the need for additional analyses of the type reported here. The compositional fields of the carbonaceous chondrite groups in

ε^{50}Ti vs. ε^{54}Cr space are defined by limited data points that often represent measurements of separate aliquots of individual meteorites or in some cases different meteorites altogether. The combination of limited data, close proximity of existing compositional fields, and overlapping fields of certain groups highlight the need for additional data. While new data for three CM chondrites and one CO chondrite are provided in this dissertation, the fact that these limited new data were sufficient to significantly redefine the boundaries of the compositional fields for these two chondrite groups illustrates the need for additional data. Further constraints on the compositional fields of the carbonaceous chondrite groups in ε^{50}Ti vs. ε^{54}Cr space from such additional data would enable more accurate assessments of potential genetic relationships between samples using these isotopic compositions. For future studies of Cr and Ti isotopic data for bulk carbonaceous chondrites, it will be imperative to analyze representative bulk samples of the selected meteorites. As discussed in this dissertation, non-representative sampling (particularly of isotopically anomalous components) could have a significant effect on the measured isotopic compositions and would complicate the use of these data for interpreting genetic relationships. It will also be important to conduct repeat measurements of separate aliquots of individual meteorites to more rigorously assess the degree of isotopic heterogeneity present within individual carbonaceous chondrites.

In the following I have identified some next steps that would build upon this dissertation work. These include: 1) Identifying the carrier phases of isotopic anomalies in meteorites; 2) Determining the relative ages of refractory inclusions and correlating these with their isotopic anomalies; and 3) Utilizing meteoritic data in combination with

astrophysical modeling. In the following sections, I discuss each of these next steps and their potential implications for Solar System origin and evolution.

5.2.1 Identifying the Carrier Phases of Isotopic Anomalies in Meteorites

An important step forward in the understanding of isotopic anomalies in meteorites and their components is the identification of the carrier phases of these anomalies. Previous studies have identified sub-micron spinel grains as the likely carriers of Cr isotopic anomalies (Dauphas et al., 2010; Qin et al., 2011), and perovskite has been suggested as a potential carrier of Ti isotopic anomalies because of its highly refractory nature and stoichiometry consistent with correlations between Ti and Ca isotopic anomalies (Dauphas et al., 2014). The confirmation of these carrier phases for Cr and Ti isotopic anomalies, identification of the carrier phases of other isotopic anomalies, and quantification of the distribution of these phases in CAIs and other meteoritic components will be crucial for advancing our understanding of the origin of these isotopic anomalies. If isotopically anomalous carrier phases were heterogeneously distributed in CAIs or CAI precursor material, or were affected to varying degrees by disk processing, this could be a significant contributor to the observed isotopic variability observed in CAIs. Therefore, the identification of these carrier phases will be crucial for our understanding of the relative contributions of inherited heterogeneity during infall from the molecular cloud, heterogeneous carrier phase distribution, and thermal processing in the protoplanetary disk to such isotopic variability. Such identification and characterization may be aided by improvements in the spatial resolution and useful yield capabilities of in situ analytical techniques for isotopic analyses such as nanoscale

secondary ion mass spectrometry (NanoSIMS) (e.g., Hoppe et al., 2013) and resonance ionization mass spectrometry (RIMS) (e.g., Stephan et al., 2016).

5.2.2 Determining the Relative Ages of Refractory Inclusions and Correlating these with Their Isotopic Anomalies

The absolute age of CAIs has been determined to be ~4.567 billion years (e.g., Amelin et al., 2010; Bouvier and Wadhwa, 2010; Connelly et al., 2012, 2017). Studies of the Al–Mg systematics in CAIs suggest that the formation time interval for these refractory inclusions was less than 200,000 years (Jacobsen et al., 2008; MacPherson et al., 2012; Kawasaki et al. 2019; Liu et al., 2019). No studies, however, have combined the chronological investigations with measurements of isotopic anomalies in the same CAIs, and such work would provide important constraints on the origin of isotopic anomalies in CAIs. According the model of Burkhardt et al. (2019) and Nanne et al. (2019), the earliest-formed solids sampled the infalling material from the molecular cloud that preserved the largest enrichments in supernova-derived nuclides. Therefore, a prediction of such a model is that the earliest-formed CAIs would preserve larger isotopic anomalies than those that formed later. If the opposite trend is observed, and the magnitude of isotopic anomalies is larger in later-formed CAIs, this would suggest that processing within the disk played a larger role in producing the isotopic anomalies than heterogeneity in the infalling material. It is also possible that no clear trend is observed, which could indicate that the formation timescale of CAIs is too short to record an observable correlation or that spatial heterogeneity played a larger role than temporal heterogeneity. It will also be useful to expand such correlated investigations of

chronology and isotopic anomalies to include additional isotope systems (including those of refractory and non-refractory elements) to ascertain whether different isotope systems show similar or different behavior. This in turn may provide constraints on whether thermal processing was important in producing isotopic variability in the protoplanetary disk.

5.2.3 Utilizing Meteoritic Data in Combination with Astrophysical Modeling

The science of the early Solar System sits at the junction of the disciplines such as astrophysics, planetary science, and cosmochemistry, and any critical evaluation of models of Solar System formation and evolution will therefore be strongest when taking an interdisciplinary approach. To do so, astrophysical models must be tested by meteoritic and cosmochemical data and interpretations of meteoritic data must in turn be supplemented by astrophysical models. This will ensure that models are constrained by physical data and the interpretations of such data are consistent with the astrophysical understanding of Solar System formation and evolution. Recent studies characterizing the isotopic dichotomy in the early Solar System are based on isotopic data from meteorites (e.g., Kruijer et al., 2017; Burkhardt et al., 2019; Nanne et al., 2019). The data from these studies can be interpreted in the context of previous astrophysical models (e.g., Ciesla et al., 2010; Yang and Ciesla, 2012) to provide a better understanding of the astrophysical environment in which our Solar System formed and evolved. Additional recent studies have sought to combine cosmochemistry and astrophysical modeling to aid our understanding of early Solar System dynamics and the formation regions of meteorite parent bodies (e.g., Desch et al., 2018; Jacquet et al., 2019). Together, such studies

demonstrate the power of combining meteoritic data and astrophysical modeling. As current and future studies continue to evaluate important questions about our early Solar System, it will be critical to continue to take an interdisciplinary approach to answering these questions.

REFERENCES

Abreu N. M., Louro M. D., Friedrich J. M., Schrader D. L., and Greenwood R. C. (2018) Elephant Moraine (EET) 93226: A clastic, type 2 carbonaceous chondrite with affinities to the CO chondrites. *Lunar Planet. Sci. 49* (Abstract #2451).

Akram W., Schönbächler M., Sprung P. and Vogel N. (2013) Zirconium–Hafnium isotope evidence from meteorites for the decoupled synthesis of light and heavy neutron-rich nuclei. *Astrophys. J.* **777**, 169–180.

Alexander C. M. O'D. and Nittler L. R. (1999) The galactic evolution of Si, Ti, and O isotopic ratios. *Astrophys. J.* **519**, 222–235.

Alexander C. M. O. D., Howard K. T., Bowden R. and Fogel M. L. (2013) The classification of CM and CR chondrites using bulk H, C and N abundances and isotopic compositions. *Geochim. Cosmochim. Acta* **123**, 244–260.

Alexander C. M. O. D., Bowden R., Fogel M. L. and Howard K. T. (2015) Carbonate abundances and isotopic compositions in chondrites. *Meteorit. Planet. Sci.* **50**, 810–833.

Alexander C. M. O. D. and Bowden R. (2018) Lewis Cliff (LEW) 85332 and Miller Range (MIL) 090001, a new grouplet that is distinct from the CR chondrites? *81st Meeting of the Meteoritical Society* (Abstract #2067).

Alexander C. M. O. D. (2019) Quantitative models for the elemental and isotopic fractionations in the chondrites: The carbonaceous chondrites. *Geochim. Cosmochim. Acta* **254**, 277–309.

Amari S., Nittler L. R., Zinner E., Gallino R., Lugaro M. and Lewis R. S. (2001a) Presolar SiC grains of type Y: origin from low-metallicity asymptotic giant branch stars. *Astrophys. J.* **546**, 248–266.

Amari S., Nittler L. R., Zinner E., Lodders K. and Lewis R. S. (2001b) Presolar SiC grains of type A and B: their isotopic compositions and stellar origins. *Astrophys. J.* **559**, 463–483.

Amelin Y., Krot A. N., Hutcheon I. D., Ulyanov A.A. (2002) Lead isotopic ages of chondrules and calcium-aluminum-rich inclusions. *Science* **297**, 1678–1683.

Amelin Y., Connelly J., Zartman R.E., Chen J.H., Gopel C., Neymark L.A. (2009) Modern U– Pb chronometry of meteorites: advancing to higher time resolution reveals new problems. *Geochim. Cosmochim. Acta* **73**, 5212–5223.

Amelin Y., Kaltenbach A., Iizuka T., Stirling C. H., Ireland T. R., Petaev M. and Jacobsen S. B. (2010) U-Pb chronology of the Solar System's oldest solids with variable 238U/235U. *Earth Planet. Sci. Lett.* **300**, 343–350.

Arnold G. L., Weyer S. and Anbar A. D. (2004) Fe Isotope Variations in Natural Materials Measured Using High Mass Resolution Multiple Collector ICPMS. *Anal. Chem.* **76**, 322–327.

Birck J. L. and Allègre C. J. (1984) Chromium isotopic anomalies in Allende Refractory Inclusions. *Geophys. Res. Lett.* **11**, 943–946.

Birck J. L. and Allègre C. J. (1985) Evidence for the presence of ^{53}Mn in the early solar system. *Geophys. Res. Lett.* **12**, 745–748.

Birck J. L. and Lugmair G. W. (1988) Nickel and chromium isotopes in Allende inclusions. *Earth Planet. Sci. Lett.* **90**, 131–143.

Bizzarro M., Baker J., and Haack H. (2004) Mg isotope evidence for contemporaneous formation of chondrules and refractory inclusions. *Nature* **431**, 275-278.

Boss A. P. (1998) Temperature in protoplanetary disks. *Annual Review of Earth and Planetary Sciences* **26**, 53–80.

Bouvier, A., Brennecka, G.B., and Wadhwa M. (2011) Absolute Chronology of the First Solids in the Solar System. *Work. Form. First Solids Sol. Syst.* #9054.

Boynton W. V. (1975) Fractionation in the solar nebula: condensation of yttrium and the rare earth elements. *Geochim. Cosmochim. Acta* **39**, 569–584.

Brearley A. J. (1997) Phyllosilicates in the matrix of the unique carbonaceous chondrite, LEW 85332 and possible implications for the aqueous alteration of CI chondrites. *Meteorit. Planet. Sci.* **32**, 377–388.

Brennecka G. A., Weyer S., Wadhwa M., Janney P. E., Zipfel J. and Anbar A. D. (2010) ^{238}U/^{235}U Variations in Meteorites: Extant ^{247}Cm and Implications for Pb-Pb Dating. *Science* **327**, 449–451.

Brennecka G. A., Borg L. E. and Wadhwa M. (2013) Evidence for supernova injection into the solar nebula and the decoupling of r-process nucleosynthesis. *Proc. Natl. Acad. Sci. U. S. A.* **110**, 17241–17246.

Brennecka G. A., Borg L. E., Romaniello S. J., Souders A. K., Shollenberger Q. R., Marks N. E. and Wadhwa M. (2017) A renewed search for short-lived ^{126}Sn in the early Solar System: Hydride generation MC-ICPMS for high sensitivity Te isotopic analysis. *Geochim. Cosmochim. Acta* **201**, 331–344.

Brennecka, G. A., Burkhardt, C., Budde, G., Kruijer, T. S., Nimmo, F., Kleine, T. (submitted) An astronomical framework for Solar System formation from Mo isotopes in refractory inclusions. *Science*.

Budde G., Burkhardt C., Brennecka G. A., Fischer-gödde M., Kruijer T. S. and Kleine T. (2016) Molybdenum isotopic evidence for the origin of chondrules and a distinct genetic heritage of carbonaceous and non-carbonaceous meteorites. *Earth Planet. Sci. Lett.* **454**, 293–303.

Burkhardt C., Kleine T., Oberli F., Pack A., Bourdon B. and Wieler R. (2011) Molybdenum isotope anomalies in meteorites: Constraints on solar nebula evolution and origin of the Earth. *Earth Planet. Sci. Lett.* **312**, 390–400.

Burkhardt C., Dauphas N., Hans U., Bourdon B. and Kleine T. (2019) Elemental and isotopic variability in solar system materials by mixing and processing of primordial disk reservoirs. *Geochim. Cosmochim. Acta* **261**, 145–170.

Cameron A.G.W. and Truran J.W. (1977) The supernova trigger for formation of the Solar System. *Icarus* **30**, 447–461.

Chen H., Lee T., Lee D. and Iizuka Y. (2009) In Situ Ti Isotopic Measurements by Laser Ablation MC-ICP-MS. *Terr. Atmos. Ocean. Sci.* **20**, 703–712.

Choe W. H., Huber H., Rubin A. E., Kallemeyn G. W., Wasson J. T. (2010) Compositions and taxonomy of 15 unusual carbonaceous chondrites. *Meteorit. Planet. Sci.* **45**, 531–554.

Ciesla F. J. (2010) The distributions and ages of refractory objects in the solar nebula. *Icarus* **208**, 455–467.

Cieza L., Padgett D. L., Staplefeldt K. R., Augereau, J.-C, Harvey, P., Evans N. J., Merín B., Koerner, D., Sargent A., van Dishoeck E. F., Allen L., Blake G., Brooke T., Chapman N., Huard T., Lai S.-P, Mundy L., Myers P. C., Spiesman W., Wahhaj Z. (2007) The Spitzer c2d Survey of Weak-Line T Tauri Stars. II. New Constraints on the Timescale for Planet Building. *Astrophys. J.* **667**, 308–328.

Clayton R. N., Grossman L., and Mayeda K. (1973) A component of primitive nuclear composition in carbonaceous meteorites. *Science* **182**, 485–488.

Clayton R. N. and Mayeda T.K. (1977) Correlated oxygen and magnesium isotope anomalies in Allende Inclusions, I: Oxygen. *Geophysical Research Letters* **4**, 295–298.

Clayton R. N. and Mayeda T. K. (1999) Oxygen isotope studies of carbonaceous chondrites. *Geochim. Cosmochim. Acta* **63**, 2089–2104.

Clayton D. D. (2003) Handbook of Isotopes in the Cosmos. *Cambridge University Press, Cambridge*.

Connelly J. N., Bizzarro M., Krot A. N., Nordlund A., Wielandt D. and Ivanova M. A. (2012) The Absolute Chronology and Thermal Processing of Solids in the Solar Protoplanetary Disk. *Science* **338**, 651–655.

Connelly J. N., Bollard J. and Bizzarro M. (2017) Pb–Pb chronometry and the early Solar System. *Geochim. Cosmochim. Acta* **201**, 345–363.

Dauphas N., Marty B. and Reisberg L. (2002) Molybdenum Nucleosynthetic Dichotomy Revealed in Primitive Meteorites. *Astrophys. J.* **569**, L139–L142.

Dauphas N., Remusat L., Chen J. H., Roskosz M., Papanastassiou D. A., Stodolna J., Guan Y., Ma C. and Eiler J. M. (2010) Neutron-Rich Chromium Isotope Anomalies in Supernova Nanoparticles. *Astrophys. J.* **720**, 1577–1591.

Dauphas N. and Chaussidon M. (2011) A Perspective from Extinct Radionuclides on a Young Stellar Object: The Sun and Its Accretion Disk. *Annu. Rev. Earth Planet. Sci.* **39**, 351–386.

Dauphas N. and Schauble E. A. (2016) Mass Fractionation Laws, Mass-Independent Effects, and Isotopic Anomalies. *Annu. Rev. Earth Planet. Sci* **44**, 709–83.

Davis A. M. and Grossman L. (1979) Condensation and fractionation of rare earths in the solar nebula. *Geochim. Cosmochim. Acta* **43**, 1611–1632.

Davis A. M., Zhang J., Greber N. D., Hu J., Tissot, F. L. H., Dauphas, N. (2018) Titanium isotopes and rare earth patterns in CAIs: Evidence for thermal processing and gas-dust decoupling in the protoplanetary disk. *Geochim. Cosmochim. Acta* **221**, 275–295.

De Leuw S., Rubin A. E., Schmitt A. K. and Wasson J. T. (2009) ^{53}Mn–^{53}Cr systematics of carbonates in CM chondrites: implications for the timing and duration of aqueous alteration. *Geochim. Cosmochim. Acta* **73**, 7433–7442.

Desch S., Kalyaan A. and Alexander C. M. O. D. (2018) The Effect of Jupiter's Formation on the Distribution of Refractory Elements and Inclusions in Meteorites. *Astrophys. J. Suppl. Ser.* **238**, 31 pp.

Doyle P. M., Krot A. N., and Nagashima K. (2013) Oxygen-isotopes of fayalite, magnetite and chondrule olivne in the CO (Y-81020, EET 90043) and CO-like (MAC 88107) chondrites. *76th Meeting of the Meteoritical Society* (Abstract #5135).

Ebert S., Render J., Brennecka G. A., Burkhardt C., Bischoff A., Gerber S. and Kleine T. (2018) Ti isotopic evidence for a non-CAI refractory component in the inner Solar System. *Earth Planet. Sci. Lett.* **498**, 257–265.

Emery J. P., Fernández Y. R., Kelley M. S. P., Warden (ne`e Crane) K. T., Hergenrother C., Lauretta D. S., Drake M. J., Campins H. and Ziffer J. (2014) Thermal infrared observations and thermophysical characterization of OSIRIS-Rex target asteroid (101955) Bennu. *Icarus* **234**, 17–35.

Eugster O. (2003) Cosmic-ray exposure ages of meteorites and Lunar rocks and their significance. *Chem. Erde* **63**, 3–30.

Evans N. J., II, Dunham M. M., Jørgensen J. K., Enoch M. L., Merín B., van Dishoeck E. F., Alcalá J. M., Myers P. C., Stapelfeldt K. R., Huard T. L., Allen L. E., Harvey P. M., van Kempen T., Blake G. A., Koerner D. W., Mundy L. G., Padgett D. L., and Sargent A. I. (2009) The Spitzer c2d Legacy results: Star-formation rates and efficiencies; evolution and lifetimes. *The Astrophysical Journal Supplement Series* **181**, 321–350.

Fahey A. J., Goswami J. N., McKeegan K. D. and Zinner E. (1987) ^{26}Al, ^{244}Pu, ^{50}Ti, REE, and trace element abundances in hibonite grains from CM and CV meteorites. *Geochim. Cosmochim. Acta* **51**, 329–350.

Frank D. R., Zolensky M. E. and Le L. (2014) Olivine in terminal particles of Stardust aerogel tracks and analogous grain in chondrite matrix. *Geochim. Cosmochim. Acta* **142**, 240–259.

Friedrich J. M., Weisberg M. K., Ebel D. S., Biltz A. E., Corbett B. M., Iotzov I. V., Khan W. S. and Wolman M. D. (2015) Chondrule size and related physical properties: A compilation and evaluation of current data across all meteorite groups. *Chemie der Erde* **75**, 419–443.

Fujiya W., Sugiura N., Sano Y. and Hiyagon H. (2013) Mn–Cr ages of dolomites in CI chondrites and the Tagish Lake ungrouped carbonaceous chondrite. *Earth Planet. Sci. Lett.* 362, 130–142.

Garenne A., Beck P., Montes-Hernandez G., Chiriac R., Toche F., Quirico E., Bonal L, Schmitt B. (2014) The abundance and stability of "water" in type 1 and 2 carbonaceous chondrites (CI, CM and CR). *Geochim. Cosmochim. Acta* **137**, 93–112.

Gattacceca J. (2019) The Meteoritical Bulletin, No 108. *Meteoritics.*

Gerber S., Burkhardt C., Budde G., Metzler K. and Kleine T. (2017) Mixing and transport of dust in the early solar nebula as inferred from titanium isotope variations among chondrules. *Astrophys. J.* **841**, L17–L23.

Göpel C., Birck J. L., Galy A., Barrat J,-A., and Zanda B. (2015) Mn-Cr systematics in primitive meteorites: insights from mineral separation and partial dissolution. *Geochim. Cosmochim. Acta* **156**, 1–24.

Greenwood R. C., Howard K. T., Franchi I. A., Zolensky M. E., Buchanan P. C., and Gibson J. M. (2014) Oxygen isotope evidence for the relationship between CM and CO chondrites: Could they both coexist on a single asteroid? *Lunar Planet. Sci. 45* (Abstract #2610).

Greenwood R. C., Howard K. T., King A. J., Lee M. R., Burbine T. H., Franchi, I. A., Anand, M., Findlay, R., and Gibson, J. M. (2019) Oxygen isotope evidence for multiple CM parent bodies: What will we learn from the Hayabusa2 and OSIRIS-REx sample return missions? *Lunar Planet. Sci. 50* (Abstract #3191).

Grossman J. N. (1994) The Meteoritical Bulletin, No 76, 1994 January: the US Antarctic meteorite collection. *Meteoritics* 29, 100–143.

Guan Y., McKeegan K. D., MacPherson G. J. (2000a) Oxygen isotopes in calcium-aluminum-rich inclusions from enstatite chondrites: new evidence for a single CAI source in the solar nebula. *Earth Planet. Sci. Lett.* **181**, 271–277.

Guan Y., Huss, G. R., MacPherson, G. J., Wasserburg, G. J. (2000b) Calcium-aluminum-rich inclusions from enstatite chondrites: indigenous or foreign? *Science* **289**, 1330–1333.

Gyngard F., Amari S., Zinner E. and Marhas K. K. (2018) Correlated silicon and titanium isotopic compositions of presolar SiC grains from the Murchison CM2 chondrite. *Geochim. Cosmochim. Acta* **221**, 145–161.

Hamilton V., Simon A., Christensen P., Reuter D., Clark B., Barucci A., Bowles N., Boynton W., Brucato J., Cloutis E., Connolly Jr. H., Donaldson Hanna K., Emery J., Enos H., Fornasier S., Haberle C., Hanna R., Howell E., Kaplan H., Keller L., Lantz C., Li J.-Y., Lim L., McCoy T., Merlin F., Nolan M., Praet A., Rozitis B., Sandford S., Schrader D. L.**,** Thomas C., Zou X.-D., Lauretta D., and the OSIRIS-REx Team. (2019) Evidence for widespread hydrated minerals on asteroid (101955) Bennu. *Nature Astronomy* **3**, 332–340.

Hasegawa S., Müller T. G., Kawakami K., Kasuga T., Wada T., Ita Y., Takato N., Terada H., Fujiyoshi T. and Abe M. (2008) Albedo, size, surface characteristics of Hayabusa-2 sample- return target 162173 1999 JU3 from AKARI and Subaru observations. *Publ. Astron. Soc. Japan* **60**, S399–S405.

Hewins R. H., Bourot-Denise M., Zanda B., Leroux H., Barrat J.- A., Humayun M., Gopël C., Greenwood R. C., Franchi I. A., Pont S., Lorand J.-P., Cournéde C., Gattacceca J., Rochette P., Kuga M., Marrocchi Y. and Marty B. (2014) The Paris meteorite, the least altered CM chondrite so far. *Geochim. Cosmochim. Acta* **124**, 190–222.

Heydegger H. R., Foster J. J. and Compston W. (1979) Evidence of a new isotopic anomaly from titanium isotopic ratios in meteoric materials. *Nature* **278**, 704–707.

Hinton R. W., Davis A. M. and Scatena-Wachel D. E. (1987) Large negative ^{50}Ti anomalies in refractory inclusions from the Murchison carbonaceous chondrite: evidence for incomplete mixing of neutron-rich supernova ejecta into the solar system. *Astrophys. J.* **313**, 420–428.

Hiroi T., Zolensky M. I., Pieters C.M. (1997) Characterization of Unusual CI/CM/CR Meteorites from Reflectance Spectroscopy. *Lunar Planet. Sci. 28* (Abstract #1463).

Hoppe P., Amari S., Zinner E., Ireland T. and Lewis R. S. (1994) Carbon, nitrogen, magnesium, silicon, and titanium isotopic compositions of single interstellar silicon carbide grains from the Murchison carbonaceous chondrite. *Astrophys. J.* **430**, 870–890.

Hoppe P., Cohen S. and Meibom A. (2013) NanoSIMS: Technical Aspects and Applications in Cosmochemistry and Biological Geochemistry. *Geostand. Geoanal. Res* **37**, 111–154.

Huang S., Farkaš J., Yu G., Petaev M. I. and Jacobsen S. B. (2012) Calcium isotopic ratios and rare earth element abundances in refractory inclusions from the Allende CV3 chondrite. *Geochim. Cosmochim. Acta* **77**, 252–265.

Huss G. R. and Smith J. B. (2007) Titanium isotopic compositions of well-characterized silicon carbide grains from Orgueil (CI): implications for s-process nucleosynthesis. *Meteorit. Planet. Sci.* **42**, 1055–1075.

Ireland T. R. (1988) Correlated morphological, chemical, and isotopic characteristics of hibonites from the Murchison carbonaceous chondrite. *Geochim. Cosmochim. Acta* **52**, 2827–2839.

Ireland T. R. (1990) Presolar isotopic and chemical signatures in hibonite-bearing refractory inclusions from the Murchison carbonaceous chondrite. *Geochim. Cosmochim. Acta* **54**, 3219–3237.

Ireland T. R., Zinner E. K. and Amari S. (1991) Isotopically anomalous Ti in presolar SiC from the Murchison meteorite. **376**, L53–L56.

Jacobsen B., Yin Q., Moynier F., Amelin Y., Krot A. N., Nagashima K., Hutcheon I. D. and Palme H. (2008) ^{26}Al-^{26}Mg and ^{207}Pb-^{206}Pb systematics of Allende CAIs: canonical solar initial ^{26}Al/^{27}Al ratio reinstated. *Geochim. Cosmochim. Acta* **272**, 353–364.

Jacquet E., Barrat J.-A., Beck P., Caste F., Gattacceca J., Sonzogni C. and Gounelle M. (2016) Northwest Africa 5958: A weakly altered CM-related ungrouped chondrite, not a CI3. *Meteorit. Planet. Sci.* ***51****, 851–869.*

Jacquet E., Pignatale F. C., Chaussidon M. and Charnoz S. (2019) Fingerprints of the Protosolar Cloud Collapse in the Solar System. II. Nucleosynthetic Anomalies in Meteorites. *Astrophys. J.* **884**, 32, 11 pp.

Jilly C. E., Huss G. R., Krot A. N., Nagashima K., Yin Q.-Z., Sugiura N. (2014) ^{53}Mn–^{53}Cr dating of aqueously formed carbonates in the CM2 lithology of the Sutter's Mill carbonaceous chondrite. *Meteorit. Planet. Sci.* **49**, 2104–2117.

Jungck M. H. A., Shimamura T. and Lugmair G. W. (1984) Ca isotope variations in Allende. *Geochim. Cosmochim. Acta* **48**, 2651–2658.

Kallemeyn G. W. and Wasson J. T. (1981) The compositional classification of chondrites – I. The carbonaceous groups. *Geochim. Cosmochim. Acta* **45**, 1217–1230.

Kallemeyn G. W., Wasson J. T. (1982) The compositional classification of chondrites: III. Ungrouped carbonaceous chondrites. *Geochim. Cosmochim. Acta* **46**, 2217–2228.

Kallemeyn G. W. (1992) Three Ungrouped Carbonaceous Chondrites from MacAlpine Hills, Antarctica. *Lunar Planet. Sci. 23* (Abstract #649).

Kallemeyn G.W., Rubin A.E., Wasson J.T. (1994) The compositional classification of chondrites: VI. The CR chondrite group. *Geochim. Cosmochim. Acta* **58**, 2873–2888.

Kallemeyn G. W., Rubin A. E. (1995) Coolidge and Loongana 001: a new carbonaceous chondrite grouplet. *Meteoritics* **30**, 20–27.

Kawasaki N., Park C., Sakamoto N., Park S. Y., Kim H. N., Kuroda M. and Yurimoto H. (2019) Variations in initial ^{26}Al/^{27}Al ratios among fluffy Type A Ca–Al-rich inclusions from reduced CV chondrites. *Earth Planet. Sci. Lett.* **511**, 25–35.

Kita N. T., Yin Q. Z., Macpherson G. J., Ushikubo T., Jacobsen B., Nagashima K., Kurahashi E., Krot A. N. and Jacobsen S. B. (2013) ^{26}Al-^{26}Mg isotope systematics of the first solids in the early solar system. *Meteorit. Planet. Sci.* **48**, 1383–1400.

Kitazato K., Milliken R. E., Iwata T., et al. (2019) The surface composition of asteroid 162173 Ryugu from Hayabusa2 near-infrared spectroscopy. *Science* **364**, 272–275.

Kööp L., Nakashima D., Heck P. R., Kita N. T., Tenner T. J., Krot A. N., Nagashima K., Park C. and Davis A. M. (2016a) New constraints on the relationship between ^{26}Al and oxygen, calcium, and titanium isotopic variation in the early Solar System from a multielement isotopic study of spinel-hibonite inclusions. *Geochim. Cosmochim. Acta* **184**, 151–172.

Kööp L., Davis A. M., Nakashima D., Park C., Krot A. N., Nagashima K., Tenner T. J., Heck P. R. and Kita N. T. (2016b) A link between oxygen, calcium and titanium isotopes in ^{26}Al-poor hibonite-rich CAIs from Murchison and implications for the heterogeneity of dust reservoirs in the solar nebula. *Geochim. Cosmochim. Acta* **189** (70–95).

Kööp L., Nakashima D., Heck P. R., Kita N. T., Tenner T. J., Krot A. N., Nagashima K., Park C. and Davis A. M. (2018) A multielement isotopic study of refractory FUN and F CAIs: Mass-dependent and mass-independent isotope effects. *Geochim. Cosmochim. Acta* **221**, 296–317.

Kööp L., Nagashima K., Kööp L., Nagashima K., Davis A. M. and Krot A. N. (2020) A refractory inclusion with solar oxygen isotopes and the rarity of such objects in the meteorite record. *Meteorit. Planet. Sci.* 1–11.

Krot A. N., Petaev M. I., Scott E. R. D., Choi B.-G., Zolensky M. E. and Keil K. (1998) Progressive alteration in CV3 chondrites: more evidence for asteroidal alteration. *Meteorit. Planet. Sci.* **33**, 748–775.

Krot A. N., Nagashima K., Ciesla F. J., Meyer B. S., Hutcheon I. D., Davis A. M., Huss G. R. and Scott E. R. D. (2010) Oxygen isotopic composition of the Sun and mean oxygen isotopic composition of the protosolar silicate dust: Evidence from refractory inclusions. *Astrophys. J.* **713**, 1159–1166.

Krot A. N. and Nagashima K. (2012) Oxygen-Isotope Systematics of the Fayalite-Bearing Assemblages in MAC 88107, CO-Like Carbonaceous Chondrite. *75th Meeting of the Meteoritical Society* (Abstract #5338).

Krot A. N., Keil K., Scott E. R. D., Goodrich C. A. and Weisberg M. K. (2013) Classification of Meteorites and Their Genetic Relationships. Vol. 1 *Treatise on Geochemistry*, 2nd ed. (Exec. Eds. H. D. Holland and K. K. Turekian), Elsevier, Oxford, 1–63.

Kruijer T. S., Kleine T., Fischer-Gödde M., Burkhardt C. and Wieler R. (2014) Nucleosynthetic W isotope anomalies and the Hf-W chronometry of Ca-Al-rich inclusions. *Earth Planet. Sci. Lett.* **403**, 317–327.

Kruijer T. S., Burkhardt C., Budde G. and Kleine T. (2017) Age of Jupiter inferred from the distinct genetics and formation times of meteorites. *Proc. Natl. Acad. Sci.* **114**, 6712–6716.

Kurahashi E., Kita N. T., Nagahara H. and Morishita Y. (2008) ^{26}Al–^{26}Mg systematics of chondrules in a primitive CO chondrite. *Geochim. Cosmochim. Acta* **72**, 3865–3882.

Larsen K. K., Wielandt D., Schiller M. and Bizzarro M. (2016) Chromatographic speciation of Cr(III)-species, inter-species equilibrium isotope fractionation and improved chemical purification strategies for high-precision isotope analysis. *J. Chromatogr. A* **1443**, 162–174.

Lauretta D. S., DellaGiustina D. N., Bennett C. A., et al. (2019) The unexpected surface of asteroid (101955) Bennu. *Nature* **568**, 55–60.

Lee M. R., Lindgren P., Sofe M. R., Alexander C. M. O' and Wang J. (2012) Extended chronologies of aqueous alteration in the CM2 carbonaceous chondrites: evidence from carbonates in Queen Alexandria Range 93005. *Geochim. Cosmochim. Acta* **92**, 148–169.

Leya I., Schönbächler M., Wiechert U., Krähenbühl U. and Halliday A. N. (2007) High precision titanium isotope measurements on geological samples by high resolution MC-ICPMS. *Int. J. Mass Spectrom.* **262**, 247–255.

Leya I., Schönbächler M., Krähenbühl U. and Halliday A. N. (2009) New titanium isotope data for Allende and Efremovka CAIs. *Astrophys. J.* **702**, 1118–1126.

Liu M.-C., McKeegan K. D., Goswami J. N., Marhas K. K., Sahijpal S., Ireland T. R. and Davis A. M. (2009) Isotopic records in CM hibonites: implications for timescales of mixing of isotope reservoirs in the solar nebula. *Geochim. Cosmochim. Acta* **73**, 5051–5079.

Liu M. C., Chaussidon M., Göpel C. and Lee T. (2012) A heterogeneous solar nebula as sampled by CM hibonite grains. *Earth Planet. Sci. Lett.* **327**–**328**, 75–83.

Liu M. C., Han J., Brearley A. J. and Hertwig A. T. (2019) Aluminum-26 chronology of dust coagulation and early solar system evolution. *Sci. Adv.* **5**, 1–9.

Lodders K. (2003) Solar System abundances and condensation temperatures of the elements. *Astrophys. J.* **591**, 1220–1247.

Loss R. D., Lugmair G. W., Davis A. M. and MacPherson G. J. (1994) Isotopically distinct reservoirs in the solar nebula: isotope anomalies in Vigarano meteorite inclusions. *Astrophys. J.* **436**, L193–L196.

MacPherson G. J. and Davis A. M. (1994) Refractory inclusions in the prototypical CM chondrite, Mighei. *Geochim. Cosmochim. Acta* **58**, 5599–5625.

MacPherson G. J., Kita N. T., Ushikubo T., Bullock E. S. and Davis A. M. (2012) Well-resolved variations in the formation ages for Ca-Al-rich inclusions in the early Solar System. *Earth Planet. Sci. Lett.* **331-332**, 43–54.

MacPherson G. J. (2013) Calcium-Aluminum-Rich Inclusions in Chondritic Meteorites. In *Meteorites and Cosmochemical Processes*. Vol. 1 *Treatise on Geochemistry*, 2nd ed. (Exec. Eds. H. D. Holland and K. K. Turekian), Elsevier, Oxford, 139–179.

MacPherson G. J., Bullock E. S., Tenner T. J., Nakashima D., Kita N. T., Ivanova M. A., Krot A. N., Petaev M. I. and Jacobsen S. B. (2017) High precision Al–Mg systematics of forsterite-bearing Type B CAIs from CV3 chondrites. *Geochim. Cosmochim. Acta* **201**, 65–82.

Martin P. M. and Mason B. (1974) Major and trace elements in the Allende meteorite. *Nature* **249**, 333–334.

Martinez R. and Mason B. (1989) Description of sample MAC 88107. *Antarctic Meteorite Newsletter* **12**, 20.

Mason B. and Martin P. M. (1977) Geochemical differences among components of the Allende meteorite. *Smithson. Contrib. Earth Sci.* (**19**), 84–95.

Mason B. and Taylor S. R. (1982) Inclusions in the Allende Meteorite. *Smithsonian Contributions to the Earth Sciences*. 1–30.

Mason B. (1987) Thin section description of LEW 85332,4. *Antarctic Meteorite Newsletter* **10**, 15.

McKeegan K. D. (1998) Oxygen Isotopic Abundances in Calcium-Aluminum-Rich Inclusions from Ordinary Chondrites: Implications for Nebular Heterogeneity. *Science* **280**, 414–418.

McKeegan K. D., Kallio A. P. A., Heber V. S., Jarzebinski G., Mao P. H., Coath C. D., Kunihiro T., Wiens R. C., Nordholt J. E., Moses R. W., Reisenfeld D. B., Jurewicz A. J. G. and Burnett D. S. (2011) The oxygen isotopic composition of the Sun inferred from captured solar wind. *Science* **332**, 1528–1532.

Myojo K., Yokoyama T., Okabayashi S., Wakaki S., Sugiura N. and Iwamori H. (2018) The Origin and Evolution of Nucleosynthetic Sr Isotope Variability in Calcium and Aluminum-rich Refractory Inclusions. *Astrophys. J.* **853**, 48–56.

Nanne J. A. M., Nimmo F., Cuzzi J. N. and Kleine T. (2019) Origin of the non-carbonaceous – carbonaceous meteorite dichotomy. *Earth Planet. Sci. Lett.* **511**, 44–54.

Niederer F. R., Papanastassiou D. A. and Wasserburg G. J. (1980) Endemic isotopic anomalies in titanium. *Astrophys. J.* **240**, L73–L77.

Niederer F. R., Papanastassiou D. A. and Wasserburg G. J. (1981) The isotopic composition of titanium in the Allende and Leoville meteorites. *Geochim. Cosmochim. Acta* **45**, 1017–1031.

Niederer F. R., Papanastassiou D. A. and Wasserburg G. J. (1985) Absolute isotopic abundances of Ti in meteorites. *Geochim. Cosmochim. Acta* **49**, 835–851.

Niemeyer S. and Lugmair G. W. (1981) Ubiquitous isotopic anomalies in Ti from normal Allende inclusions. *Earth Planet. Sci. Lett.* **53**, 211–225.

Niemeyer S. and Lugmair G. W. (1984) Titanium isotopic anomalies in meteorites. *Geochim. Cosmochim. Acta* **48**, 1401–1416.

Olsen M. B., Wielandt D., Schiller M., Van Kooten E. M. M. E. and Bizzarro M. (2016) Magnesium and 54Cr isotope compositions of carbonaceous chondrite chondrules – Insights into early disk processes. *Geochim. Cosmochim. Acta* **191**, 118–138.

Palme H., Lodders K. and Jones A. (2014) Solar system abundances of the elements. In Planets, Asteroids, Comets and the Solar System. Vol. 2 Treatise on Geochemistry (ed. A. M. Davis), second ed. Elsevier, Oxford, pp. 15–36.

Papanastassiou D. A. (1986) Chromium Isotopic Anomalies in the Allende Meteorite. *Astrophys. J.* **308**, 27–30.

Papanastassiou D. A. and Brigham C. A., (1989) The identification of meteorite inclusions with isotope anomalies. *Astrophys. J. Lett.* **338**, L37–L40.

Peters S. T. M., Münker C., Pfeifer M., Elfers B. and Sprung P. (2017) Distribution of p-process ^{174}Hf in early solar system materials and the origin of nucleosynthetic Hf and W isotope anomalies in Ca-Al rich inclusions. *Earth Planet. Sci. Lett.* **459**, 70–79.

Prinz M., Weisberg M. K., Brearley A., Grady M. M., Pillinger C., Clayton R. N., Mayeda T. K. (1992) LEW85332: A C2 Chondrite in the CR Clan. *Meteoritics* **27**, 278.

Prinz M., Weisberg M. K., Clayton R. N., Mayeda T. K. (1993) Oxygen Isotopic Relationships Between the LEW85332 Carbonaceous Chondrites and CR Chondrites. *Lunar Planet. Sci. 24*, 1185.

Qin L., Alexander C. M. O. D., Carlson R. W., Horan M. F. and Yokoyama T. (2010) Contributors to chromium isotope variation of meteorites. *Geochim. Cosmochim. Acta* **74**, 1122–1145.

Qin L., Nittler L. R., Alexander C. M. O. D., Wang J., Stadermann F. J. and Carlson R. W. (2011) Extreme ^{54}Cr-rich nano-oxides in the CI chondrite Orgueil – Implication for a late supernova injection into the solar system. *Geochim. Cosmochim. Acta* **75**, 629–644.

Render J., Brennecka G. A., Wang S.-J., Wasylenki L. E. and Kleine T. (2018) A Distinct Nucleosynthetic Heritage for Early Solar System Solids Recorded by Ni Isotope Signatures. *Astrophys. J.* **862**, 26–43.

Render, J., Ebert, S., Burkhardt, C., Kleine, T., Brennecka, G. A. (2019) Titanium isotopic evidence for a shared genetic heritage of refractory inclusions from different carbonaceous chondrites. *Geochim. Cosmochim. Acta* **254**, 40-53.

Righter K. (2007) *Antarctic Meteorite Newsletter* **30**, 1.

Rubin A. E. and Wasson J. T. (1986) Chondrules in the Murray CM2 meteorite and compositional differences between CM–CO and ordinary chondrite chondrules. Geochim. Cosmochim. Acta 50, 307–315.

Rubin A. E. (1989) Size-frequency distributions of chondrules in CO3 chondrites. *Meteoritics* **24**, 179–189.

Rubin A. E., Kallemeyn G. W. (1990) Lewis Cliff 85332: A Unique Carbonaceous Chondrite. *Meteoritics* **25**, 215–225.

Rubin A. E. (2005) Relationships among intrinsic properties of ordinary chondrites: oxidation state, bulk chemistry, oxygen- isotopic composition, petrologic type, and chondrule size. *Geochim. Cosmochim. Acta* **69**, 4907–4918.

Russell S. S., Srinivasan G., Huss G. R., Wasserburg G. J. and MacPherson G. J. (1996) Evidence for Widespread 26Al in the Solar Nebula and Constraints for Nebula Time Scales. *Science* **273**, 757–762.

Russell S. S., McCoy T. J., Jarosewich E. and Ash R. D. (1998) The Burnwell, Kentucky, low-FeO chondrite fall: description, classification and origin. *Meteorit. Planet. Sci.* **33**, 853–856.

Russell S. S., Davis A. M., MacPherson G. J., Guan Y., Huss G.R. (2000) Refractory inclusions from the ungrouped carbonaceous chondrites MAC 87300 and MAC 88107. *Meteorit. Planet. Sci.* **35**, 1051–1066.

Ruzicka A., Floss C. and Hutson M. (2012) Amoeboid olivine aggregates (AOAs) in the Efremovka, Leoville and Vigarano (CV3) chondrites: A record of condensate evolution in the solar nebula. *Geochim. Cosmochim. Acta* **79**, 79–105.

Sanborn M. E., Yin Q.-Z., Schrader D. L. (2015) Aqueous alteration and its effect on ε^{54}Cr: An investigation of CR1 and CR2 chondrites. *78th Annual Meeting of the Meteoritical Society*, #5157.

Sanborn M. E., Wimpenny J., Williams C. D., Yamakawa A., Amelin Y., Irving A. J. and Yin Q. Z. (2019) Carbonaceous achondrites Northwest Africa 6704/6693: Milestones for early Solar System chronology and genealogy. *Geochim. Cosmochim. Acta* **245**, 577–596.

Sahijpal S., Goswami J. N. and Davis A. M. (2000) K, Mg, Ti and Ca isotopic compositions and refractory trace element abundances in hibonites from CM and CV meteorites: Implications for early solar system processes. *Geochim. Cosmochim. Acta* **64**, 1989–2005.

Satterwhite C. and Mason B. (1988) Description of MAC 87300. *Antarctic Meteorite Newsletter* **11**, 34.

Schrader D. L., Franchi I. A., Connolly, Jr., H. C., Greenwood R. C., Lauretta D. S. and Gibson J. M. (2011) The formation and alteration of the Renazzo-like carbonaceous chondrites I: Implications of bulk-oxygen isotopic composition. *Geochim. Cosmochim. Acta* **75**, 308–325.

Schrader D. L., Davidson J., Greenwood R. C., Franchi I. A. and Gibson J. M. (2014) A water-ice rich minor body from the early Solar System: The CR chondrite parent asteroid. *Earth Planet. Sci. Lett.* **407**, 48–60.

Schrader D. L. and Davidson J. (2017) CM and CO chondrites: A common parent body or asteroidal neighbors? Insights from chondrule silicates. *Geochim. Cosmochim. Acta* **214**, 157–171.

Schrader D. L., McCoy T. J., and Gardner-Vandy K. (2017) Relict chondrules in primitive achondrites: Remnants from their precursor parent bodies. *Geochim. Cosmochim. Acta* **205**, 295–312.

Scott E. R. D. and Krot A. N. (2014) Chondrites and their Components. Vol. 1 *Treatise on Geochemistry*, 2nd ed. (Exec. Eds. H. D. Holland and K. K. Turekian), Elsevier, Oxford, 65–137.

Sears D. W. G., Sears H., Myers B. M. (1990) The natural TL survey of the 1987/1988 Antarctic meteorite collections: An unusual carbonaceous chondrite group and the lunar meteorites. *Lunar Planet. Sci. 21*, 1121–1122.

Shields W. R., Murphy J. T., Cantazaro E. J. and Garner E. L. (1966) Absolute isotopic abundance ratios and the atomic weight of a reference sample of chromium. J. Res. Natl. Bur. Stand. 70A, 193–197.

Shollenberger Q. R., Borg L. E., Render J., Ebert S., Bischoff A., Russell S., Brennecka G.A. (2018a) Isotopic coherence of refractory inclusions from CV and CK meteorites: Evidence from multiple isotope systems. *Geochim. Cosmochim. Acta* **228**, 62–80.

Shollenberger Q.R., Render J., and Brennecka G.A. (2018b) Er, Yb, and Hf isotopic compositions of refractory inclusions: An integrated isotopic fingerprint of the Solar System's earliest reservoir. *Earth Planet. Sci. Lett*. **495**, 12–23.

Shukolyukov A., and Lugmair G. W. (2006) Manganese-chromium isotope systematics of carbonaceous chondrites. *Earth Planet. Sci. Lett.*, **250**, 200–213.

Simon J. I., Jordan M. K., Tappa M. J., Schauble E. A., Kohl I. E. and Young E. D. (2017) Calcium and titanium isotope fractionation in refractory inclusions: tracers of condensation and inheritance in the early solar protoplanetary disk. *Earth Planet. Sci. Lett*. **472**, 277–288.

Stephan T., Trappitsch R., Davis A. M., Pellin M. J., Rost D., Savina M. R., Yokochi R. and Liu N. (2016) CHILI – the Chicago Instrument for Laser Ionization – a new tool for isotope measurements in cosmochemistry. *Int. J. Mass Spectrom.* **407**, 1–15.

Sugiura N. and Fujiya W. (2014) Correlated accretion ages and ε^{54}Cr of meteorite parent bodies and the evolution of the solar nebula. *Meteorit. Planet. Sci.* **49**, 772–787.

Tachibana S., Abe M., Arakawa M., Fujimoto M., Iijima Y., Ishiguro M., Kitazato K., Kobayashi N., Namiki N., Okada T., Okazaki R., Sawada H., Sugita S., Takano Y., Tanaka S., Watanabe S., Yoshikawa M., Kuninaka H., and the Hayabusa2 Project Team. (2014) Hayabusa2: Scientific importance of samples returned from C-type near-Earth asteroid (162173) 1999 JU3. Geochem. J. 48, 571–587.

Takir D., Stockstill-Cahill K. R., Hibbitts C. A., Nakauchi Y. (2019) 3-µm Reflectance Spectroscopy of Carbonaceous Chondrites Under Asteroid-Like Conditions. *Lunar Planet. Sci. 50* (Abstract #2056).

Torrano Z. A., Brennecka G. A., Williams C. D., Romaniello S. J., Rai V. K., Hines R. R. and Wadhwa M. (2019) Titanium isotope signatures of calcium-aluminum-rich inclusions from CV and CK chondrites: Implications for early Solar System reservoirs and mixing. *Geochim. Cosmochim. Acta* **263**, 13–30.

Torrano Z. A., Davidson J., and Wadhwa M. (2020) The reclassification of Northwest Africa (NWA) 2900 from CV3 to CK3 chondrite. *LPSC 51* #1748.

Trinquier A., Birck J.-L. and Allègre C. J. (2007) Widespread ^{54}Cr Heterogeneity in the Inner Solar System. *Astrophys. J.* **655**, 1179–1185.

Trinquier A., Birck J. L., Allégre C. J., Göpel C. and Ulfbeck D. (2008) ^{53}Mn-^{53}Cr systematics of the early Solar System revisited. *Geochim. Cosmochim. Acta* **72**, 5146–5163.

Trinquier A., Elliott T., Ulfbeck D., Coath C., Krot A. N. and Bizzarro M. (2009) Origin of nucleosynthetic isotope heterogeneity in the solar protoplanetary disk. *Science* **324**, 374–376.

Troiano J., Rumble D. III, River M. L., and Friedrich J. M. (2011) Compositions of three low-FeO ordinary chondrites: Indications of a common origin with the H chondrites. *Geochim. Cosmochim. Acta* **75**, 6511–6519.

Wanajo S., Janka H. T. and Müller B. (2013) Electron-capture supernovae as origin of ^{48}Ca. *Astrophys. J. Lett.* **767**, L26, 6 pp.

Warren P. H. (2011) Stable-isotopic anomalies and the accretionary assemblage of the Earth and Mars: A subordinate role for carbonaceous chondrites. *Earth Planet. Sci. Lett.* **311**, 93–100.

Wasserburg G. J., Lee T. and Papanastassiou D. A. (1977) correlated O and Mg isotopic anomalies in Allende Inclusions: II. Magnesium. *Geophys. Res. Lett.* **4**, 299–302.

Wasson J. T., Rubin A. E. and Kallemeyn G. W. (1993) Reduction during metamorphism of four ordinary chondrites. *Geochim. Cosmochim. Acta* **57**, 1867–1878.

Weisberg M. K., McCoy T. J. and Krot A. N. (2006) Systematics and evaluation of meteorite classification. In *Meteorites and the Early Solar System II* (eds. D. S. Lauretta and H. Y. McSween). University of Arizona Press, Tucson, pp. 19–52.

Whitney B. A., Wood K., Bjorkman J. E., Wolff M. J. (2003) Two-dimensional radiative transfer in protostellar envelopes: I. Effects of geometry on class I sources. *Astrophys. J.* **591**, 1049–63.

Williams C. D., Janney P. E., Hines R. R. and Wadhwa M. (2016) Precise titanium isotope compositions of refractory inclusions in the Allende CV3 chondrite by LA-MC-ICPMS. *Chem. Geol.* **436**, 1–10.

Williams C. D., Ushikubo T., Bullock E. S., Janney P. E., Hines R. R., Kita N. T., Hervig R. L., Macpherson G. J., Mendybaev R. A., Richter F. M. and Wadhwa M. (2017) Thermal and chemical evolution in the early solar system as recorded by FUN CAIs: Part I – Petrology , mineral chemistry, and isotopic composition of Allende FUN CAI CMS-1. *Geochim. Cosmochim. Acta* **201**, 25–48.

Wood J. A. (2004) Formation of chondritic refractory inclusions: The astrophysical setting. *Geochim. Cosmochim. Acta* **68**, 4007–4021.

Yamaguchi A., Kimura M., Barrat J.-A., Greenwood R. (2019) Compositional diversity of ordinary chondrites inferred from petrology, bulk chemical, and oxygen isotopic compositions of the lowest FeO ordinary chondrite, Yamato 982717. *Meteorit. Planet. Sci.* **54**, 1919–1929.

Yamakawa A., Yamashita K., Makishima A. and Nakamura E. (2009) Chemical Separation and Mass Spectrometry of Cr, Fe, Ni, Zn, and Cu in Terrestrial and Extraterrestrial Materials Using Thermal Ionization Mass Spectrometry. *Anal. Chem* **81**, 9787–9794.

Yamakawa A., Yamashita K., Makishima A., and Nakamura E. (2010) Chromium isotope systematics of achondrites: Chronology and isotopic heterogeneity of the inner solar system bodies. *Astrophys. J.* **720**, 150–154.

Yamashita K., Maruyama S., Yamakawa A., Nakamura E. (2010) ^{53}Mn–^{53}Cr chronometry of CB chondrite: Evidence for uniform distribution of ^{53}Mn in the early Solar System. *Astrophys. J.* **723**, 20–24.

Yang L. and Ciesla F. J. (2012) The effects of disk building on the distributions of refractory materials in the solar nebula. *Meteorit. Planet. Sci.* **47**, 99–119.

Zhang J., Dauphas N., Davis A. M. and Pourmand A. (2011) A new method for MC-ICPMS measurement of titanium isotopic composition: Identification of correlated isotope anomalies in meteorites. *J. Anal. At. Spectrom.* **26**, 2197-2205.

Zhang J., Dauphas N., Davis A. M., Leya I. and Fedkin A. (2012) The proto-Earth as a significant source of lunar material. *Nature Geosci.* **5,** 251–255.

Zinner E. K., Fahey A. J., McKeegan K. D., Goswami J. N. and Ireland T. R. (1986) Large ^{48}Ca anomalies are associated with ^{50}Ti anomalies in Murchison and Murray hibonites. *Astrophys. J.* **311**, L103.

Zinner E., Amari S., Guinness R., Jennings C., Mertz A. F., Nguyen A. N., Gallino R., Hoppe P., Lugaro M., Nittler L. R. and Lewis R. S. (2007) NanoSIMS isotopic analysis of small presolar grains: search for Si3N4 grains from AGB stars, and Al and Ti isotopic compositions of rare presolar SiC grains. *Geochem. Cosmochim. Acta* **71**, 4786–4813.

Zolensky M., Barrett R., Browning L. (1993) Mineralogy and composition of matrix and chondrule rims in carbonaceous chondrites. *Geochim. Cosmochim. Acta* **57**, 3123–3148.

APPENDIX A

A RECLASSIFICATION OF NORTHWEST AFRICA 2900 FROM CV3 TO CK3.8 CHONDRITE

Abstract

Carbonaceous chondrites are classified into different groups based on their compositional and petrographic characteristics. Certain groups exhibit sufficient similarities that they are considered to be clans representing parent bodies which originated in close proximity to one another. In the case of CV and CK chondrites, these similarities are so substantial that some studies have argued for a common parent body origin. These similarities also mean that they are susceptible to misclassification as one another. It is therefore important to accurately classify CV and CK chondrites to properly compare the properties of the two groups and evaluate the single parent body hypothesis. In this study, we re-evaluate the current classification of Northwest Africa (NWA) 2900 as a CV3 chondrite. Based on chondrule abundance, chondrule size, iron content in chondrule and matrix olivine, magnetite abundance, elemental abundances in olivine and magnetite, and comparison with previously reported data for CV and CK chondrites, we propose that the classification of NWA 2900 be changed from CV3 chondrite to CK3.8 chondrite. We additionally refine the compositional criteria used to distinguish between CV and CK chondrites and demonstrate that bulk oxygen isotope compositions are not sufficient for reliably distinguishing between CV and CK chondrites.

A.1 Introduction

Northwest Africa (NWA) 2900 was found as a single 1375 g stone in the North African Sahara in 2004. Although this meteorite is currently classified as a Vigarano-like carbonaceous chondrite of petrologic type 3 (CV3) (Connolly et al., 2006), previous work has noted that it is largely equilibrated and possesses a recrystallized matrix similar to low-grade Karoonda-like chondrites of petrologic type 4 (CK4) (Chaumard et al., 2014). The criteria used for the classification of chondrites into different classes include their petrography and mineralogy (e.g., Weisberg et al., 2006), bulk element abundances (e.g., Kallemeyn et al., 1989), and oxygen isotope compositions (e.g., Clayton and Mayeda, 1999). The carbonaceous chondrite class is divided into distinct groups based on bulk composition and petrographic characteristics such as the relative sizes and modal abundances of chondritic components (e.g., chondrules). Certain groups, such as CV and CK chondrites, show such substantial similarities that they are considered to be clans that may represent distinct parent bodies that originated in close proximity to one another in the solar nebula (Weisberg et al., 2006).

All CV chondrites recognized to date are of petrologic type 3 (i.e., are unequilibrated) and are characterized by their high matrix abundances (~45 vol% on average), large chondrules (1 mm average diameter), and high abundances of relatively large (up to cm-sized) calcium-aluminum-rich inclusions (CAIs) and amoeboid olivine aggregates (AOAs) (~10–15 vol% on average) (Scott et al., 1996; Weisberg et al., 2006). The CV chondrites are subdivided into oxidized (CV_{ox}) and reduced (CV_{red}) subgroups based on modal metal/magnetite ratios and the Ni content of metal and sulfides (McSween, 1977). The oxidized subgroup is further subdivided into the Allende-like

(CV_{oxA}) and Bali-like (CV_{oxB}) subgroups based on the more restricted compositional range in matrix olivine compositions, lower matrix abundances, and higher metal/magnetite ratios observed in the CV_{oxA} subgroup relative to the CV_{oxB} subgroup (Weisberg et al., 1997). While phyllosilicates are not present in CV_{oxA} chondrites, their presence in the matrices of CV_{oxB} chondrites suggests that these samples experienced aqueous alteration (Krot et al., 1995, 1998, 2005). The CV_{oxA} chondrites contain an assemblage of secondary minerals such as andradite, grossular, hedenbergite, kirschsteinite, nepheline, sodalite, and wollastonite as a result of Fe–alkali–halogen metasomatism (Kimura and Ikeda, 1995; Krot et al., 1995, 1998, 2005). The CK chondrites are highly oxidized and are characterized by abundant magnetite (~1–8 vol%, averaging ~4 vol%), rounded magnetite-rich objects up to 1 mm in diameter, matrices containing plentiful equilibrated olivines, and the absence of Fe, Ni metal (e.g., Kallemeyn et al., 1991; Geiger and Bischoff, 1995). Whereas all CV chondrites are of unequilibrated petrologic type 3, CK chondrites span the entire petrologic range from type 3 to 6 (e.g., Kallemeyn et al., 1991; Greenwood et al., 2010; Chaumard et al., 2014, 2016; Dunn et al., 2016a), and those of petrologic type <4 show many petrographic and geochemical similarities to CV_{ox} chondrites (e.g., Kallemeyn et al., 1991; Greenwood et al., 2010).

A model for a common parent body for CV and CK chondrites was proposed by Greenwood et al. (2010) based on similarities between the two groups in chondrule size distribution, refractory-lithophile abundances, and whole-rock oxygen isotope compositions, along with the argument that observed differences in olivine compositions, oxidation, carbon content, presence of chondrule rims, and refractory inclusions could be

explained by different amounts of metamorphism experienced by a common body rather than being primary features of different bodies. In the model proposed by Greenwood et al. (2010) for a single heterogeneous CV–CK parent body, CV3 chondrites originate close to the asteroid surface while CK chondrites form deeper in the body, ranging from CK3 to CK6 petrologic types with increasing depth, i.e., the so-called onion-shell model (Wood, 2003; Trieloff et al., 2003). These authors additionally suggest that the lack of CK chondrite material within CV chondrites is because impact processes on the asteroid did not penetrate to sufficient depth to excavate these materials.

Some subsequent studies have supported the idea of a common CV–CK parent body, although alternatives to the onion-shell model include the formation of CK chondrites via metamorphism by radiative heating (Chaumard et al., 2012) and the burial and aqueous alteration of CK chondrites on a shocked CV-like parent body (Wasson et al., 2013). The support for the common CV–CK parent body model is based on similarities in CAI abundance and chondrule petrography (Wasson et al., 2013; Chaumard et al., 2014), a potential continuous CV–CK metamorphic series defined by chondrule abundance, size, type, and igneous rims (Chaumard and Devouard, 2016), and an apparent lack of pre-metamorphic petrographic differences between the two groups (Wasson et al., 2013). However, other studies have used differences in magnetite compositions and sizes and abundances of chondrules between CV and CK chondrites, which are inconsistent with a single metamorphic sequence (Dunn et al., 2016a), and distinct bulk Cr isotopic compositions (Yin et al., 2017) to argue against a common CV–CK parent body. Therefore, previous studies utilizing bulk analyses must be supplemented by studies of the compositions of individual minerals in large sample sets

of CV and CK chondrites to further evaluate the possibility of a common CV–CK parent body (Davidson et al., 2014a; Dunn et al., 2016a).

Due to their broad similarities, CV and CK chondrites are especially prone to misclassification as one another. It remains important to accurately classify CV and CK chondrites to properly compare the properties of the two groups and test the single parent body hypothesis. Based on a review of published data and new analyses, Dunn and Gross (2017) established additional criteria for distinguishing between CV and CK chondrites, including chondrule abundance, Fa content in chondrule and matrix olivine, and Cr_2O_3, TiO_2, NiO, and Al_2O_3 abundances in magnetite. In this study, we re-evaluate the classification of NWA 2900 as a CV3 chondrite and refine the criteria used to distinguish between CV and CK chondrites.

A.2 Analytical Methods

An epoxy-mounted 1-inch round thick section of NWA 2900 was initially characterized using an optical microscope. Backscattered electron (BSE) and X-ray element images (Al, Ca, Cr, Fe, Mg, Ni, S, Si) were obtained with the JXA-8520F electron probe microanalyzer (EPMA) in the Eyring Materials Center at Arizona State University (operating conditions: 20 kV, 30 nA). These images were used to identify phases for further study and to determine the modal abundances of the major chondritic components. High-resolution images were obtained for select, representative phases using the same instrument. Major and minor element abundances (Na, Mg, Al, Si, P, K, Ca, Ti, Cr, Mn, Fe, and Ni for silicates; Mg, Al, Si, Co, Ca, Ti, Cr, Fe, and Ni for magnetite) were determined quantitatively with the Cameca SX-100 EPMA at the

University of Arizona's Lunar and Planetary Laboratory (operating conditions: 15 kV, 20 nA). Silicate standards (with detection limits in wt% in parentheses) were Crete albite for Na (0.03), San Carlos olivine for Mg and Si (0.04 and 0.02, respectively), Hakone anorthite for Al and Ca (0.02 and 0.01, respectively), orthoclase for K (0.02), natural rutile for Ti (0.02), Smithsonian USNM 117075 for Cr (0.02), Rockport fayalite for Fe (0.07), rhodonite for Mn (0.05), synthetic apatite for P (0.02), natural barite for S (0.01), and nickel metal for Ni (0.07). Magnetite standards (with detection limit in parentheses in wt%) were Smithsonian USNM 117075 for Mg, Al, and Cr (0.04, 0.02, and 0.02, respectively), Hakone anorthite for Ca (0.01), natural rutile for Ti (0.01), natural hematite for Fe (0.07), San Carlos olivine for Si (0.02), nickel metal for Ni (0.07), cobalt metal for Co (0.01), and rhodonite for Mn (0.05). An overlap correction was applied to the magnetite analyses to account for the Cr Kβ peak overlap with the Mn Kα peak. Only magnetite and stoichiometric silicate analyses with totals between 98.0 and 101.0 wt% were considered of high quality and are presented here. Modal abundances and apparent chondrule diameters (both major and minor axes) were determined from full thick section BSE and X-ray element images using pixel counting in Adobe Photoshop®.

A.3 Results

A.3.1. Petrography

NWA 2900 exhibits low shock and moderate weathering (Connolly et al., 2006), and contains large chondrules (~13 vol%; average size = 1.11 mm, n = 25) and CAIs (~5 vol%; up to 2.5 mm diameter), magnetite (~4 vol%), and a coarse-grained interchondrule matrix (~78 vol%) (Fig. A1). No metal or sulfides were observed, although this could be

due to plucking and/or weathering. Some chondrules are Fe-rich (e.g., Fig. A2a, b, e) and those chondrules with Mg-rich cores have Fe-rich rims (Fig. A2c, d, f–h). As a result, some chondrules do not have distinct boundaries due to the Fe-rich, coarse-grained nature of the surrounding matrix (e.g., Fig. A2b, f). Chromium-bearing magnetite is abundant both in the matrix (Fig. A3) and associated with chondrules (Fig. A2), where it is observed both in rims and internally.

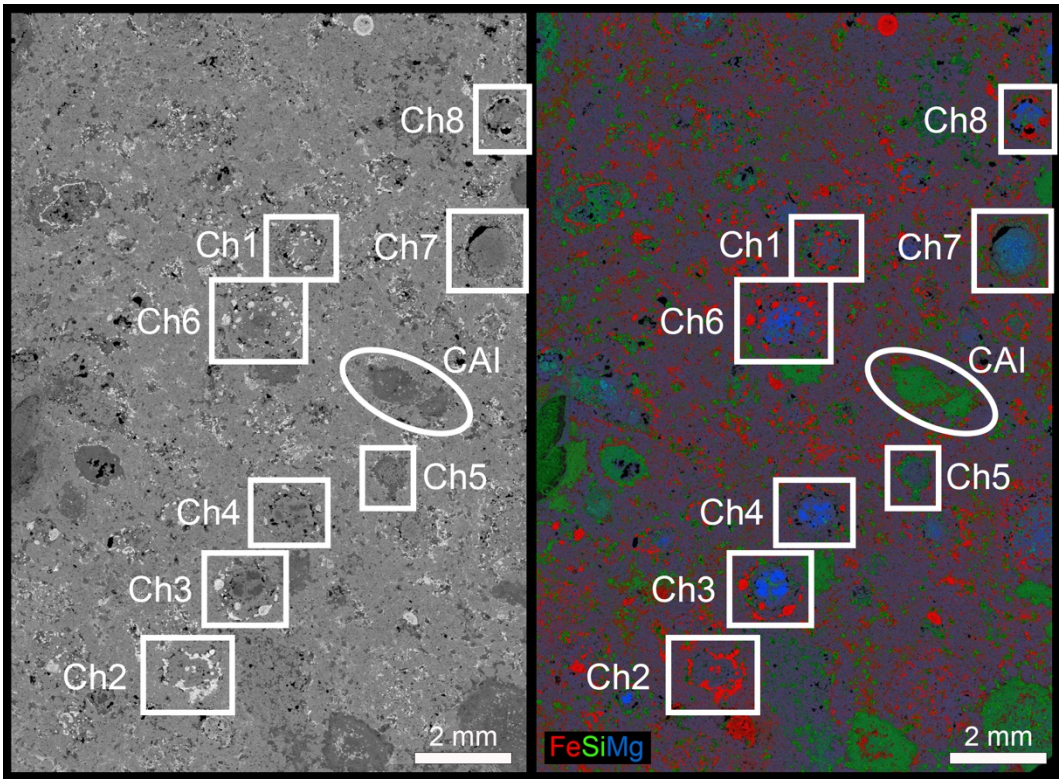

Fig. A1. (Left) BSE image of NWA 2900 and (Right) FeSiMg (RGB) elemental image of NWA 2900 (red = Fe, green = Si, blue = Mg). The white boxes indicate chondrules analyzed in this study (Ch1–Ch8; see Fig. A2 for BSE images and Tables A1 and A2 for magnetite and olivine compositions of these chondrules) and the white ellipse indicates a CAI. The brightest (i.e., white) regions in the BSE image are magnetite and correspond to the bright red regions in the RGB elemental image, such as the magnetite rims around some chondrules (e.g., Ch2, Ch3, Ch7, and Ch8). Mg-rich chondrule cores are blue in the right image (Ch3, Ch4, Ch6, Ch7, Ch8), and the interiors of other chondrules contain more Fe-rich silicates similar to the Fe-rich composition of the matrix (Ch1, Ch2, Ch5).

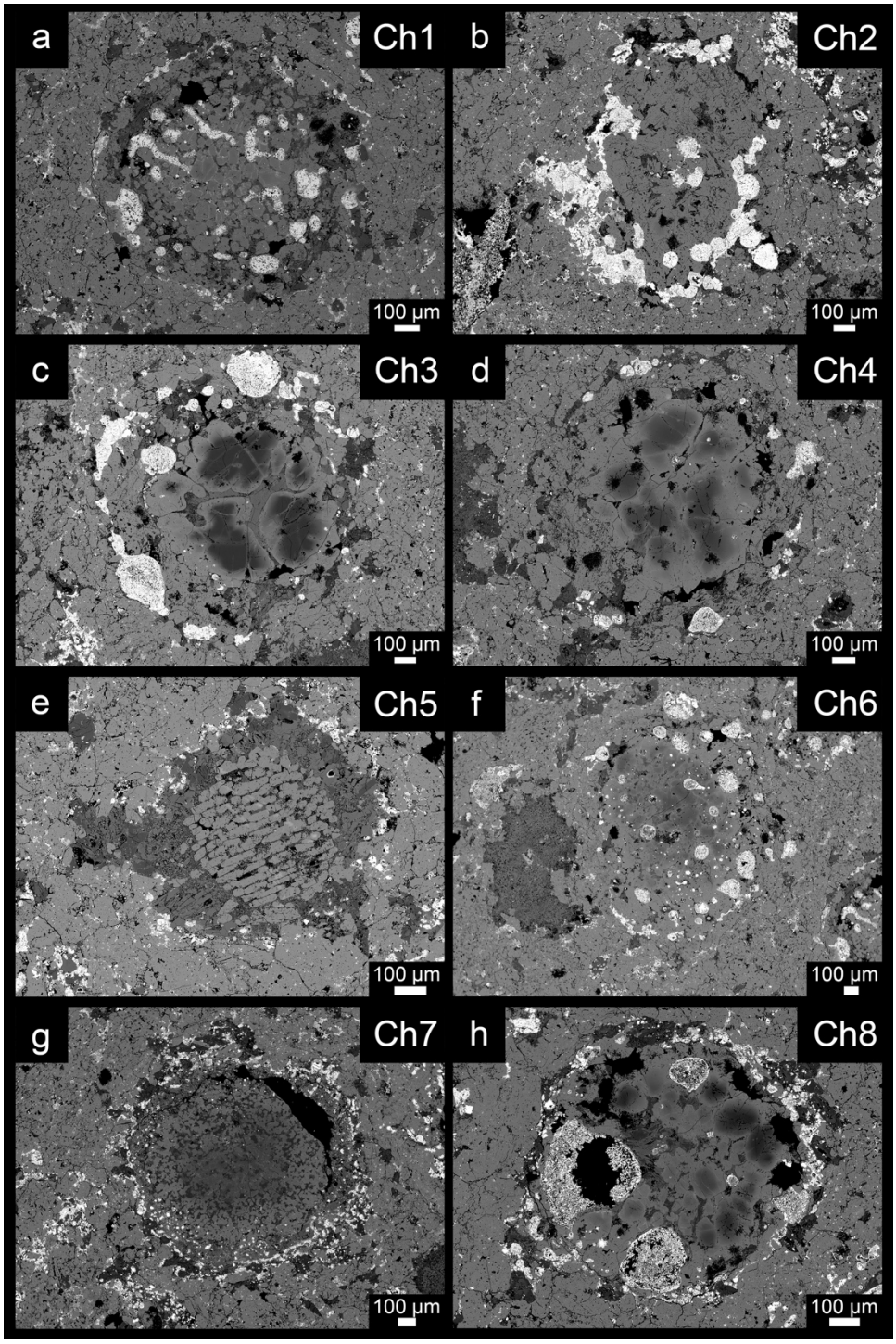

Fig. A2. BSE images of representative chondrules (Ch1–Ch8) from NWA 2900 analyzed in this study, including those with porphyritic (a–d, f–h) and barred olivine (e) textures.

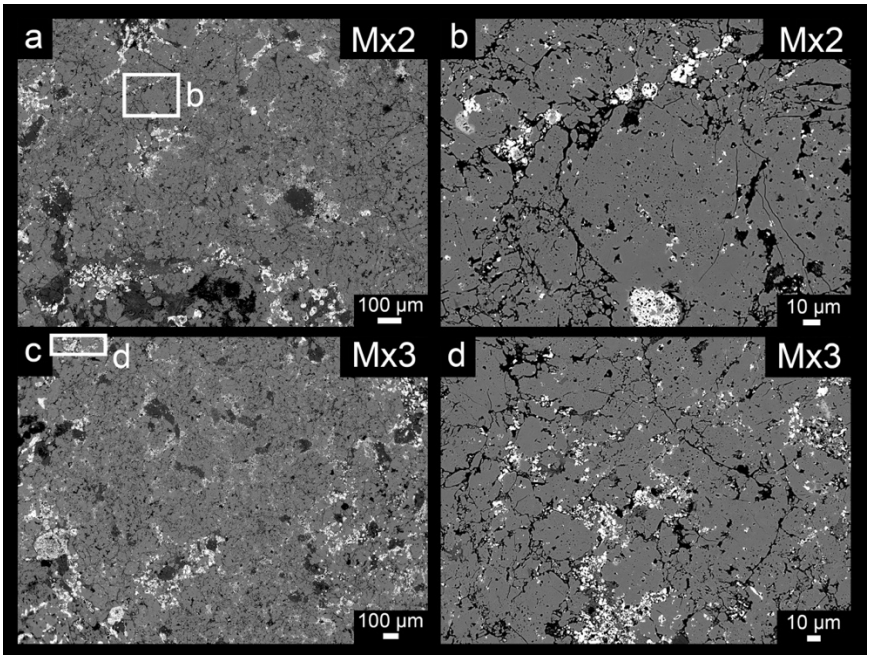

Fig. A3. BSE images of representative coarse-grained and uniformly Fe-rich matrix regions (Mx2 and Mx3) in NWA 2900, with white boxes in regions (a) and (c) indicating areas enlarged and shown in regions (b) and (d), respectively.

A.3.2 Magnetite Morphologies and Composition

Magnetite in NWA 2900 is present within the matrix (Fig. A3a–d), rimming chondrules (Fig. A2b, c, g, h), and within some chondrules (Fig. A2a, b, f, h). Magnetite grains occur primarily as rounded, inclusion-bearing porous grains although some inclusion-free subhedral grains are also observed (Fig. A3a–d; Fig. A4a–f). These morphologies are consistent with the magnetite observed in anomalous CK3 Watson-002 (Davidson et al., 2014a) and the CK3-like ungrouped C3 Ningqiang (Hsu et al., 2006). Major and minor element abundances in magnetite in NWA 2900 range from 1.23 to 4.00 wt% Cr_2O_3, 2.27 to 3.09 wt% Al_2O_3, 0.49 to 0.65 wt% TiO_2, and 0.22 to 0.38 wt% NiO. Compositions are compared with those of magnetite from previously measured CV chondrites (Haggerty and McMahon, 1979; Rubin, 1991; Murakami and Ikeda, 1994;

Choi et al., 1997; Greenwood et al., 2010; Davidson et al., 2014b; Dunn et al., 2016a; Dunn and Gross, 2017) and CK chondrites (Geiger and Bischoff, 1995; Righter and Neff, 2007; Greenwood et al., 2010; Davidson et al., 2014a; Dunn et al., 2016a) in Fig. A5. Representative chondrule magnetite compositions are given in Table A1 and examples of a subset of these are shown in Fig. A4a–f. Analysis spots shown in Fig. A4 demonstrate that care was taken to conduct spot analyses on pore- and inclusion-free areas to ensure good stoichiometric analyses.

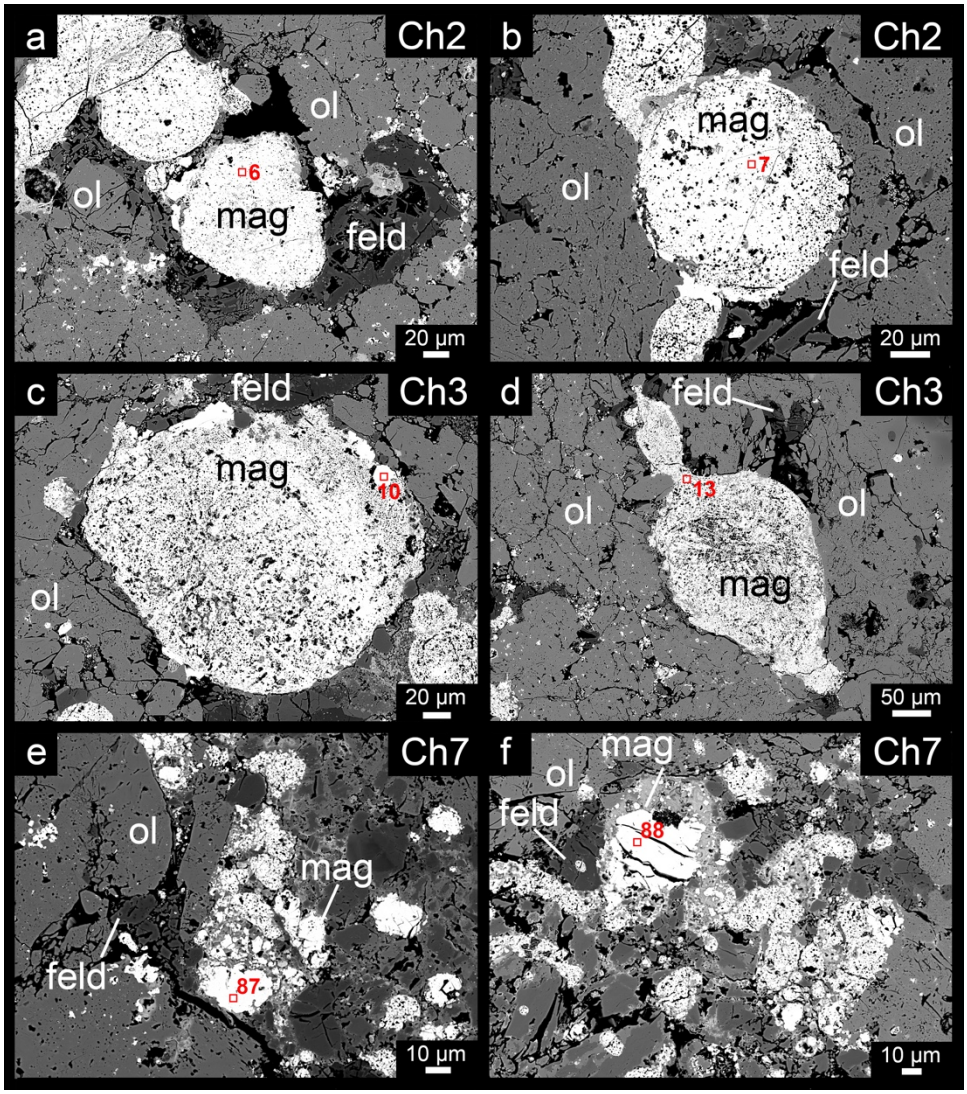

Fig. A4. BSE images of representative magnetites analyzed during this study from Chondrule 2 (a–b), Chondrule 3 (c–d) and Chondrule 7 (e–f). Examples of typical rounded, porous inclusion-bearing grains are shown in a–d, while examples of inclusion-free subhedral grains are shown in e–f. Numbered red squares correspond to magnetite analysis points (see Table A1); mag = magnetite, ol = olivine, and feld = feldspar.

Table A1. Representative microprobe analyses (wt%) of magnetite in chondrules from NWA 2900.

Region	Ch 1	Ch 2	Ch 2	Ch 3	Ch 3	Ch 6	Ch 6	Ch 7	Ch 7	Ch 8
Point	Mag 4	Mag 6	Mag 7	Mag 10	Mag 13	Mag 72	Mag 74	Mag 87	Mag 88	Mag 100
MgO	0.57	0.74	0.68	0.70	0.76	0.98	0.75	0.59	0.65	0.69
FeO	87.47	84.00	84.79	84.72	82.80	86.14	85.05	85.91	85.59	85.80
FeO*	30.55	29.27	29.43	30.20	27.62	28.95	30.44	30.55	30.35	30.45
Fe_2O_3*	63.26	60.83	61.51	60.59	61.32	63.56	60.69	61.52	61.39	61.51
CaO	0.04	0.84	0.79	0.06	0.89	0.72	bdl	0.08	0.06	0.04
CoO	0.02	0.02	bdl	bdl	0.03	bdl	0.03	bdl	0.03	bdl
MnO	bdl	bdl	bdl	bdl	bdl	bdl	bdl	bdl	bdl	bdl
NiO	0.23	0.33	0.33	0.28	2.11	0.29	0.27	0.25	0.35	0.22
Cr_2O_3	1.23	2.81	2.74	3.64	2.96	2.33	4.00	2.43	2.39	1.57
V_2O_3	bdl	bdl	bdl	bdl	bdl	bdl	bdl	bdl	bdl	bdl
TiO_2	0.49	0.61	0.60	0.52	0.60	0.08	0.54	0.60	0.62	0.59
Total	92.66	92.04	92.35	92.51	92.78	92.85	93.32	92.58	92.52	92.11
New Total*	98.99	98.13	98.51	98.63	98.92	99.21	99.40	98.74	98.67	98.27

*Data were initially processed with stoichiometric oxygen assigned to Fe as FeO (Fe^{2+}) resulting in the lower of the two reported totals ("Total"). The FeO and Fe_2O_3 contributions were calculated following the method of Droop (1987), and weight percent totals were recalculated ("New Total"). For calculation details, see Davidson et al. (2014a).
bdl = below detection limit.

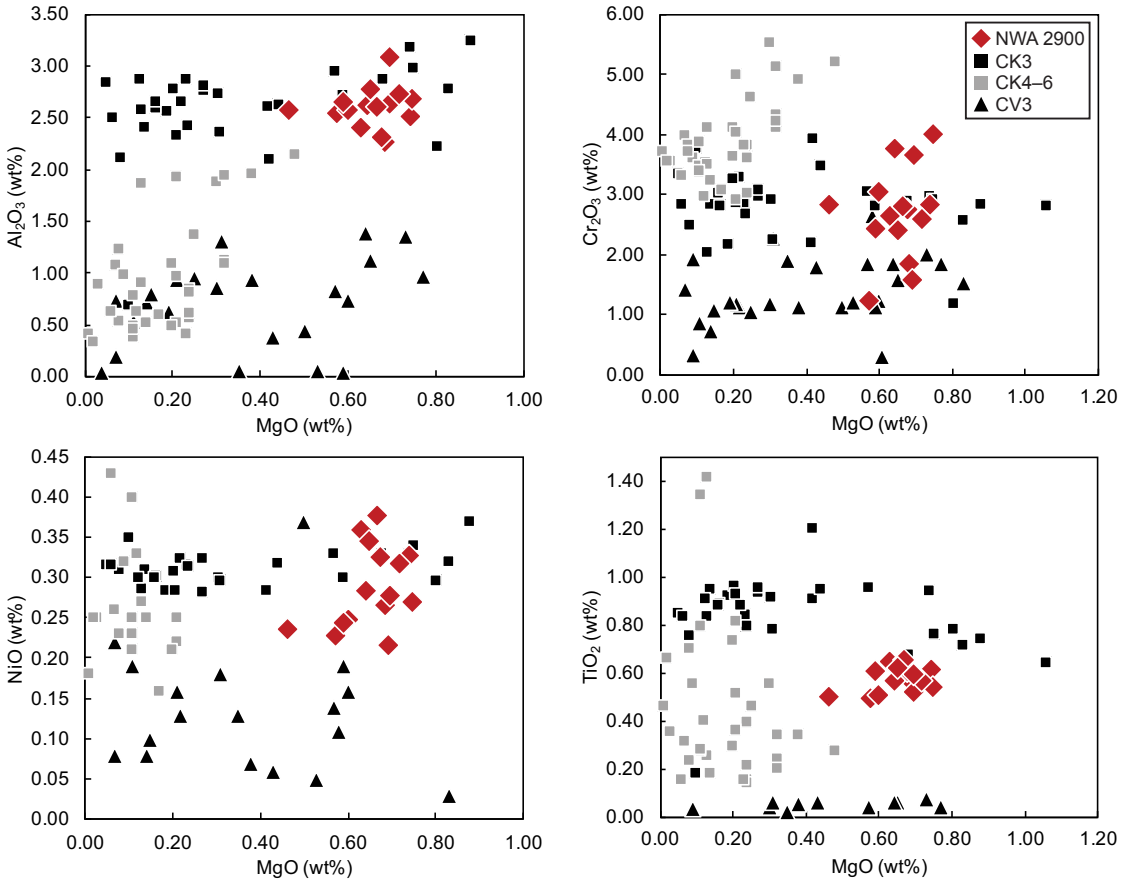

Fig. A5. Compositions of magnetite from NWA 2900 (red diamonds) plotted along with literature data for magnetites from CV3 (black triangles; Haggerty and McMahon, 1979; Rubin, 1991; Murakami and Ikeda, 1994; Choi et al., 1997; Greenwood et al., 2010; Dunn et al., 2016a; Dunn and Gross, 2017), CK3 (black squares; Davidson et al., 2014a; Dunn et al., 2016a; Geiger and Bischoff, 1995), and CK 4–6 (gray squares; Geiger and Bischoff, 1995; Righter and Neff, 2007; Greenwood et al., 2010; Dunn et al., 2016a) chondrites.

A.3.3 Olivine Compositions

Olivine grains were measured in eight chondrules (Ch1–Ch8) and three matrix (Mx1–Mx3) regions; representative major and minor element abundances are shown in Table A2. Fayalite compositions in chondrule olivine range from Fa_{1} to Fa_{35}, while matrix olivine is well equilibrated, with a range from Fa_{33} to Fa_{36} (Fig. A6). Chondrule

olivine contains 0.03 to 0.46 wt% Cr_2O_3, 0.04 to 0.91 wt% Al_2O_3, 0.03 to 0.20 wt% TiO_2, 0.07 to 0.24 wt% MnO, 0.09 to 0.50 wt% NiO, and 0.02 to 0.57 wt% CaO. All matrix olivine is characterized by >0.25 wt% NiO, with the majority >0.30 wt%. The compositions of olivine from eight chondrules in NWA 2900 are shown in Fig. A7, plotted along with chondrule olivine compositions from previously measured CV chondrites (Haggerty and McMahon, 1979; Rubin, 1991; Murakami and Ikeda, 1994; Choi et al., 1997; Greenwood et al., 2010; Davidson et al., 2014b; Dunn et al., 2016a; Dunn and Gross, 2017) and CK chondrites (Geiger and Bischoff, 1995; Righter and Neff, 2007; Greenwood et al., 2010; Davidson et al., 2014a; Chaumard and Devouard, 2016; Dunn et al., 2016a).

Table A2. Representative microprobe analyses (wt%) of olivine in chondrules and matrix from NWA 2900

Region	Ch 1	Ch 2	Ch 3	Ch 4	Ch 5	Ch 6	Ch 7	Ch 8	Mx 1	Mx 2	Mx 3
Point	Ol 104	Ol 29	Ol 16	Ol 35	Ol 45	Ol 65	Ol 85	Ol 92	Ol 56	Ol 111	Ol 119
MgO	34.31	31.41	43.20	41.48	34.26	34.40	34.28	50.66	32.57	31.69	31.20
FeO	27.50	30.52	16.43	18.09	27.74	27.15	26.84	7.36	30.04	30.18	31.41
CaO	0.09	0.26	0.48	0.20	0.10	0.27	0.10	0.28	0.06	0.27	0.27
MnO	0.20	0.22	0.11	0.13	0.15	0.19	0.18	bdl	0.24	0.23	0.22
NiO	0.39	0.33	0.11	0.10	0.32	0.31	0.31	bdl	0.33	0.32	0.31
Al_2O_3	0.07	0.51	0.19	0.31	0.11	0.08	0.07	0.15	0.32	0.10	0.10
Cr_2O_3	0.06	0.15	0.20	0.11	0.18	0.13	0.05	0.07	0.07	0.03	0.07
SiO_2	35.63	35.28	37.73	37.60	35.99	35.44	36.55	40.50	35.76	35.15	34.14
TiO_2	0.03	0.13	0.11	0.08	0.04	0.07	0.07	0.04	0.10	0.04	0.03
Total	98.28	99.04	98.56	98.28	98.97	98.02	98.50	99.06	99.59	98.12	98.25
Number of cations based on 4 oxygens for olivine:											
Mg	1.399	1.288	1.662	1.609	1.386	1.405	1.386	1.849	1.323	1.312	1.300
Fe	0.629	0.702	0.354	0.394	0.630	0.622	0.609	0.151	0.685	0.701	0.734
Ca	0.003	0.008	0.013	0.006	0.003	0.008	0.003	0.007	0.002	0.008	0.008
Mn	0.005	0.005	0.002	0.003	0.004	0.004	0.004	0.000	0.006	0.006	0.005
Ni	0.009	0.007	0.002	0.002	0.007	0.007	0.007	0.000	0.007	0.007	0.007
Al	0.002	0.017	0.006	0.010	0.004	0.003	0.002	0.004	0.010	0.003	0.003
Cr	0.001	0.003	0.004	0.002	0.004	0.003	0.001	0.001	0.002	0.001	0.002
Si	0.975	0.970	0.974	0.978	0.977	0.971	0.991	0.992	0.975	0.976	0.954
Ti	0.001	0.003	0.002	0.002	0.001	0.001	0.001	0.001	0.002	0.001	0.001
Total	3.023	3.008	3.019	3.008	3.016	3.025	3.004	3.005	3.013	3.017	3.025
Fa	31	35	18	20	31	31	31	8	34	35	36

bdl = below detection limit.

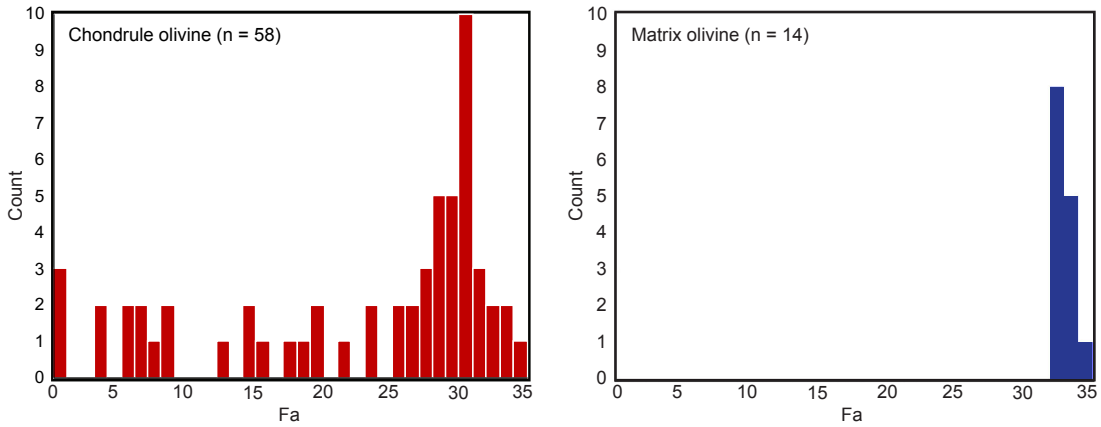

Fig. A6. Histograms of Fa content in chondrule olivine (left) and matrix olivine (right) in NWA 2900 showing that matrix olivine is equilibrated while chondrule olivine is not completely equilibrated.

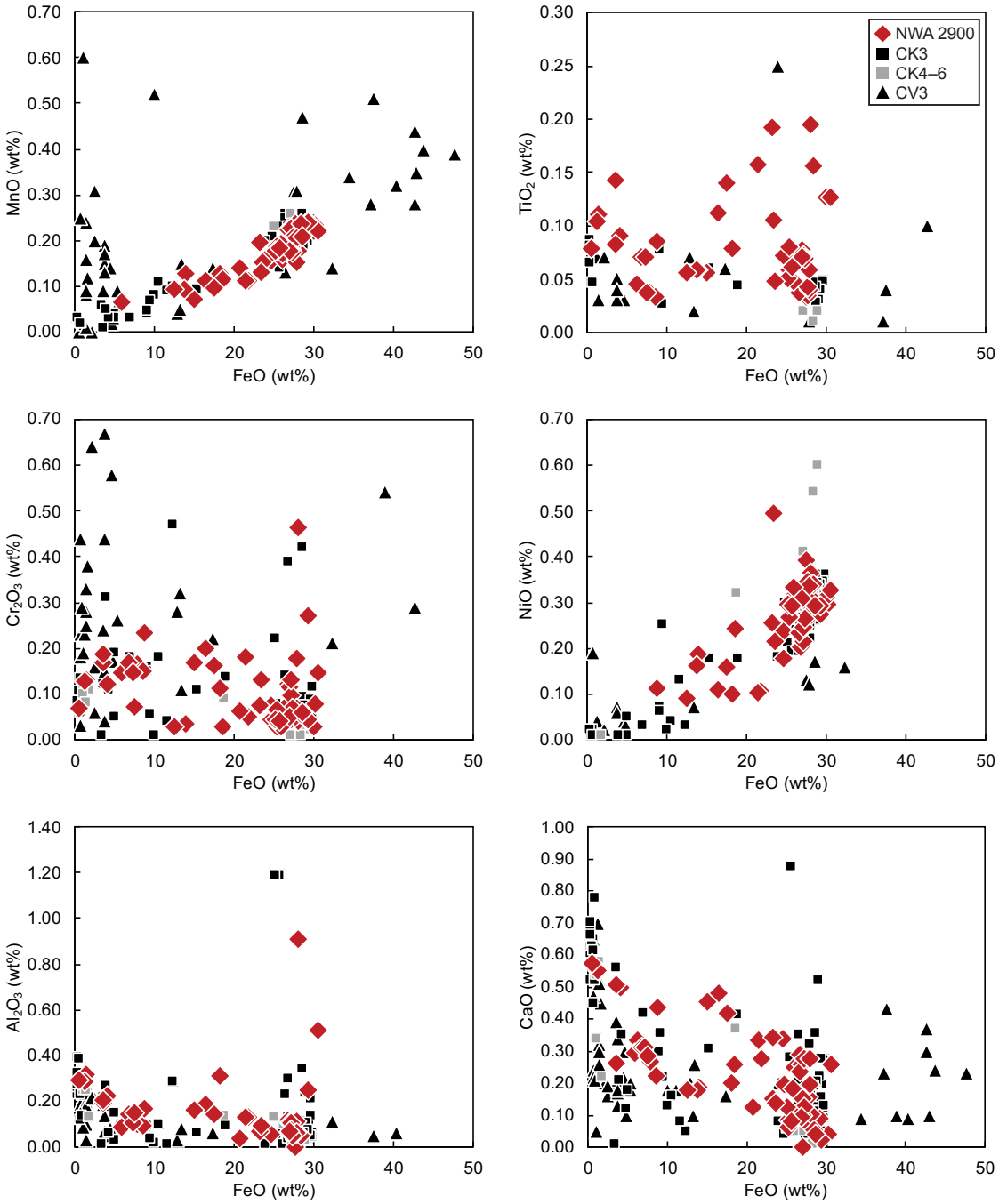

Fig. A7. Compositions of chondrule olivine from NWA 2900 (red diamonds) plotted along with literature data for chondrule olivines from CV3 (black triangles; Haggerty and McMahon, 1979; Rubin, 1991; Murakami and Ikeda, 1994; Choi et al., 1997; Greenwood et al., 2010; Davidson et al., 2014b; Dunn et al., 2016a; Dunn and Gross, 2017), CK3 (black squares; Davidson et al., 2014a; Chaumard and Devouard, 2016), and CK 4–6 (gray squares; Righter and Neff, 2007; Chaumard and Devouard, 2016) chondrites.

A.4 Discussion

A.4.1 The classification of Northwest Africa 2900

Although the CV and CK chondrite groups exhibit several similarities, including chondrule size distribution, refractory-lithophile abundances, and whole-rock oxygen isotope compositions, certain criteria can be used to reliably distinguish between them (as detailed by Dunn and Gross, 2017). Here, we re-evaluate the classification of NWA 2900 using these criteria and argue that the data convincingly demonstrate that NWA 2900 should be reclassified as a CK3.8 chondrite.

The chondrule abundance in NWA 2900 is ~13 vol%, which is similar to the previously reported chondrule abundances of ~15 vol% for CK4–6 chondrites (Kallemeyn et al., 1991; Scott et al., 1996) and ~25 vol% for CK3–4 chondrites (Chaumard and Devouard, 2016) and significantly lower than the ~45 vol% reported for CV chondrites (Scott et al., 1996; Weisberg et al., 2006). This chondrule abundance of ~13 vol%, combined with the average chondrule diameter of 1.11 mm is most consistent with the CK3.8 chondrites NWA 4724 and NWA 4425, which have chondrule abundances of 22.5 ± 6.0 vol% and 17.1 ± 2.7 vol% and average chondrule diameters of 0.81 ± 0.10 mm and 1.04 ± 0.06 mm, respectively (Chaumard and Devouard, 2016).

Chondrule olivine in NWA 2900 has a compositional range from Fa_{1} to Fa_{35} with a peak near ~Fa_{31} (Fig. A6). This is similar to the range of Fa_{1} to Fa_{34} reported for chondrule olivine in CK3 chondrites (Ivanova et al., 2000; Davidson et al., 2014a; Chaumard and Devouard, 2016) and the range of Fa_{1} to Fa_{33} reported for chondrule olivine in CK4 chondrites (Kallemeyn et al., 1991; Chaumard and Devouard, 2016). In

contrast, the Fa content of chondrule olivine in CV3 chondrites is typically <Fa_{15} (Dunn and Gross, 2017).

Matrix olivine in NWA 2900 has a compositional range of Fa_{33} to Fa_{36} (i.e., the matrix is mostly equilibrated), which is consistent with the compositional range of Fa_{32} to Fa_{37} previously reported for matrix olivine from CK3 chondrites (Dunn et al., 2016b). In equilibrated CK4–6 chondrites, matrix olivine is even more homogeneous, with a narrow range from Fa_{31} to Fa_{32} (Kallemeyn et al., 1991; Chaumard et al., 2009). The compositional range of matrix olivine in CV3 chondrites is highly variable from Fa_{0} to Fa_{99} (Peck, 1984; Scott et al. 1988; Krot et al. 1995; Choi et al., 1997; Kimura and Ikeda, 1998; Davidson et al., 2014b; Dunn and Gross, 2017). Matrix olivine in NWA 2900 is characterized by >0.25 wt% NiO, and the majority has >0.30 wt% NiO. This is generally consistent with the lower limit of NiO abundance for CK chondrites of 0.30 wt% established by Dunn and Gross (2017) and the range of 0.30 to 0.80 wt% for the NiO abundance previously reported for matrix olivine in CK3 chondrites (Dunn et al., 2016b) and is in contrast to the <0.30 wt% NiO previously reported for matrix olivine in CV3 chondrites (Peck 1984; Murakami and Ikeda 1994; Kimura and Ikeda 1998).

The abundance of magnetite in NWA 2900 is ~4 vol%, which is consistent with the average magnetite abundance in CK chondrites (Geiger and Bischoff, 1995). The minor element abundances in magnetite in NWA 2900 are also most consistent with those previously reported for magnetites in CK3 chondrites (Fig. A5). The lower limits of magnetite minor element abundances that must be met for classification as a CK chondrite according to the criteria of Dunn and Gross (2017) are 3.0 wt% Cr_2O_3, 0.1 wt%

TiO_2, 0.2 wt% NiO, and 2.0 wt% Al_2O_3. The magnetite in NWA 2900 exceeds each of these lower limits except for Cr_2O_3, and we propose that reducing this lower limit to 2.0 wt%—which is exceeded by the majority of the magnetite in NWA 2900—is required by the CV and CK magnetite data in the literature (see following section).

A.4.2 New criteria for distinguishing between CV and CK chondrites

In addition to using the criteria from Dunn and Gross (2017) to classify NWA 2900 as a CK chondrite, we also seek to refine the criteria for distinguishing between CV and CK chondrites. Magnetite in NWA 2900 exceeds each of the elemental abundance lower limits established by Dunn and Gross (2017) except for Cr_2O_3. However, based on our literature data compilation (Fig. A5) we propose reducing the lower limit of Cr_2O_3 abundance for classification as a CK3 chondrite from the 3.0 wt% proposed by Dunn and Gross (2017) to 2.0 wt% because most CK3 chondrite magnetite has a Cr_2O_3 abundance above 2.0 wt% and below 3.0 wt% Cr_2O_3, and most CV3 chondrite magnetite has a Cr_2O_3 abundance below 2.0 wt% (Fig. A5). Additionally, most CK4–6 chondrite magnetite has a Cr_2O_3 abundance above 3.0 wt%, so this threshold can instead be used to distinguish between CK3 and CK4–6 chondrites.

The bulk oxygen isotope composition of NWA 2900 ($\delta^{17}O$ = –1.361‰, $\delta^{18}O$ = +3.027‰, $\Delta^{17}O$ = −2.935‰) was one of the criteria used to classify it as a CV3 chondrite (Connolly et al., 2006). In three-oxygen isotope space, $CV3_{oxA}$ chondrites define a large field along the carbonaceous chondrite anhydrous mineral (CCAM) line and $CV3_{red}$ and $CV3_{oxB}$ chondrites define smaller fields that significantly overlap the $CV3_{oxA}$ field but are

distinct from each other (Fig. A8). Previously measured CK chondrites define a field similar to that of the $CV3_{oxA}$ chondrites, which encompasses the $CV3_{red}$ field and overlaps slightly with the $CV3_{oxB}$ field (Fig. A8). NWA 2900 plots near the edge of the CV_{oxA} and CV_{oxB} chondrite fields (Fig. A8) but is more enriched in both $\delta^{17}O$ and $\delta^{18}O$ than all previously measured CV and CK chondrites. Due to the evidence for classifying NWA 2900 as a CK chondrite presented in this study, we conclude that NWA 2900 expands the known range of oxygen isotope compositions for CK chondrites (gray dotted oval) and further demonstrates that bulk oxygen isotope compositions may be unable to reliably distinguish between CV3 and CK chondrites. Although it is tempting to cite the overlapping oxygen isotope compositions of CV3 and CK chondrites as evidence for a single parent body origin (e.g., Greenwood et al., 2010), other compositional and isotopic evidence points to distinct parent body origins of these two chondrite groups and the similarities in oxygen isotope compositions may instead reflect similar spatial origin of these parent bodies in the Solar System and/or parent body processes.

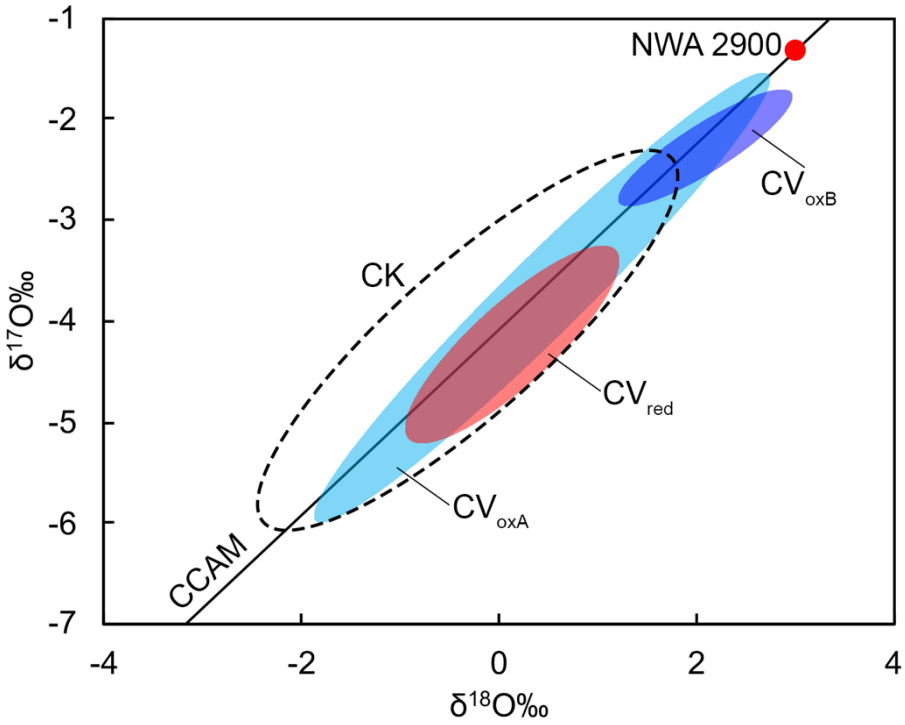

Fig. A8. Bulk oxygen isotope compositions of CV and CK chondrites redrawn from Greenwood et al. (2010). Compositional ranges for previously analyzed $CV3_{red}$ (red), $CV3_{oxA}$ (gray), $CV3_{oxB}$ (blue), and CK3–6 (dashed black) chondrites are indicated by the oval fields (Clayton et al., 1977; Clayton and Mayeda, 1999; Greenwood et al., 2010). The oxygen isotope composition of NWA 2900 is plotted as a red circle (Connolly et al., 2006). The dotted gray oval shows an extended CK chondrite field when NWA 2900 is included.

A.5 Summary

Based on petrographic observations, modal abundances of chondrules and magnetite, major and minor element compositions of magnetite and olivine, and Fa contents of chondrule and matrix olivine, we demonstrate that NWA 2900 should be reclassified as a CK3.8 chondrite. We also propose a modification of the criteria of Dunn and Gross (2017) to reduce the lower limit of Cr_2O_3 abundance for classification as a CK3 chondrite from 3.0 wt% to 2.0 wt% and further demonstrate that the 3.0 wt% threshold can be used to distinguish between CK3 and CK4–6 chondrites. Finally, NWA

2900 expands the known range of oxygen isotope compositions of CK chondrites and demonstrates that bulk oxygen isotope compositions cannot be used to reliably distinguish between CV and CK chondrites.

Acknowledgments: We thank Axel Wittmann and Ken Domanik for their assistance with the electron microprobes at Arizona State University and University of Arizona, respectively. We acknowledge the use of facilities within the Eyring Materials Center at Arizona State University supported in part by NNCI-ECCS-1542160. This work was supported by NASA grants NNX15AH41G to M. W. and NNH19ZDA005K to Z. T. and M. W.

REFERENCES FOR APPENDIX A

Chaumard N., Devouard B., Zanda B., and Ferrière L. 2009. The link between CV and CK carbonaceous chondrites based on parent body processes (abstract #5206). *Meteoritics & Planetary Science* 55 (Suppl.).

Chaumard N., Devouard B., Delbo M., Provost A., and Zanda B. 2012. Radiative heating of carbonaceous near-Earth objects as a cause of thermal metamorphism for CK chondrites. *Icarus* 220:65–73.

Chaumard N., Devouard B., Bouvier A., and Wadhwa M. 2014. Metamorphosed calcium-aluminum inclusions in CK carbonaceous chondrites. *Meteoritics & Planetary Science* 49:419–452.

Chaumard N. and Devouard B. 2016. Chondrules in CK carbonaceous chondrites and thermal history of the CV-CK parent body. *Meteoritics & Planetary Science* 51:547–573.

Choi B. -G., McKeegan K. D., Leshin L. A., and Wasson J. T. 1997. Origin of the magnetite in oxidized CV chondrites: In situ measurement of oxygen isotopic compositions of Allende magnetite and olivine. *Earth and Planetary Science Letters* 146:337–349.

Clayton R. N., Onuma N., Grossman L., and Mayeda T. K. 1977. Distribution of the presolar component in Allende and other carbonaceous chondrites. *Earth and Planetary Science Letters* 34:209–224.

Clayton R. N. and Mayeda T. K. 1999. Oxygen isotope studies of carbonaceous chondrites. *Geochimica et Cosmochimica Acta* 63:2089–2104.

Connolly H. C. Jr., Zipfel J., Grossman J. N., Folco L., Smith C., Jones R. H., Righter K., Zolensky M., Russell S. S., Benedix G. K., Yamaguchi A., and Cohen B. A. 2006. The Meteoritical Bulletin, No. 90, 2006 September. *Meteoritics & Planetary Science* 41:1383–1418.

Davidson J., Krot A. N., Nagashima K., Hellebrand E., and Lauretta D. S. 2014a. Oxygen isotope and chemical compositions of magnetite and olivine in the anomalous CK3 Watson 002 and ungrouped Asuka-881595 carbonaceous chondrites: Effects of parent body metamorphism. *Meteoritics & Planetary Science* 49:1456–1474.

Davidson J., Schrader D. L., Alexander C. M. O. D., Lauretta D. S., Busemann H., Franchi I. A., Greenwood R. C., R H. C. C. J., Domanik K. J., and Verchovsky A. 2014b. Petrography, stable isotope compositions, microRaman spectroscopy, and presolar components of Roberts Massif 04133: A reduced CV3 carbonaceous chondrite. *Meteoritics & Planetary Science* 49:2133–2151.

Droop G. T. R. 1987. A general equation for estimating Fe3+ concentrations in ferromagnesian silicates and oxides from microprobe analyses, using stoichiometric criteria. *Mineralogical Magazine* 51:431–435.

Dunn T. L., Gross J., Ivanova M. A., Runyon S. E., and Bruck A. M. 2016a. Magnetite in the unequilibrated CK chondrites: Implications for metamorphism and new insights into the relationship between the CV and CK chondrites. *Meteoritics & Planetary Science* 51:1701– 1720.

Dunn T. L., Gross J., and Ivanova M. 2016b. Homogeneity of matrix and chondrule olivine in the unequilibrated CK chondrites (abstract #1921). *Meteoritics & Planetary Science* 51 (Suppl.).

Dunn T. L. and Gross J. 2017. Reclassification of Hart and Northwest Africa 6047: Criteria for distinguishing between CV and CK3 chondrites. *Meteoritics & Planetary Science* 52:2412–2423.

Geiger T. and Bischoff A. 1995. Formation of opaque minerals in CK chondrites. *Planetary and Space Sciences* 43:485–498.

Greenwood R. C., Franchi I. A., Kearsley A. T., and Alard O. 2010. The relationship between CK and CV chondrites. *Geochimica et Cosmochimica Acta* 74:1684–1705.

Haggerty S. E. and McMahon B. M. 1979. Magnetite-sulfide-metal complexes in the Allende meteorite. Proceedings, 10th Lunar and Planetary Science Conference. pp. 851– 870.

Hsu W., Guan Y., Hua X., Wang Y., Leshin L. A., and Sharp T. G. 2006. Aqueous alteration of opaque assemblages in the Ningqiang carbonaceous chondrite: Evidence from opaque assemblages in oxygen isotopes. *Earth and Planetary Science Letters* 243:107–114.

Ivanova M. A., Nazarov A., Kononkova N. N., Taylor L. A., Patchen A., Clayton R. N., and Mayeda T. K. (2000) Dhofar 015, a new CK3 chondrite: a record of nebular processes. *Meteoritics & Planetary Science* 35:A83.

Kallemeyn G. W., Rubin A. E., Wang D., and Wasson J. T. 1989. Ordinary chondrites–bulk compositions, classification, lithophile-element fractionations, and composition-petrographic type relationships. *Geochimica et Cosmochimica Acta* 53:2747–2767.

Kallemeyn G. W., Rubin A. E., and Wasson J. T. 1991. The compositional classification of chondrites: V. The Karoonda (CK) group of carbonaceous chondrites. *Geochimica et Cosmochimica Acta* 55:881–892.

Kimura M. and Ikeda Y. 1998. Hydrous and anhydrous alterations of chondrules in Kaba and Mokoia CV chondrites. *Meteoritics & Planetary Science* 33:1139–1146.

Krot A. N., Scott E. R. D., and Zolensky M. E. 1995. Mineralogical and chemical modification of components in CV chondrites: nebular or asteroidal processing? *Meteoritics* 30:748–775.

Krot A. N., Petaev M. I., Scott E. R. D., Choi B. -G., Zolensky M. E., and Keil K. 1998. Progressive alteration in CV chondrites: more evidence for asteroidal alteration. *Meteoritics & Planetary Science* 33:1065–1085.

Krot A. N., Keil K., Goodrich C. A., Scott E. R. D., and Weisberg M. K. 2005. Classification of meteorites. In *Meteorites, Comets and Planets*. Treatise on Geochemistry, vol. 1 (ed. A. Davies). Elsevier B.V., 83–127.

McSween H. Y. Jr. 1977. Petrographic variations among carbonaceous chondrites of the Vigarano type. *Geochimica et Cosmochimica Acta* 41:1777–1790.

Murakami T. and Ikeda Y. 1994. Petrology and mineralogy of the Yamato-86751 CV3 chondrite. *Meteoritics* 29:397–409.

Peck J. A. 1984. Origin and variation in properties of CV3 chondrite matrix and matrix clasts. Proceedings, 16th Lunar and Planetary Science Conference. pp. 635–636.

Righter K. and Neff K. E. 2007. Temperature and oxygen fugacity constraints on CK and R chondrite, and implications for water and oxidation in the early solar system. *Polar Science* 1:25–44.

Rubin A. E. 1991. Euhedral awaruite in the Allende meteorite: Implications for the origin of awaruite- and magnetite-bearing nodules in CV3 chondrites. *American Mineralogist* 76:1356–1362.

Scott E. R. D., Barber D. J., Alexander C. M. O'D., Hutchinson R., and Peck J. A. 1988. Primitive material surviving in chondrites: Matrix. *Meteorites and the early solar system*, edited by Kerridge J. F and Mathews M. S. Tucson, Arizona: The University of Arizona Press. pp. 718–745.

Scott E. R. D., Love S. G., and Krot A. N. 1996. Formation of chondrules and chondrites in the protoplanetary nebula. In *Chondrules and the protoplanetary disk*, eds. Hewins R. H., Jones R. H., and Scott E. R. D. Cambridge, UK: Cambridge University Press. 87–96.

Trieloff M., Jessberger E. K., Herrwerth I., Hopp J., Fiéni C., Ghélis M., Bourot-Denise M. and Pellas P. (2003) Structure and thermal history of the H-chondrite parent asteroid revealed by thermochronometry. *Nature* 422:502–506.

Wasson J. T., Isa J., and Rubin A. E. 2013. Compositional and petrographic similarities of CV and CK chondrites: A single group with variations in textures and volatile concentrations attributable to impact heating, crushing and oxidation. *Geochimica et Cosmochimica Acta* 108:45–62.

Weisberg M. K., Prinz M., Clayton R. N., and Mayeda T. K. 1997. CV3 chondrites: Three subgroups, not two. *Meteoritics & Planetary Science* 32:A138–A139.

Weisberg M. K., McCoy T. J., and Krot A. N. 2006. Systematics and evaluation of meteorite classification. *Meteorites and the early solar system*, 2nd ed. Tucson, Arizona: The University of Arizona Press. pp. 19–52.

Wood J. A. (2003) Of asteroids and onions. *Nature* 422:479–481.

Yin Q.-Z., Sanborn M. E., and Zeigler K. 2017. Testing the common source hypothesis for CV and CK chondrites parent body using $\Delta^{17}O$–$\varepsilon^{54}Cr$ isotope systematics (abstract #1771). 48th Lunar and Planetary Science Conference.

APPENDIX B

PREVIOUS PUBLICATION/STATEMENT OF CO-AUTHORS

Chapter 2, Chapter 3, Chapter 4, and Appendix A of this dissertation are all co-authored manuscripts in various stages of publication and preparation for publication. Chapter 2 was published in Geochimica et Cosmochimica Acta in 2019 and Appendix A has been submitted for publication in Meteoritics and Planetary Science in 2020. Chapters 3 and 4 are in preparation for submission. I am the first author of each of these co-authored manuscripts, and all co-authors (listed below) have given their permission for the use of these documents in this dissertation.

Chapter 2 co-authors: Gregory A. Brennecka, Curtis D. Williams, Stephen J. Romaniello, Vinai K. Rai, Rebekah R. Hines, and Meenakshi Wadhwa.

Chapter 3 co-authors: Gregory A. Brennecka, Cameron M. Mercer, Stephen J. Romaniello, Vinai K. Rai, Rebekah R. Hines, and Meenakshi Wadhwa.

Chapter 4 co-authors: Devin L. Schrader, Jemma Davidson, Richard C. Greenwood, Vinai K. Rai, Rebekah R. Hines, and Meenakshi Wadhwa.

Appendix A co-authors: Jemma Davidson and Meenakshi Wadhwa.